

2010

Focussed electric field induced ion transport: A novel nano-patterning process

Dibyadeep Paul
Iowa State University

Follow this and additional works at: <https://lib.dr.iastate.edu/etd>

 Part of the [Mechanical Engineering Commons](#)

Recommended Citation

Paul, Dibyadeep, "Focussed electric field induced ion transport: A novel nano-patterning process" (2010). *Graduate Theses and Dissertations*. 11467.
<https://lib.dr.iastate.edu/etd/11467>

This Thesis is brought to you for free and open access by the Iowa State University Capstones, Theses and Dissertations at Iowa State University Digital Repository. It has been accepted for inclusion in Graduate Theses and Dissertations by an authorized administrator of Iowa State University Digital Repository. For more information, please contact digirep@iastate.edu.

Focused Electric Field Induced Ion Transport: A novel nano-imprinting
approach

by

Dibyadeep Paul

A thesis submitted to the graduate faculty
in partial fulfillment of the requirements for the degree of
MASTER OF SCIENCE

Co-Major: Mechanical Engineering, Electrical Engineering

Program of Study Committee:

Abhijit Chandra, Co-Major Professor

Ashraf Bastawrsos, Co-Major Professor

Liang Dong, Co-Major Professor

Iowa State University

Ames, Iowa

2010

Copyright © Dibyadeep Paul, 2010. All rights reserved

TABLE OF CONTENTS

LIST OF FIGURES	iv
LIST OF TABLES	vii
ABSTRACT	viii
CHAPTER 1 INTRODUCTION: LITERATURE REVIEW	1
1.1. Various Similar Processes Studied Earlier	2
1.2. Electrode Processes and Formation of Anodic Films	3
1.3. Ion and water transport through Nafion	4
1.3.1 Simple models	4
1.3.2 Diffusive models	5
1.3.2.1 Dilute solution theory	5
1.3.2.2 Concentrated solution theory	6
1.3.3 Hydraulic models	10
1.3.4 Combination models	11
1.4. Electrolyte transport/Modeling of Nafion membrane	12
1.5. Transport properties of Nafion	14
CHAPTER 2 THEORY	16
2.1. Background	16
2.1.1 Dilute Solution Theory	16
2.1.1.1 Migration flux	17
2.1.1.2 Diffusive flux	17
2.1.1.3 Convective flux	18
2.1.2 Electroneutrality condition	21
2.1.3 Electrode Kinetics	21
2.1.3.1 Theoretical Derivation of Butler-Volmer equation	23
2.1.4 Modeling of Interfaces	27
2.2. Calculation of dielectric constant of membrane	28
2.3. Calculation of deformation of membrane	29
2.4. Model equations	30
2.4.1 Domain Equations	33
2.4.2 Boundary Conditions	34
2.5. Numerical simulation procedure	34
2.5.1 Mesh Generation:	34
2.5.2 Mesh Size:	35
2.6. Numerical Method:	36
2.6.1 Solution for the concentration and potential fields	36
2.6.2 Solution of the shape of the copper anode	39
2.6.3 Mesh Update and Smoothing	41
CHAPTER 3 SIMULATION AND RESULTS	43
3.1. Experimental results	43
3.1.1 Method 1: Direct Contact Mask-Modulated Electric Field Printing	43
3.1.2 Method 2: Non-contact Mask-Modulated Electric Field Printing	45
3.1.3 Method 3: Non-contact Uniform Electric Field Mask Printing	47

3.2. Simulation details	49
3.3. Variation with height from electrode surface	50
3.4. Variation with chamber width/periodicity of mask opening	56
3.5. Variation with opening radius	60
3.6. Variation with standoff distance between mask and anode surface	71
3.7. Variation with membrane and mask thickness	72
3.8. Variation with curvature of membrane	76
3.9. Variation of surface profile with time	78
3.10. Variation with Electrode potential	90
3.11. Variation with H ₂ SO ₄ concentration	96
3.12. Variation with mask and membrane dielectric constant	103
CHAPTER 4 CONCLUSION	108
ACKNOWLEDGEMENTS	110
BIBLIOGRAPHY	111

LIST OF FIGURES

Figure 1.1 Membrane structure and interactions as a function of water content λ (moles of water per mole of sulphonic acid sites). The black regions are the fluorocarbon backbones, the grayish-white regions inside the black regions are the water molecules, the dotted black regions correspond to the collapsed membrane configuration	8
Figure 1.2 Schematic depicting a microscale model with sulphonic ions, water molecules and hydrogen ions	9
Figure 2.1 Energy diagram of an electron-ion system	24
Figure 2.2: Potential Energy diagram for an elementary charge transfer step	25
Figure 2.3 Boundary between two different media	27
Figure 2.4 Schematic of model domain	32
Figure 3.1: Experimental Configuration for direct contact printing method	43
Figure 3.2 Direct contact printing under CDC voltage (5V, pulse duration = 0.02/200 μ sec., exposure = 10sec.)	44
Figure 3.3: Schematic diagram for non-contact mask-modulated electric field printing.	45
Figure 3.4 $I = 0.2A$. (CDC voltage, standoff distance = 75 μ m, pressure = 15inHg, pulse duration = 6.25/400msec., exposure = 60sec., electrolyte = 1.80M H_2SO_4 + 0.25M $CuSO_4$)	46
Figure 3.5: Polymer sheet with single drilled 2mm hole, comparison of pressure variation at 1.25X. (a) $P = 0$ inHg (b) $P = 4$ inHg (CDC voltage, standoff distance = 10 μ m, current = 0.05A, pulse duration = 0.5/50msec., exposure = 15sec., electrolyte = 1.80M H_2SO_4 + 0.25M $CuSO_4$)	47
Figure 3.6 Schematic diagram depicting Uniform Electric Field Mask Printing	47
Figure 3.7: Mask printing under uniform DC voltage (0.1V, standoff distance = 20 μ m, $P=1.0$ inHg, exposure = 30sec., electrolyte = 0.01M H_2SO_4 + 0.5M $CuSO_4$).	48
Figure 3.8 Variation of imprinted profile with various values of standoff distance between anode and cathode	50
Figure 3.9 Variation of α (surface angle) with standoff distance between anode and cathode (H), comparison of experimental and numerical values	51
Figure 3.10 Variation of depth of surface profile (D) with standoff distance between anode and cathode (H), comparison of experimental and numerical values	52
Figure 3.11 Variation of width of surface profile (W) with standoff distance between anode and cathode (H), comparison of experimental and numerical values	53
Figure 3.12 Schematic depicting the imprinted profile along with the fitting line used to calculate surface angle (α)	54
Figure 3.13 Variation of imprinted profile with various values of half-pitch of cell	56

Figure 3.14 Variation of Electric field on anode surface with half cell width	57
Figure 3.15 Variation of imprinted profile with opening radius. Variation shown for small opening radius 100 nm-1 μ m	60
Figure 3.16 Variation of imprinted profile with opening radius, at intermediate values (1 μ m – 200 μ m), showing the increase and subsequent decrease in depth of cut.	61
Figure 3.17 Variation of imprinted profile with opening radius at large value of the radius(200 μ m – 1700 μ m)	62
Figure 3.18 Variation of imprinted profile shifted by the opening radius W	63
Figure 3.19 Variation of imprinted profile with various opening radius, mask thickness (T_{mask})=75e-6 m	64
Figure 3.20 Variation of Electric field with Opening radius, using conductive media model	65
Figure 3.21 Variation of the imprinted profile with standoff distance between mask and anode ($=T_{gap} + T_{membrane}$), for $W / (T_{gap} + T_{mask}) = 1$	66
Figure 3.22 Variation of the imprinted profile with standoff distance between mask and anode ($=T_{gap} + T_{membrane}$), for $W / (T_{gap} + T_{mask}) = 3$	67
Figure 3.23 Variation of the imprinted profile with standoff distance between mask and anode ($=T_{gap} + T_{membrane}$), for $W / (T_{gap} + T_{mask}) = 5$	68
Figure 3.24 Variation of imprinted profile with change in the standoff distance between mask and anode.	71
Figure 3.25 Variation of imprinted profile with various values of membrane thickness	72
Figure 3.26 Variation of imprinted profile with various values of mask thickness, for mask opening =1e-4 m	73
Figure 3.27 Variation of imprinted profile with various values of mask thickness, for mask opening =3e-4 m	74
Figure 3.28 (a)Variation of the imprinted profile with eccentricity/curvature of membrane, eccentricity = h/w. While eccentricity is not equal to the curvature it is proportional to the curvature of the membrane. (b) Schematic depicting the eccentricity of the membrane.	76
Figure 3.29 Variation of Dimensionless Copper concentration over anode surface, with time, mask opening= 200e-6 m	78
Figure 3.30 Variation of the concentration profile on anode surface with time, at long time scales	79
Figure 3.31 Variation of Effective surface overpotential($(V - V_{cu}) - U_{anode}$) along anode surface, mask opening= 200e-6 m	80
Figure 3.32 variation of the Surface Overpotential at the anode surface, at long time scales	81

Figure 3.33 Variation of anodic current density with time, mask opening= 200e-6 m	82
Figure 3.34 Variation of the current density at anode surface, at long time scales	83
Figure 3.35 Variation of imprinted surface profile, mask opening= 200e-6 m	84
Figure 3.36 Variation of the imprinted surface profile, at long time scales.	85
Figure 3.37 Variation of the average slope of the anode surface within the mask opening with time. Note that the shown slope slightly understates the actual slope due to the nature of the calculation.	86
Figure 3.38 Variation of Ratio H_{d1}/H_{d0} with time. H_{d1} =displacement of bottom most point on the profile from the original anode surface, H_{d0} =displacement at the center of the mask opening	87
Figure 3.39 Variation of the imprinted profile with potential difference between anode and cathode	90
Figure 3.40 Variation of Material removal rate with current from experimental setup for Non-contact mask modulated electric field printing	91
Figure 3.41 Variation of Material removal rate (nm/s) with current (experiment) and voltage(simulation) respectively.	92
Figure 3.42 Variation of dimensionless imprinted profile depicting the flattening of the bottom surface with increasing potential difference between anode and cathode.	93
Figure 3.43 Experimentally obtained profile using stainless steel 570 μm mask, (a) $I= 1.052 \text{ A}$ (b) $I=1.885 \text{ A}$ (DC voltage, standoff distance = 150 μm . Exposure = 300 sec, electrolyte = 1.80 M H_2SO_4 + 0.25 M CuSO_4)	94
Figure 3.44 Variation of imprinted profile with/without H_2SO_4 at time $t=.04$ seconds	96
Figure 3.45 Variation of imprinted profile with various concentrations of H_2SO_4	97
Figure 3.46 Variation of Copper Ion Concentration with concentration of sulphuric acid	98
Figure 3.47 Variation of Potential at Electrolyte-Anode Interface with sulphuric acid concentration	99
Figure 3.48 Perforated stainless steel 570 μm , comparison of MRR at different electrolyte concentrations. (DC voltage, Insulated perforated stainless steel hole, insulated cathode chamber with added round electrode, $P = 1\text{inHg}$, standoff distance = 20 μm , exposure = 60sec.)	100
Figure 3.49 Variation of Dimensionless MRR (nm/s) with concentration of sulphuric acid	101
Figure 3.50 Variation of imprinted profile with various values of mask dielectric constant.	103
Figure 3.51 Variation of imprinted profile with various values of mask dielectric constant.	104

LIST OF TABLES

Table 1 Advanced Meshing Parameters	36
Table 2 Parameters and their Corresponding value for Nerst-Planc equation	37
Table 3 Parameters and their corresponding value for Poisson's Equation	38

ABSTRACT

FEFIIT is a unique method, which can be utilized to imprint complex structures on the surface of a conducting substrate. Experimental results have shown that under certain conditions, it is possible to obtain surface structures with characteristic length smaller than that of the mask. DC chopped simulations in particular yield unique features, which can be exploited to yield high aspect ratio structures. In this thesis, a model of this process is established and studied. Studies are conducted on the various length scale parameters as well as the starting concentration, and the potential applied. Two independent dimensionless parameters are found to profoundly affect the shape of the surface structure formed. Further, a qualitative reasoning for the DC chopped simulations are provided.

CHAPTER 1 INTRODUCTION: LITERATURE REVIEW

The emerging field of nanotechnology has opened up a new field in which engineered nanostructures interact with biological molecules to create drugs and medical technology with much higher efficiency. This has opened up uncharted areas of medicines such as personalized medicine, targeted drug delivery, smart drugs, advanced diagnostic biosensors, which aim to provide higher efficiency as well as lower costs to the user. Devices such as protein nanoarrays, micro/nanofluidics, microcantilevers, lab on chip devices are routinely used in such investigations. Conventional technology such as surface and bulk micromachining has been used to yield very good dimensional accuracy and at low costs for devices in the micrometer scale. However the fabrication of devices of characteristic length from 1 nm to 100 nm, could be problematic due to the expanding cost and complexity of optical lithography equipment and the inherent slowness of electron beam techniques.

In this thesis we study a novel method using simulations. This method can imprint micron size patterns on copper with wavy surfaces, (including full surface of revolutions such as ducts and pipes) with the hope of reducing the cost of fabrication as well as increasing its efficiency (Chandra et al, 2006, patent pending). The process is based on focused electric field induced ion transport (FEFIIT) across a membrane mediated electro-chemical cell. It has a number of unique features: a) a feature reduction ratio of 3:1 b) The working distance and the depth of field or depth of focus in FEFIIT is about 2 to 3 orders of magnitude higher than that of a comparable Lithography process ($O(10\mu\text{m})$) c) the process is environmentally benign, since the electrolyte is separated from the anode, and can thus be recycled. d) no residual stress formed in the copper plate, since the process is a non-contact method e) the process can be easily parallelized and f) the capital cost of the process is low. The process is also applicable to other conductors.

FEFIIT is a unique process in which a metal substrate is anodically oxidized under a “focused” electric field. The device consists of a modified electrolytic cell, the

anode being the 99.99% pure copper substrate to be etched, and the cathode being a platinum or copper electrode. The anode and cathode are separated by an ion-selective membrane (Nafion) which permits the transfer of copper ions to the cathode, but inhibits flow of the sulphate ions. The copper anode is submerged in DI water, while the cathode is immersed in an electrolyte consisting of H_2SO_4 and CuSO_4 . This separation of the electrolyte from the cathode is achieved by using an anion (SO_4^{2-}) impermeable Nafion (Nafion is trademark of DuPont Co.) that prevents contamination of the cathode by the sulphate ions. The membrane is supported using a perforated mask which also provides the specific dimensions of the structures to be created on the substrate.

In the following sections a literature survey of the different mechanisms/processes occurring at different regions in the chamber, is provided.

1.1. Various Similar Processes Studied Earlier

Modeling of processes involving electrodeposition and electrodisolution has been a topic of study for a long time. While continuum based models have been used to predict material removal or addition rates for various processes in the macroscale, microscale processes are difficult to model using similar models. This is because at that scale the process becomes inherently stochastic, and only stochastic models can give quantitative results for such processes. Electrodeposition studies using macroscopic models have been studied by Alkire et al[1-4]. In these studies, the authors simulated various electrodeposition systems using continuum techniques. However quantitative match between theory and experiments were not obtained. To obtain such quantitative matches, the authors also performed various multiscale hybrid simulations combining kinetic monte carlo and Nerst-Planck-Poisson equations to arrive at results which provided very good match between theory and experiments. [5-14]

1.2. Electrode Processes and Formation of Anodic Films

The first study of the kinetics of deposition and dissolution of Cu/CuSO₄ solution was carried out by Mattsson and Bockris in 1958[15]. They used galvanostatic measurements to measure the dissolution/deposition of Copper at very fine time intervals such that only a few monolayers per pulse were deposited or dissolved. The variation of activation overpotential at constant high current density ($\sim 10e-2$ A/cm²), with time was found to be very similar to that of a resistance and capacitance in parallel, indicating that the deposition/dissolution rates were determined by the presence of the double layer as well as the charge transfer process. They showed the existence of the reduction-oxidation (redox) reaction process between Cu²⁺ and Cu⁺ whilst Cu⁺ exists in reversible equilibrium with Cu at the electrode surface. At low current densities ($\sim 1e-2$ A/cm²), the rise of the activation overpotential is slower than that observed at higher current densities. The overpotential observed was higher than predicted by Butler Volmer equation. This phenomenon was explained using a model proposed by Mehl and Bockris [16] which stated that the rate controlling step at low current densities was determined by the surface diffusion of adions.

Kinetic studies on the short time deposition and dissolution of copper in various solution of copper salts (sulphate, chloride, perchlorate, acetate and aminosulphonate) and their corresponding acids were carried out by a galvanostatic transient method by Bockris and Enyo[17]. Further they studied the effect of different electrode preparation techniques on the current density. It was found that electrodes prepared by electrodeposition had higher current densities for the same surface overpotential compared to electrodes prepared by melting in helium. This was assigned to the fact that electrodeposited copper electrodes had higher surface dislocations which consequently formed sites for deposition or dissolution. Their experiments confirmed the importance of double layer formation and the intermediate Cu⁺ formation in determining the current density. These and other studies show that while it is possible that surface films/anodic films might form in

cases where electrodissoolution is carried out in basic solutions, surface films are not formed when electrodissoolution/deposition is carried out in acidic solutions.

The above models have been recently implemented in numerical models by Pirogov et al [18-20]. These models consider incomplete dissociation of CuSO_4 and H_2SO_4 . The concentrations of the individual ions are governed by chemical equilibrium conditions. Further the dissolution of CuSO_4 is assumed to occur via the 2 step process instead of the one step process. A total of 5 ions $\text{Cu}^{2+}, \text{Cu}^+, \text{HSO}_4^-, \text{SO}_4^{2-}, \text{H}^+$ are considered to be simultaneously present in the solution. CuSO_4 and H_2SO_4 are considered to be incompletely dissociated. Migration and diffusion of the individual ions are simultaneously considered. These models give rise to results which qualitatively match experimentally determined current vs voltage curves.

1.3. Ion and water transport through Nafion

There are three main categories of models, (a) the simple approaches, (b) the diffusive approach, (c) the hydraulic approach, and (d) their combination.

1.3.1 Simple models

The simplest models of the membrane that treat transport in the membrane in a nontrivial manner (i.e., they consider species transport and not just fit a polarization curve with empirical parameters) make several assumptions and use some simple transport expressions along with material conservation equations. These models are aimed at examining effects outside the membrane (e.g., cathode flooding [21]) or when only general trends are desired [22]. Furthermore, these models assume constant values of transport properties in the membrane and thus are not applicable when the water content of the membrane is expected to vary (e.g., membrane dehydration). Such assumptions also limit the predictability of these models. Since the membrane is stationary, only the water and protons move in the membrane system. For the proton movement, the simplest treatment is to use Ohm's law. For the movement of water through the membrane, a value of β , the net water flux per

proton flux, is often assumed or is calculated based on the water flux in the anode or cathode region. Most models that use this approach also treat the catalyst layer as an interface, which allows for the water flux to become a boundary condition that is directly related to β . While this approach has merit in terms of convergence issues and allowing for analytic expressions to describe the membrane, it has limited usage under most fuel-cell conditions since β is not known a priori.

1.3.2 Diffusive models

The diffusive models treat the membrane system as a single, homogeneous phase in which water and cations/anions dissolve and move by concentration and potential gradients. They correspond more-or-less to the vapor-equilibrated membrane, or in other words a membrane at lower water content. Many membrane models, including some of the earliest ones, treat the system in such a manner. The diffusive models allow one to predict such effects as membrane dehydration. As the current density is increased, the water content of the membrane decreases, causing a larger ohmic drop due to its effect on conductivity. Furthermore, the profiles become more curved as the current density is increased because of the interactions between the water gradient and electro-osmotic fluxes in the membrane. There are two main ways in which the diffusive transport can be treated, first by dilute solution theory and second by concentrated solution theory. The former approach is simpler to implement and may yield sufficiently correct answers, especially in terms of current density. However, it lacks the universality and rigor of the latter approach, which can be applied for all water contents.

1.3.2.1 Dilute solution theory

Dilute solution theory starts with the use of the Nernst-Planck equation [23] which represents the total ion transport as a sum of migration, diffusion and convection of ions. Dilute solution theory considers only the interactions between

each dissolved species and the solvent. The motion of each charged species is described by its transport properties, namely, the mobility and the diffusion coefficient. These transport properties can be related to one another via the Nernst-Einstein equation [24]. So long as the solute species are sufficiently dilute that the interactions among them can be neglected, material balances can be written. This theory has been utilized in a number of studies to model the transport through Nafion membranes. Since this model is relatively simple, and the characteristic parameters necessary to model Nafion for transport of different cations and anions such as Cu^{2+} , H^+ , SO_4^{2-} etc are easily available, this model has found wide spread use in modeling of PEM fuel cells ([25]).

1.3.2.2 Concentrated solution theory

Concentrated solution theory takes into account the binary interactions between all of the species. In addition, it uses a more general driving force, namely, that of chemical potential. This allows for the concentrated-solution-theory equations to be valid for both the diffusive and hydraulic models, the only difference being in the interpretation of the chemical potential. Consequently, if concentrated solution theory is used, the model can easily become a combination one (i.e., valid for all water contents). For membranes, concentrated solution theory was initially used by Pintauro and Bennion [26]. To do the analysis, one starts with the equation of multicomponent transport. As discussed by Fimrite et al. [27], this treatment is similar to that of the dusty-fluid model applied to the membrane [28], but accounts for the bulk movement of water in a more consistent manner using a different reference frame. This analysis is akin to the analysis of gas movement in porous media presented by Weber and Newman [29]. It should be noted that since the above treatment also implicitly accounts for convection, the model is more of a combination model and not just a diffusion one, as mentioned in the next section. A proton and water interaction can then be used to model the transport in the membrane, which results in equations similar to Nernst-Planck. The models that use

the above formulation are primarily focused on modeling the conductivity of the membrane. However these models are somewhat complicated and requires predicting or measuring the necessary binary interaction parameters.

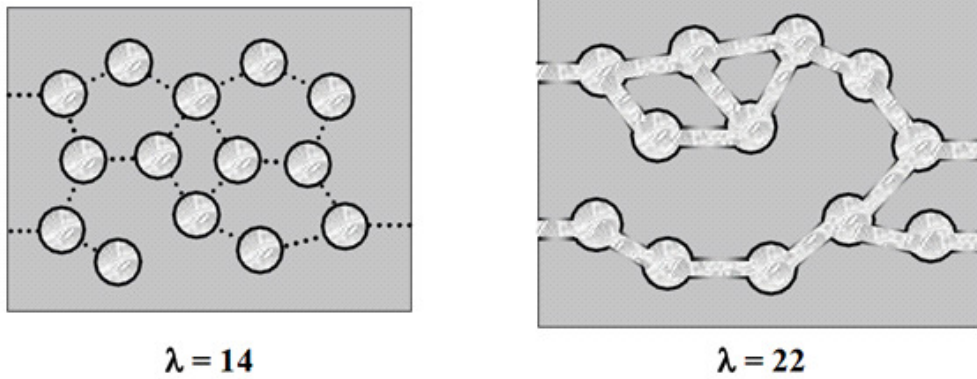


Figure 1.1 Membrane structure and interactions as a function of water content λ (moles of water per mole of sulphonic acid sites). The black regions are the fluorocarbon backbones, the grayish-white regions inside the black regions are the water molecules, the dotted black regions correspond to the collapsed membrane configuration

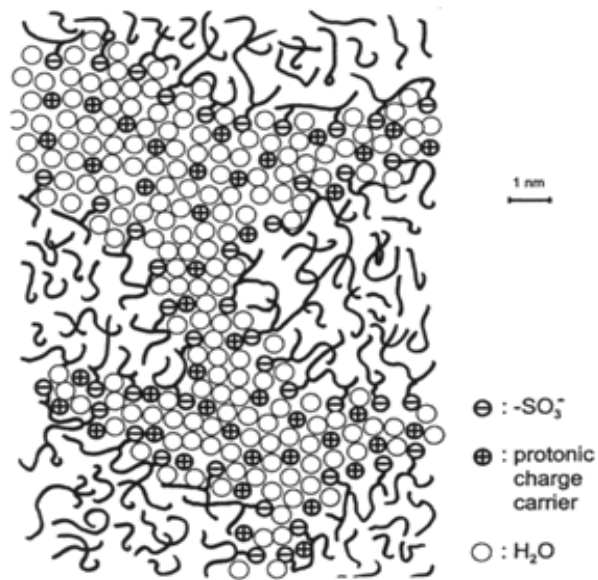


Figure 1.2 Schematic depicting a microscale model with sulphonic ions, water molecules and hydrogen ions

1.3.3 Hydraulic models

In contrast to the single-phase treatment above are the models that assume the membrane system as two phases. This type of model corresponds to the liquid-equilibrated membranes as shown in Figure 1.1 and Figure 1.2 (i.e., high water contents where there is a bulk-like liquid-water phase in the membrane). In this model, the membrane is treated as having pores that are filled with liquid water. Thus, the two phases are water and membrane. The addition of a second phase allows for the membrane system to sustain a pressure gradient in the water because of a possibly unknown stress relation between the membrane and fluid at every point in the membrane. The phenomenon of diffusion assumes two or more phases, one of which is stationary and the rest mobile. The stationary phase is typically not modeled directly since its concentration, flux etc are not important. If on the other hand, the stationary phase itself is modeled directly, as is done here, (since the water is modeled as flowing through a capillary pore, where the pore walls are made up of the stationary fluorocarbon/sulphonic acid groups), diffusion doesn't have any meaning. Furthermore, unlike the models discussed in earlier sections, the water content of the membrane is usually assumed to remain constant as long as the membrane remains fully liquid equilibrated and has been pretreated appropriately. For the transition case between liquid- and vapor-equilibration, see section 1.3.4. The first model to describe the membrane using a hydraulic approach was that of Bernardi and Verbrugge [30-31], which was based on earlier work by Verbrugge and Hill [32-33]. This model utilizes a dilute solution approach that uses the Nernst-Planck equation to describe the movement of protons, except that now the velocity of protons/ions is not equal to zero because they move in the separate water phase. The velocity of the water is given by Schlögl's equation [34]. In the above system, the movement of water can be attributed to a potential gradient and a pressure gradient. The movement of water by a pressure gradient is determined primarily by an effective permeability of water moving through the pore network. This approach is quite useful for describing fuel-cell systems as long as the membrane is well

hydrated with uniform water content. Such a treatment does not necessarily lend itself to describing the flux of water resulting when there is a water-activity gradient across the membrane (i.e., when the membrane is not fully hydrated). Many other models use the same approach and equations as Bernardi and Verbrugge, especially for systems wherein the membrane is expected to be well hydrated (e.g., saturated gas feeds) [35]. Instead of the dilute solution approach above, concentrated solution theory can also be used to model liquid-equilibrated membranes. An interesting aspect of hydraulic models is that the water-pressure profile inside the membrane is essentially linear. This is because the water content and consequently the properties are assumed uniform. Also, this assumption means that the net water flux in the membrane should be constant with respect to current density because all of the transport is linearly proportional to the current density. While this is true for the case of a zero pressure difference, it is not the case when there is a pressure differential because this is an extra force driving water from the cathode to the anode. However, under these conditions a hydraulic model may not be valid, which is why the predicted β values are lower than those usually observed [36]. In other words, the pressure effects are over emphasized if one only uses a hydraulic-model approach. Overall, as long as water is on both sides of the membrane, the hydraulic treatment remains valid, and the effect of pressure difference is significant.

1.3.4 Combination models

The two approaches above can be contrasted to one another. In the first approach, (section 1.3.2) water moves by diffusion and pressure-driven flow is excluded as a separate driving force. In the second approach, only pressure-driven flow is used and there is no diffusive flow. Furthermore, the former approach assumes one phase and the latter two phases. In essence, the diffusive models describe transport in vapor-equilibrated membranes, and the hydraulic models in liquid-equilibrated ones. Thus, to model the full spectrum of water contents, some kind of superposition of the two is required [37]. In other words, a model for the

transition region between the two modes is necessary. Perhaps the easiest way to do the superposition is to combine linearly the two driving forces for water, as many models have done [38]. In essence, this is a dilute solution approach and the two driving forces should not necessarily be valid for all water contents. Furthermore, the addition of both driving forces means that an extra variable is being added to the set of unknowns, and consequently an additional relation is required (e.g., assumption of equilibrium between the concentration and pressure). While this treatment is neither really rigorous nor consistent, it does help to fit and explain data. Before discussing other approaches, it is of interest to examine the magnitude of the terms. Because a single-phase model cannot sustain a pressure gradient, Meyers [39] included pressure-driven flow by allowing for a discontinuity in pressure at the membrane/solution interface, even though the electrochemical-potential of all soluble species is continuous. He argues that the additional mechanical stresses compressing the membrane should be indistinguishable from the thermodynamic pressure, and thus the thermodynamic pressure might be discontinuous at the interface. In essence, this approach is similar to using the chemicalpotential, concentrated-solution-theory approach described below, although it is not as consistent. The most consistent and rigorous approach for modeling the transition region and the whole spectrum of water contents is to use concentrated solution theory. As noted above, such an approach accounts for both convection and diffusion in the membranes. While multiple dilute solution approaches have been used for the various water contents, the concentrated-solution theory approach and equations are independent of the water content. The key is using the correct parameter values and in the interpretation of the single driving force of chemical potential.

1.4. Electrolyte transport/Modeling of Nafion membrane

As stated in earlier sections, electrolytic transport can be represented in two different ways: using dilute solution theory and concentrated solution theory. The details and the background on both these methods have been stated in earlier

sections. In the model developed in this thesis, we used dilution solution theory primarily because the parameters for this theory for different ions: copper, sulphate and hydrogen are easily available from the literature. It is much more difficult to obtain the necessary parameters for concentrated solution theory from literature. Further since concentrated solution theory is much more general, it requires better computation techniques. The modeling of deformation of Nafion membranes under electrical fields has seen significant improvements since 2000. While the exact structure of Nafion is not known till date, various approximations have been made to arrive at the deformation of Nafion. The initial modeling of Nafion deformation under electric fields were carried out by Nasser et al[40-41]. They studied the deformation of Nafion membranes using a micromechanics model under hydrated water sullen conditions. Their model accounts for coupled ion transport, electric field and elastic deformation to predict the response of the membrane. For their experiments they used an IPMC (ionic polymer metal composite) which consists of a thin Nafion sheet, plated with platinum on both sides. They also studied the effect of various ionic forms of Nafion immersed in different solvents. It was found that the nature of the solvent could have dramatic effects on the actuation of Nafion. [42]. Tadokoro et al[43], developed a white box model of Nafion-Pt taking into consideration the ionic motion by electric field, water motion by ion-drag, swelling and contraction of the membrane, momentum effect , electrostatic force and conformation changes. They were able to obtain quantitative match with experimental results especially on the time of maximum displacement, which was lacking in the conventional models proposed earlier. Tamagawa [44-46] studied the effect of various metals plated on to the IPMC. They used a simple cantilever model, for the Nafion deformation and found that Nickel plating instead of copper greatly increases the deflection of the membrane. Yamaue et al. [47] constructed the electrostress diffusion coupling model for the polyelectrolyte gels. The theory gives a microscopic expression for the Onsager coefficients in terms of the Stokes radius of the ion and size fo the micropores of the gel. Their model was able to qualitatively

explain the relaxation behavior of an ionic gel for various kinds of ions including large counterions such as tetraethylammonium. In recent years Porfiri [48-49] et al studied the actuation of Nafion membranes in details. They developed a physics based model for IPMC based sensing and actuation. Their model describes a variety of phenomenon such as counter ion, solvent and polymer motions; electric dipole generation; osmotic effects; boundary layer formation; polymer swelling; and local charge imbalances. Using this model they derived a reduced order plate like model equivalent to piezoelectric bimorph plates. Their model predictions are in close agreement with experimental results for mechanical stiffness, electric capacitance and sensing, actuation capacity of water hydrated Nafion in Na^+ form.

1.5. Transport properties of Nafion

To characterize the transport properties of Nafion, various techniques have been used since the 1950s. The first measurements to determine the nature of transport in Nafion membranes were done by Rubinstein using two electrode probes[50]. Their investigations showed that Nafion doesn't have a pure resistive nature, but also a capacitance type behavior. Later Cahan et al [51] used both two probe and four probe measurements to show that Nafion indeed had a resistive/conductive behavior rather than a combination of resistive and capacitative behavior. Their investigations showed that the prior results showing that Nafion had a capacitative behavior was incorrectly deduced and was merely an artifact of the two probe experiments. These results were later corroborated by various other researchers as well [52-57]. Another interesting characteristic noted in later experiments and modeling efforts were that Nafion need not have an isotropic behavior, but an anisotropic behavior. Results obtained by Silva et al [58], Casciola et al [59] and Ma [60] et al show that anisotropy of conduction might be significant at high temperatures. The transport properties of various ions through Nafion have also been characterized by various investigators. Among them we used data reported by Tsou et al [61] and Yeo et al[62]. They used an electrochemical test cell to

observe the diffusion coefficients and solubilities of hydrogen ions in Dow short-side-chain perfluoro-sulphonic and -carboxylic membranes. The conductivity/diffusivity of Sulphate were obtained from Unnikrishnan[63]. They conducted permeation studies of F^{-} , Cl^{-} , Br^{-} , NO_2^{-} , NO_3^{-} , and SO_4^{2-} and various cations such as K^{+} , Na^{+} , Cu^{2+} and Ca^{2+} , through Nafion-117 ionomer and also studied the effect of salt and pH of the feed solution.

The objective of this study will be to characterize the process using simulations. Chapter 1 provided a literature review of the various processes occurring at various regions in the electrochemical cell. In Chapter 2 we provide the details and theoretical derivations of the model derived from this literature survey, that we propose to use for our study. Chapter 3 describes the results from the numerical simulations. Finally Chapter 4 ends with the discussion of the results and provides details of future work that can be done.

CHAPTER 2 THEORY

2.1. Background

To study and explain the experimental features obtained, we undertake detailed theoretical investigations into the electrochemical origin of the features. Here we use a dilute transport theory to model the ion transport in the electrolyte. While there are more sophisticated models available for Nafion, here too we use the dilute transport theory. The reason for this is primarily that the parameters for more complicated phenomenon are not available in current literature and hence the models are difficult to use. Since the model used for the Nafion and the electrolyte are the same, we provide a detailed overview and background on dilute transport theory. To model the electrode kinetics and conversion of copper to copper ions, we model the interface by Butler-Volmer kinetics. Butler-Volmer describes the relation between the current density at the electrode-electrolyte interface and the surface overpotential. Next we describe the electroneutrality condition and derive it from the Poisson's equation. Finally we present the derivation of the displacement continuity equations which act to close the set of boundary conditions. We end by providing a complete set of governing equations for the three ions and the corresponding boundary conditions.

2.1.1 Dilute Solution Theory

While electrons in a conductor flow only in response to an electric field, ions in an electrolyte move in response to an electric field (a process called migration) and also in response to concentration gradients (diffusion) and bulk fluid motion (convection). The net flux of an ion is therefore the sum of the migration, diffusion, and convection terms. In the following sections we look at each of these individual phenomena separately.

2.1.1.1 Migration flux

When an electric field is created in a solution, it tends to drive ions in different directions depending on the charges on the ions. For example it drives cations or positively charged ions in the direction of the electric field, while negatively charged ions move in the opposite direction. The velocity of the ion in response to an electric field is its migration velocity, given by:

$$v_{i,migration} = -z_i u_i F \nabla \Phi \quad (1.1)$$

Where Φ is the potential in the solution, u_i , called the mobility, is a proportionality factor that relates how fast the ion moves in response to an electric field, z_i is the number of electronic charges on the i th ion and F is the Faradays constant. The Faradays constant quantifies the amount of charge per mole of ions containing 1 electronic charge on each molecule. The Flux density of a species is equal to its velocity multiplied by its concentration. Thus the migrational flux density is given by:

$$N_{i,migration} = -z_i u_i F c_i \nabla \Phi \quad (1.2)$$

Summing the migrational fluxes accordingly for a binary electrolyte, we see that the current density i , due to migration is given by:

$$i = -F^2 (z_+^2 u_+ c_+ + z_-^2 u_- c_-) \nabla \Phi \quad (1.3)$$

The ionic conductivity κ is defined as:

$$\kappa = F^2 (z_+^2 u_+ c_+ + z_-^2 u_- c_-) \quad (1.4)$$

Thus, the movement of charged species in a uniform solution under the influence of an electric field is also given by Ohm's law:

$$i = -\kappa \nabla \Phi \quad (1.5)$$

2.1.1.2 Diffusive flux

The concept of diffusion is derived from Fick's First Law. Fick's first law relates the diffusive flux to the concentration field, by postulating that the flux goes

from regions of high concentration to regions of low concentration, with a magnitude that is proportional to the concentration gradient (spatial derivative). In (spatial) dimension, this is:

$$J = -D \frac{\partial c}{\partial x} \quad (1.6)$$

where J is the diffusion flux [$\frac{mol}{m^2 s}$]. J measures the amount of substance that will flow through a small area during a small time interval, D is the diffusion coefficient or diffusivity in dimensions of [$length^2 time^{-1}$] [$(\frac{m^2}{s})$], c is the concentration in dimensions of (*amount of substance*) $length^{-3}$, [$\frac{mol}{m^3}$], and x is the position.

D is proportional to the squared velocity of the diffusing particles, which depends on the temperature, viscosity of the fluid and the size of the particles according to the Stokes-Einstein relation. In dilute aqueous solutions the diffusion coefficients of most ions are similar and have values that at room temperature are in the range of $0.6e-9$ to $2e9 m^2 / s$. For biological molecules the diffusion coefficients normally range from $1e-11$ to $1e-10 m^2 / s$. In two or more dimensions we must use ∇ , the del or gradient operator, which generalizes the first derivative to obtain :

$$\vec{N}_{i,convection} = -D \nabla c \quad (1.7)$$

2.1.1.3 Convective flux

Convection is the bulk movement of a fluid. The equations describing fluid velocity and convection is governed by the Navier Stokes equation given by:

$$\rho \left(\frac{\partial \vec{v}}{\partial t} + \vec{v} \cdot \nabla \vec{v} \right) = -\nabla p + \mu \nabla^2 \vec{v} + f \quad (1.8)$$

Where \vec{v} is the velocity of the fluid, ρ is the density of the fluid, p is the pressure, and μ is the viscosity of the fluid.

The flux density of a species by convection is given by:

$$\vec{N}_{i,convection} = c_i \vec{v} \quad (1.9)$$

where \vec{v} is the velocity of the bulk fluid. Convection includes natural convection (caused by density gradients) and force convection (caused by mechanical stirring or a pressure gradient). Convection can be laminar, meaning that the fluid flows in a smooth fashion, or turbulent, in which the motion is chaotic. Hence the net current density at any point in the fluid medium taking place due to convection can be obtained as:

$$i_{convection} = \sum_i z_i c_i F v \quad (1.10)$$

The condition of electroneutrality as discussed below states:

$$\sum_i z_i c_i = 0 \quad (1.11)$$

Therefore, in an electrically neutral solution, bulk convection alone does not cause a net current. However, convection can cause mixing of the solution, and while it alone cannot cause a current, fluid motion can affect concentration profiles and serve as an effective means to bring reactants to the electrode surface.

From the above phenomena, we can calculate the net flux due to a combination of migration, diffusion and convection which can be written as:

$$N_i = -z_i u_i F c_i \nabla \Phi - D_i \nabla c_i + c_i v \quad (1.12)$$

Mass transfer in an electrolyte requires a description of the movement of mobile ionic species, material balances, current flow, electroneutrality, and fluid mechanics. The flux density N_i of species i , is a vector quantity indicating the direction in which the species is moving and the number of moles going per unit time across a plane of 1 cm^2 , oriented perpendicular to the flow of the species. This movement is due first of all to the motion of the fluid with the bulk velocity v . However, the movement of the species can deviate from this average velocity by diffusion if there is a concentration gradient ∇c_i or by migration if there is an

electric field $-\nabla\Phi$ and if the species is charged (z_i is the number of proton charges carried by an ion).

The migration term is inherent to all electrochemical systems or systems containing charged species acted on by an electric field. Here Φ is the electrostatic potential whose gradient is the negative of the electric field. These are not quantities that can be measured easily and directly in a liquid solution. The quantity u_i is called the mobility and denotes the average velocity of a species in the solution when acted upon by a force of 1N/mol, independent of the origin of the force. Thus z_iF is the charge per mole on a species. Multiplication by the electric field $-\nabla\Phi$ gives the force per mole. Multiplication by the mobility u_i gives the migration velocity, and finally multiplication by the concentration c_i gives the contribution to the net flux density N_i due to migration in an electric field.

The three components stated above can then be combined and stated in a differential format as follows:

$$\frac{\partial c_i}{\partial t} = -\nabla \cdot N_i + R_i \quad (1.13)$$

Here the left hand side corresponds to the accumulation term, the first term on the right hand side corresponds to the net input to the control volume and the second term on the right corresponds to the production term or generation term (in case there is any chemical reaction).

For net input, it is necessary to compute the net amount of material brought in by the different fluxes on the various faces of the volume element. The differences in fluxes going out of the control volume and coming into the control volume, contribute to accumulation or depletion. The production per unit volume R_i involves homogeneous chemical reactions in the bulk of the solution, but not any electrode reactions, which occur at the boundaries of the solution. In electrochemical systems, the reaction is frequently limited to electrode surfaces, in which case R_i is zero.

2.1.2 Electroneutrality condition

Finally, we can say that the solution is electrically neutral i.e.

$$\sum_i z_i c_i = 0 \quad (1.14)$$

Such electro-neutrality is observed in all solutions except in a thin double charge layer near electrodes and other boundaries. This double layer may be of the order of 1 to 10 nm in thickness. The phenomena related to the double layer at the electrodes can usually be taken into account by the boundary conditions. Hence, it is reasonable to adopt the above equation in a description of the bulk of a solution.

However it should be remembered that electroneutrality is not a fundamental law of nature. A more accurate description of the potential would be Poisson's equation, which for a medium of uniform dielectric constant, reads:

$$\nabla^2 \Phi = -\frac{F}{\epsilon} \sum_i z_i c_i \quad (1.15)$$

and relates the charge density to the Laplacian of the electric potential. The proportionality constant in this equation is Faraday's constant F divided by the permittivity or dielectric constant ϵ . The value of the proportionality constant is quite large (1.392e16 V.cm/equiv for a relative dielectric constant of 78.303), so that what, in terms of concentrations, would be a negligible deviation, amounts to a considerable deviation from the perspective of electroneutrality, or in other words, from Laplace's equation for the potential.

Another way of saying the same is that F/ϵ is so large that an appreciable separation of charge would require prohibitively large electric forces. Still another way is that the conductivity is so large that any initial charge density would be neutralized very rapidly or would rapidly flow to the boundaries of the solution.

2.1.3 Electrode Kinetics

For a single electrode reaction occurring in a steady state, the rate of the reaction is related in a simple manner by Faraday's law to the current density i_n

The rate of the electrode reaction, characterized by the current density, depends first on the nature and previous treatment of the electrode surface. Second, the rate of reaction depends on the composition of the electrolytic solution adjacent to the electrode, just outside the double layer. This may be different from the composition of the bulk solution because of limited rates of mass transfer. However, the diffusive part of the double layer is regarded as part of the interface. It is too thin to probe adequately, and the theory of the diffuse layer is a microscopic model rather than a macroscopic theory.

Finally the rate of the reaction depends on the electrode potential. This electrode potential is characterized by the surface overpotential η_s defined as the potential of the working electrode relative to a reference electrode of the same kind placed in the solution adjacent to the surface of the working electrode (just outside the double layer). This is a macroscopically well-defined potential and can be expressed in terms of electrochemical potentials. For the general electrode reaction, the equilibrium condition is:

$$\sum_i s_i \mu_i = n \mu_{e^-} \quad (1.16)$$

The surface overpotential η_s expresses the departure from the equilibrium potential and is given by:

$$F \eta_s = F (\Phi_{electrode} - \Phi_{solution}) = -\mu_{e^-} + \sum_i \frac{s_i}{n} \mu_i \quad (1.17)$$

where the chemical potential of the electrons μ_{e^-} is related to the potential Φ by

$$\mu_i = z_i F \Phi \quad (1.18)$$

where z_i is negative for the electrons.

The driving force for electrochemical reactions η_s , the surface overpotential can be defined in three different ways:

- a) The potential of the electrode minus that of a reference electrode of the same kind and located adjacent to the surface
- b) The potential of the electrode (relative to the solution) minus the value at equilibrium or open-circuit.
- c) The electrochemical potential of electrons in the electrode compared to the electrochemical potentials of other participants in the electrode reaction.

The reaction rate thus goes to zero at $\eta_s = 0$, for any composition or reaction surface. For analyzing the behavior of electrochemical systems, we seek the macroscopic relationship between the current density and the surface overpotential and the composition adjacent to the electrode surface:

$$i_n = f(\eta_s, c_i) \quad (1.19)$$

Microscopic models may be useful in correlating these results, although they are not essential. Transient electrode processes can also involve the double-layer capacity and possibly hysteresis related to changes in the surface of the electrode. While the equation (1.19) can be characterized by experiments, we use a theoretical model used widely in electrochemical simulations, known as Butler-Volmer equation and use parameters for the Butler Volmer equation from literature. The details of the Butler Volmer equation and its derivation are provided in the following section.

2.1.3.1 Theoretical Derivation of Butler-Volmer equation

As an example of the reversible reaction occurring at the anode/cathode, we consider the following reaction:



where O is the oxidized species and R is the reduced species. If only one reaction is occurring at the electrode, then the current is proportional to the net rate of reaction. The reactions in the cathodic and anodic directions occur simultaneously, each with its own dependence on the surface overpotential and reactant concentrations. The net rate of reaction r is equal to the difference

between the rate of the forward reaction and the rate of the backward reaction, and can be written as:

$$r = \frac{i_n}{nF} = k_a c_R \exp\left[\frac{(1-\beta)nF}{RT}V\right] - k_c c_O \exp\left(\frac{-\beta nF}{RT}V\right) \quad (1.21)$$

where k_a and k_c are the rate constant for the anodic and cathodic reactions, respectively, and c_R and c_O are the concentrations of the anodic and cathodic reactants, respectively. This implies that the cathodic and anodic reactions are first order in the reactants.

The above equation for the electrochemical reaction is similar to what one sees in ordinary chemical kinetics, with the additional factor for the dependence of the rates on the potential. The rate constants k_a and k_c would be expected to show an Arrhenius dependence on temperature, and they also depend on the nature of the electrode surface. The k 's and the exponential factors together represent Arrhenius rate constants with potential-dependent activation energies.

The symmetry factor β represents the fraction of the applied potential V that promotes the cathodic reaction. Similarly, $(1-\beta)$ is the fraction of the applied potential that promotes the anodic reaction. While it is frequently assumed that the symmetry factor has a value of $\frac{1}{2}$, experimental results deviate significantly.

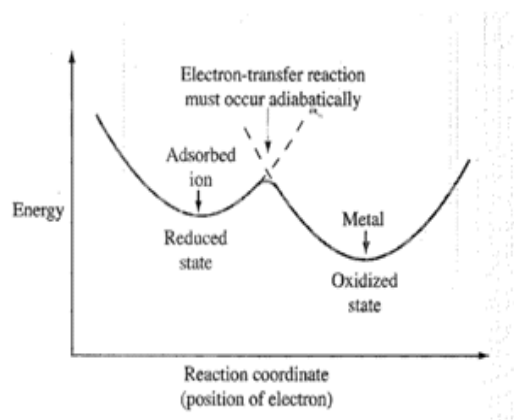


Figure 2.1 Energy diagram of an electron-ion system

The meaning of the symmetry factor β is illustrated above by means of a potential-energy diagram. Figure 2.1 above shows two upward opening parabolas describing adiabatic electron transfer at an active intermediate. The reaction coordinate can be thought of as the position of the electron during the transfer process. In Figure 2.2 the potential-energy curve for an applied potential V_1 is shown by a solid line, the activation energies E_a and E_c in the anodic and cathodic directions, respectively being indicated on the figure. A change of the applied potential from V_1 to V_2 results in a change of the energy of the reduced state relative to the oxidized state by an amount $nF(V_2 - V_1)$, and this tends to drive the reaction anodically if V_2 is greater than V_1 .

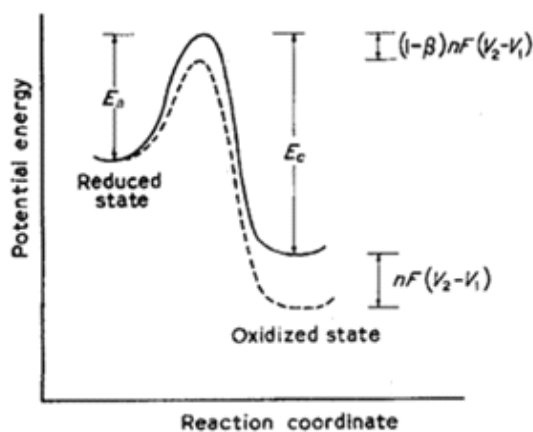


Figure 2.2: Potential Energy diagram for an elementary charge transfer step

If the applied potential is change from V_1 to V_2 , the potential-energy diagram is envisioned to change to the dashed curve. Then according to Figure 2.2, the activation energy in the cathodic direction increases by $\beta nF(V_2 - V_1)$, and the activation energy in the anodic direction decreases by $(1 - \beta)nF(V_2 - V_1)$:

$$E_{c2} = E_{c1} + \beta nF(V_2 - V_1) \quad (1.22)$$

$$E_{a2} = E_{a1} - (1 - \beta)nF(V_2 - V_1) \quad (1.23)$$

This corresponds to the exponential terms in (1.21) and illustrates how β is the fraction of the applied potential that favors the cathodic reaction.

At some value U of the potential difference V between the metal and the solution, the rate of the forward reaction and the rate of the backward reaction, and the net rate of reaction is zero. Then equation (1.21) becomes

$$k_a c_R \exp\left\{\frac{(1-\beta)nFU}{RT}\right\} = k_c c_O \exp\left\{\frac{-\beta nFU}{RT}\right\} \quad (1.24)$$

Further rearrangement yields:

$$U = \frac{RT}{nF} \ln\left(\frac{k_c c_O}{k_a c_R}\right) \quad (1.25)$$

a form of the Nernst equation. The potential at which the net rate of reaction is zero is known as the equilibrium potential, and the surface overpotential. η_s is defined as the difference between the actual potential and the equilibrium potential:

$$\eta_s = V - U \quad (1.26)$$

Substituting these two equations into equation (1.21) yields

$$\frac{i_n}{nF} = k_a c_R \exp\left[\frac{(1-\beta)nF}{RT} \eta_s + (1-\beta) \ln \frac{k_c c_O}{k_a c_R}\right] - k_c c_O \exp\left[\frac{-\beta nF}{RT} \eta_s - \beta \ln\left(\frac{k_c c_O}{k_a c_R}\right)\right] \quad (1.27)$$

With this definition of η_s and the exchange current density i_o defined by:

$$i_o = nF k_a^\beta k_c^{1-\beta} c_R^\beta c_O^{1-\beta} \quad (1.28)$$

Equation (1.27) can be written as

$$i_n = i_o \left\{ \exp\left[\frac{(1-\beta)nF}{RT} \eta_s\right] - \exp\left[\frac{-\beta nF}{RT} \eta_s\right] \right\} \quad (1.29)$$

This equation is known as the Butler-Volmer equation, often seen in the following form:

$$i_n = i_o \left\{ \exp\left[\frac{\alpha_a F}{RT} \eta_s\right] - \exp\left[\frac{-\alpha_c F}{RT} \eta_s\right] \right\} \quad (1.30)$$

Equation (1.27) shows that i_o depends on the composition of the solution adjacent to the electrode, as well as the temperature and the nature of the electrode surface. Comparison of equation (1.30) with equation (1.29) shows that $\alpha_a = (1 - \beta)n$ and $\alpha_c = \beta n$

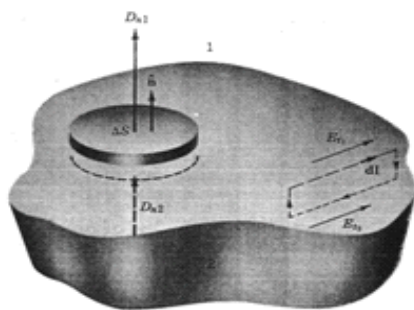


Figure 2.3 Boundary between two different media

2.1.4 Modeling of Interfaces

The Gauss' law in integral form states that if there is any free charge at any point in a medium, an integral of the electric displacement field over a closed surface surrounding the free charge is equal to the net charge within the volume enclosed by the surface of integral:

$$\Phi_{D,S} = \oint_S D \cdot dA \quad (1.31)$$

and

$$\Phi_{D,S} = Q_{free} \quad (1.32)$$

where D is the electric displacement field, $\Phi_{D,S}$ is the flux of the electric displacement field, and Q_{free} is the total free charge within the control volume.

The above theorem can be applied to an interface between two dielectric material to determine the boundary condition necessary for the Poissons equation stated earlier. Application of the integral form of Gauss's law to an infinitesimally small "pillbox" of thickness $h \rightarrow 0$ with upper surface S_1 parallel to S in medium 1

with outward normal $\hat{n}_1 = \hat{n}$ and lower surface S_2 parallel to S in medium 2 with outward normal $\hat{n}_1 = -\hat{n}$, gives:

$$\oint_{S_G} D \cdot ds = \iint_{S_1} D_1 \cdot \hat{n}_1 ds + \iint_{S_2} D_2 \cdot \hat{n}_2 ds = \rho_s \Delta s \quad (1.33)$$

where the contributions from the sides vanish as $\Delta h \rightarrow 0$ about S . Here $\rho_s = \rho_s(r)$, $r \in S$, denotes the surface charge density residing on the interface S . In the limit as $\Delta s \rightarrow 0$, one obtains

$$\hat{n} \cdot (D_1(r) - D_2(r)) = \rho_s(r), r \in S \quad (1.34)$$

Or

$$D_{n1}(r) - D_{n2} = \rho_s(r), r \in S \quad (1.35)$$

Here D_{n1} and D_{n2} are the normal components of the displacement field at the interface on sides 1 and 2 respectively and $\rho_s(r)$ is the surface charge at the interface. Assuming that the surface charge generated due to electric double layers is very small and the effect of double layers are negligible within the dielectric medium we can neglect the right hand side of (1.35) thus obtaining:

$$D_{n1}(r) - D_{n2} = 0 \quad (1.36)$$

or

$$\epsilon_1 E_{n1} = \epsilon_2 E_{n2} \quad (1.37)$$

2.2. Calculation of dielectric constant of membrane

The swollen Nafion can be regarded as a two-phase composite system, with hydrophilic clusters embedded in a hydrophobic polymer-backbone continuum. The effective dielectric constant of the two-phase composite can be expressed as[64]:

$$\kappa_e = (1-c)\kappa_1 A_1 + c\kappa_2 A_2 \quad (1.38)$$

where κ_1 and κ_2 are the dielectric tensors of phase 1 and 2, A_1 and A_2 are the corresponding field concentration tensors, and c is the volume fraction of phase 2. The concentration tensors are defined by:

$$\langle E_1 \rangle = A_1 E^0, \langle E_2 \rangle = A_2 E^0, (1-c)A_1 + cA_2 = I \quad (1.39)$$

where $\langle E \rangle$ denotes the volume average of E , E^0 is the electric field applied at the boundary, and I is the second-order unit tensor. It is clear that the determination of the effective dielectric constant depends on the determination of the concentration tensor. To do this, we adopt the Mori-Tanaka mean field approach[65], assuming that the average field, $\langle E_1 \rangle$ in phase 2, is equal to the average field in a single cluster embedded in an infinite matrix subjected to an external field equal to the yet-unknown average field, in phase 1, $\langle E_1 \rangle$:

$$E_2 = A_2^{dil} E_1, A_2^{dil} = [I + S \kappa_1^{-1} (\kappa_2 - \kappa_1)]^{-1} \quad (1.40)$$

where A^{dil} is a concentration tensor for the dilute distribution of clusters (i.e., no interaction with other clusters), and can be determined exactly, using Eshelby's equivalent-inclusion concept[66], S is the Eshelby tensor. For a spherical inclusion embedded in an isotropic matrix [67] $S_{11} = S_{22} = S_{33} = \frac{1}{3}$. From Equations (1.38), Equation (1.39) and (1.40), after some manipulation we obtain:

$$\kappa_e = \frac{\kappa_1 + \kappa_2 - c(\kappa_1 - \kappa_2)}{\kappa_1 + \kappa_2 + c(\kappa_1 - \kappa_2)} \kappa_1 \quad (1.41)$$

2.3. Calculation of deformation of membrane

Assuming the Nafion membrane to have a heterogeneous matrix structure, Nemat-Nasser derived expressions for the deflection of a Nafion membrane subjected to an external electric field. In their derivation, they assumed that the Nafion membrane is attached to two metallic electrodes on either sides of the membrane. Using this model they arrived at the following expression for the deflection:

$$u_x = \frac{z^2 + \nu x^2 - \nu y^2}{2R_c} \quad (1.42)$$

Where R_c is the imposed radius of curvature and ν is the Poissons ratio of the membrane. R_c is given as follows:

$$R_c = \frac{\bar{Y}I}{M} = \frac{2\bar{Y}h^2}{3k_0\kappa_e\phi_0 a} \quad (1.43)$$

Where \bar{Y} is the effective Youngs modulus of the composite, I is the cross-sectional moment of inertia, k_0 is a constitutive parameter, κ_e is the effective dielectric constant of the membrane, and ϕ_0 is the potential applied on the lower surface. The value of k_0 in terms of r_e , the effective radius of the polymer chain, r_d is the mean distance between two clusters, r_c is the cluster size, electronic charge e and effective dielectric constant κ_e is given as:

$$k_0 = \frac{e}{4\pi\kappa_e r_c^2} \frac{r_d^3}{\pi r_e^2} \quad (1.44)$$

Further the parameter a is given as:

$$a^2 = \frac{C^- F^2}{\kappa_e RT} \quad (1.45)$$

C^- being the number of negative charges in units of mol/m^3 , and F is the faradays constant.

2.4. Model equations

Using the above theory we can now write down the equations describing the physics of FEFIT. Here we consider the effect of three ions: Cu^{2+} , SO_4^{2-} , and H^+ . The ions are considered to be completely dissociated when in solution. Figure 2.4 shows a representative description of the geometry under consideration. While the experimental geometry is very complex, we consider a simplified model. The cathode as well as the anode is much wider than the opening holes, as such they are

considered infinitely wide. Further, we assume the condition surrounding each hole is self-similar, hence periodic. Hence we can apply periodic boundary conditions on the outer edges of the cell. At the inner edge, the cell is symmetric about the centerline, hence it is sufficient to simulate one half of it. Finally, it should be mentioned that we simulate the conditions in a two-dimensional space.

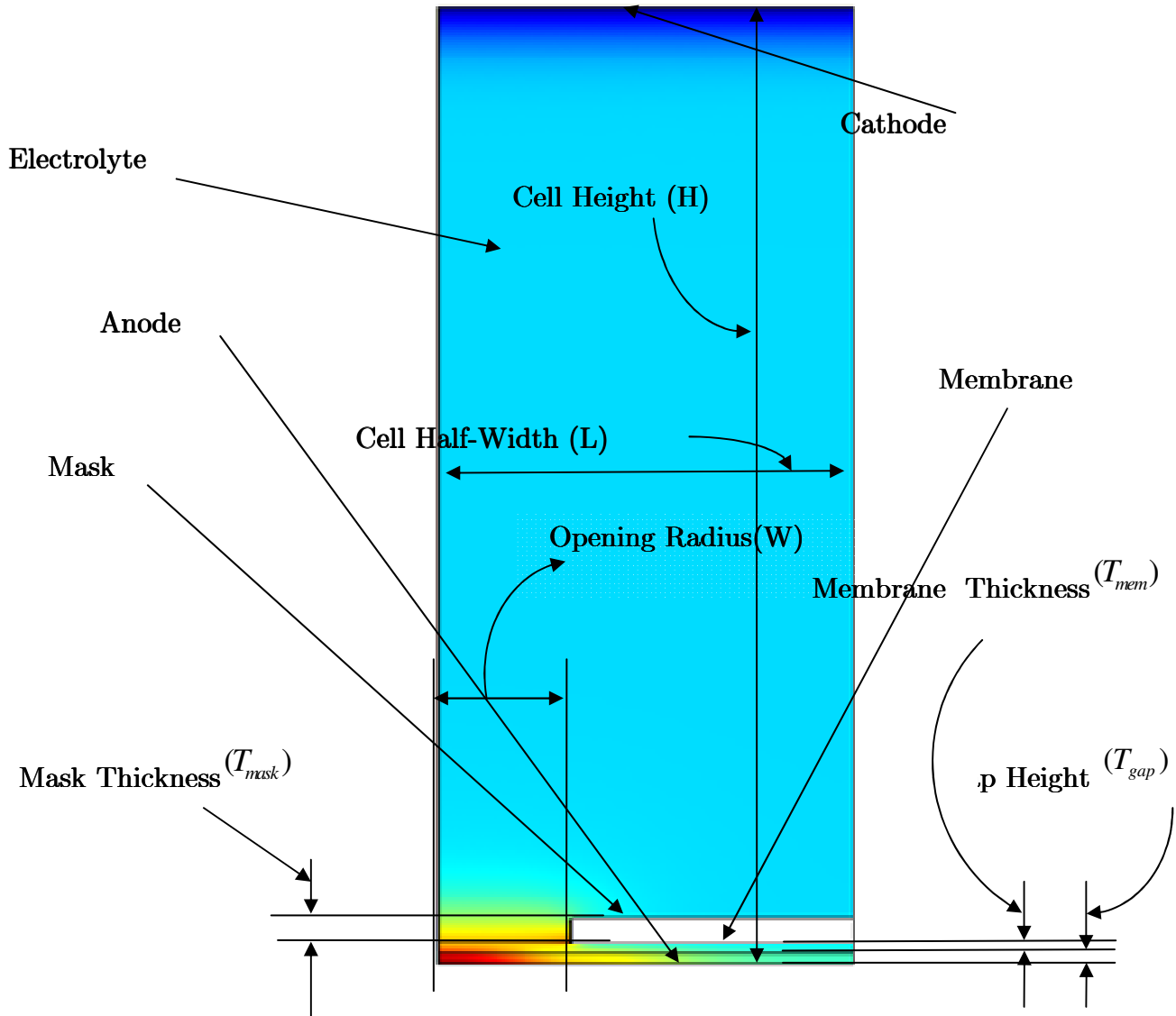


Figure 2.4 Schematic of model domain

2.4.1 Domain Equations

Using the theory of dilute solutions, as derived in section 2.1.1, we can now write down the equations governing the transport of the three species in the electrolyte and Nafion as follows

$$\frac{\partial c_{cu}}{\partial t} = z_{cu} F \nabla \cdot (u_{cu} c_{cu} \nabla \Phi) + \nabla \cdot (D_{cu} \nabla c_{cu}) \quad (1.46)$$

$$\frac{\partial c_{so_4}}{\partial t} = z_{so_4} F \nabla \cdot (u_{so_4} c_{so_4} \nabla \Phi) + \nabla \cdot (D_{so_4} \nabla c_{so_4}) \quad (1.47)$$

$$\frac{\partial c_H}{\partial t} = z_H F \nabla \cdot (u_H c_H \nabla \Phi) + \nabla \cdot (D_H \nabla c_H) \quad (1.48)$$

where the significance of the different terms have been explained earlier. In addition to the Nerst-Planck equations, we also have to take into consideration the Poisson equations which serves to evaluate the potential distribution in the domain as given by:

$$\nabla^2 \Phi = -\frac{F}{\epsilon} (z_{cu} c_{cu} + z_{so_4} c_{so_4} + z_H c_H) \quad (1.49)$$

The four governing differential equations determine the concentration distribution and the potential distribution within the electrolyte and Nafion. To simulate the effect of the mask, we consider it to be a impermeable dielectric material with a certain dielectric constant. Since, the flow of ions through the mask is negligible; we consider the concentration distribution of copper, sulphate or hydrogen ions in the dielectric to be zero. Further assuming that the molecules within the dielectric are fixed within the dielectric and don't dissociate into ions, we obtain the net charge distribution at any point within the mask to be zero. Hence applying the Poisson's equation to the mask we finally arrive at the Laplace equation as follows:

$$\nabla^2 \Phi = -\frac{F}{\epsilon} (z_{cu} c_{cu} + z_{so_4} c_{so_4} + z_H c_H) = 0 \quad (1.50)$$

2.4.2 Boundary Conditions

To close the four governing equations, we need at least four boundary conditions on each of the bounding surfaces of the different domains. At the interfaces between the Nafion and electrolyte; Nafion and mask; and mask and electrolyte, we apply the condition of dielectric continuity. At the interface between the Nafion and membrane, we consider that the electrolyte passes freely, while at the interface between the Nafion and mask; and electrolyte and mask; a no-flux boundary condition is applied. To simulate the periodicity at the outer edge of the cell, we apply a Neumann boundary condition on the concentration and potential distribution. Further due to the symmetry boundary condition at the center of the hole, the boundary condition there too reduces to Neumann boundary conditions on the concentration and potential distribution. The electrode kinetics in our problem is simulated using the Butler-Volmer equations. As stated earlier, the Butler-Volmer equation estimates the net current density from either electrode based on the difference in potential between the electrolyte surrounding the electrode and the potential at the electrode. The flux of the rest of the ions is set to zero, since sulphate or hydrogen ions are neither generated or adsorbed/absorbed on the surface of the electrodes.

2.5. Numerical simulation procedure

2.5.1 Mesh Generation:

An advancing front surface meshing technique is utilized to mesh the domain of interest. Triangles are built progressively inward from the discretized boundary of the domain. An active front is maintained where new triangles are formed. As the algorithm progresses, the front advances to fill the remainder of the area with triangles. In 2d, for each face of a triangle on the advancing front, an ideal location for the third point is computed. Also determined are any existing nodes on the front that may form a well-shaped triangle with the facet. The algorithm then selects

either the new third node or an existing node, which will form the best triangle. A check is also performed at this stage to ensure that the triangles don't overlap each other as the advancing front approaches each other.

2.5.2 Mesh Size:

The mesh size distribution is determined by the element sizes provided individually on each boundary, as well as the global maximum element size on the sub-domain. Smaller element sizes (maximum element length = 0.01) are used on the inlet, outlet and on the sphere, while relatively larger elements (maximum element length = 0.05) are used on the surface of the channel walls. A maximum element size of .1 is set within the domain of the flow. The element size necessary for a good solution should be small on the boundary, to capture the sharp gradients properly. However it is not necessary to have such small elements throughout. Table 1 specifies the other parameters necessary to build the surface mesh. The element growth rate determines the maximum rate at which the element size can grow from a region with small elements such as the boundary to a region with larger elements, in the interior of the domain. An element growth rate of 1.3 specifies that the element can grow at a rate of approximately 30% from one element to another. The value of the Mesh curvature factor determines the size of the boundary elements compared to the curvature of the geometric boundary. The curvature radius multiplied by the curvature factor, gives the maximum allowed element size along the boundary. A lower value gives a finer mesh along the boundaries. The parameter mesh curvature cutoff specifies the smallest radius of curvature captured by the meshing method. When the radius of curvature is smaller than the Mesh Curvature times the maximum distance in the geometry, the mesh generator considers the radius of curvature as being this product.

Table 1 Advanced Meshing Parameters

Parameter	Value
Element Growth Rate	1.3
Mesh Curvature Factor	0.3
Mesh Curvature cutoff	0.001

2.6. Numerical Method:

2.6.1 Solution for the concentration and potential fields

A Lagrangian Multiplier based constrained galerkin finite element approach to is used to discretize the governing set of equations along with the boundary conditions. The method used provides a flexible way to solve multiple coupled partial differential equations with Neumann and Dirichlet Boundary conditions simultaneously. To solve our model, we used a generalized finite element code: COMSOL. COMSOL represents all models using a generalized

$$e_a \frac{\partial^2 u}{\partial t^2} + d_a \frac{\partial u}{\partial t} + \nabla \cdot (-c \nabla u - \alpha u + \gamma) + \beta \cdot \nabla u = f \quad (1.51)$$

on the computational domain in 1D, 2D or 3D. To model our equations, we used two sets of equations of the form (1.51). The first set is used to represent the Nerst Planc equations for the three ions of copper, sulphate and hydrogen. The second set is used to represent the Poisson equation. The following table represents the various parameters of equation (1.51) for the Nerst Planc equation:

Table 2 Parameters and their Corresponding value for Nerst-Planc equation

Parameter	Value
e_a	0
u	$\begin{bmatrix} c_{cu} \\ c_{SO_4} \\ c_H \end{bmatrix}$
d_a	$\begin{bmatrix} 1 & 0 & 0 \\ 0 & 1 & 0 \\ 0 & 0 & 1 \end{bmatrix}$
c	$\begin{bmatrix} D_{cu} & 0 & 0 \\ 0 & D_{SO_4} & 0 \\ 0 & 0 & D_H \end{bmatrix}$
a	0
α	$\begin{bmatrix} \begin{bmatrix} 2Fu_{Cu}\Phi_x \\ 2Fu_{Cu}\Phi_x \end{bmatrix} & \begin{bmatrix} 0 \\ 0 \end{bmatrix} & \begin{bmatrix} 0 \\ 0 \end{bmatrix} \\ \begin{bmatrix} 0 \\ 0 \end{bmatrix} & \begin{bmatrix} -2Fu_{SO_4}\Phi_x \\ -2Fu_{SO_4}\Phi_y \end{bmatrix} & \begin{bmatrix} 0 \\ 0 \end{bmatrix} \\ \begin{bmatrix} 0 \\ 0 \end{bmatrix} & \begin{bmatrix} 0 \\ 0 \end{bmatrix} & \begin{bmatrix} Fu_H\Phi_x \\ Fu_H\Phi_y \end{bmatrix} \end{bmatrix}$
β	0
f	0

Further the above set of equations are solved only for the regions of the membrane and electrolyte, but not for the mask. It is assumed that the mask is impermeable to the electrolyte and hence the concentration of either of the ions is uniformly zero.

Table 3 Parameters and their corresponding value for Poisson's Equation

Parameter	Value
e_a	0
u	Φ
d_a	0
c	$\frac{\epsilon_0 \epsilon_w}{F}$
a	0
α	0
β	0
f	$z_{Cu}c_{Cu} + z_{SO_4}c_{SO_4} + z_Hc_H$ for Nafion and elect 0 for dielectric mask.

Using this scheme, the finite element discretization of the time-dependent PDE problem can be written as

$$0 = L(U, \dot{U}, \ddot{U}, t) - N_F(U, t)\Lambda \quad (1.52)$$

$$0 = M(U, t) \quad (1.53)$$

where equation (2.44) represents the discretized governing equations and (2.45) represents the constraints due to the boundary conditions. The time dependent problem is solved using SUNDIALS (Suite of Nonlinear and Differential/Algebraic equation Solvers) [68-69] developed at Lawrence Livermore Laboratories. This method uses a highly stable variable-order-variable-step-size backward differentiation formula (BDF). For each individual time step convergence criterion was met when:

$$\left(\frac{1}{N} \sum_i \left(\frac{|E_i|}{A_i + R|U_i|} \right)^2 \right)^{(1/2)} < 1 \quad (1.54)$$

Where A_i is the absolute tolerance for the i th degree of freedom, R is the relative tolerance, N is the number of degrees of freedom, E_i is the estimate of the error in the solution for the time step under consideration and U_i is the solution for the i -th degree of freedom. In our simulations a absolute tolerance of .001 and a relative tolerance of .01 was used for all the degrees of freedom.

2.6.2 Solution of the shape of the copper anode

Due to anodic dissolution, the shape of the node changes as a function of time. Hence in order to accurately predict the shape of the anodic surface, the current density etc, it is necessary to keep track of the exact position of all points of the anodic surface. Further, when the boundary deforms, it is necessary to move or fill up the region created by the movement of the surrounding boundary. This is where different methods such as Lagrangian, Eulerian or Arbitrary Lagrangian-Eulerian come into practice. These methods provide ways to accurately move/deform the mesh so as to fill up the gaps and thus maintain continuity.

Lagrangian methods are primarily used in structural or solid mechanics. In this method, each individual node of the computational mesh follows the associated material particle during motion. The lagrangian method allows an easy tracking of free surfaces and interfaces between different materials. The material coordinates, X , allow us to identify the reference configuration, R_X . The motion of the material points relates the material coordinates, X , to the spatial ones x . We can thus define

$$x = x(X, t) \quad (1.55)$$

Eulerian algorithms on the other hand are widely used in fluid mechanics. Here, the computational mesh is fixed and the continuum moves with respect to the grid. In Eulerian description, large distortions in the continuum motion can be handled with relative ease, but generally at the expense of precise interface definition and resolution of flow details. The conservation equations are formulated in terms of

the spatial coordinates x and the time t . Therefore, the Eulerian description of motion only involves variables and functions having an instantaneous significance in fixed region of space. The material velocity v at a given mesh node corresponds to the velocity of the material point coincident at the considered time t with the considered node. The velocity v is consequently expressed with respect to the fixed-element mesh without any reference to the initial configuration of the continuum and the material coordinates $X : v = v(x, t)$.

Because of the shortcomings of purely Lagrangian and purely Eulerian descriptions, a technique has been developed that succeeds to a certain extent, in combining the best features of both the lagrangian and the Eulerian approaches. Such a technique is known as the arbitrary Lagrangian-Eulerian description. In the ALE description, the nodes of the computational mesh may be moved with the continuum in normal Lagrangian fashion, or be held fixed in Eulerian manner, or be moved in some arbitrarily specified way. Hence ALE proves ways to accurately handle greater distortions of the continuum than can be handled by a pure Lagrangian or pure Eulerian method.

In the ALE description of motion, neither the material configuration R_x nor the spatial configuration R_χ is taken as the reference. Thus, a third domain is needed: the referential configuration R_χ where reference coordinates χ are introduced to identify the grid points. The referential domain R_χ is mapped into the material and spatial domains by Ψ and Φ respectively. The particle motion ϕ may then be expressed as: $\phi = \Phi \cdot \Psi^{-1}$.

In order to express the conservation laws for mass, momentum and energy in an ALE framework, a relation between material time derivative, which is inherent in conservation laws, and referential time derivative is needed. To relate the time derivative in the material, spatial and referential domains, we define three scalar quantities $f(x, t)$, $f^*(\chi, t)$ and $f^{**}(X, t)$ in the spatial, referential and material

domains, where the stars indicate that the functional forms are different for spatial, material and referential domain in general.

Since the particle motion ϕ is a mapping, the spatial description $f(x,t)$, and the material description $f^{**}(X,t)$ of the physical quantity can be related as:

$$f^{**} = f(\phi(X,t),t) \text{ or } f^{**} = f \cdot \phi \quad (1.56)$$

The gradient of this expression can be easily computed as:

$$\frac{\partial f^{**}}{\partial(X,t)}(X,t) = \frac{\partial f}{\partial(x,t)}(x,t) \frac{\partial \phi}{\partial(X,t)}(X,t) \quad (1.57)$$

Which is amenable to the matrix form

$$\begin{pmatrix} \frac{\partial f^{**}}{\partial X} & \frac{\partial f^{**}}{\partial t} \end{pmatrix} = \begin{pmatrix} \frac{\partial f}{\partial x} & \frac{\partial f}{\partial t} \end{pmatrix} \begin{pmatrix} \frac{\partial x}{\partial X} & v \\ 0^T & 1 \end{pmatrix} \quad (1.58)$$

Which renders after multiplication:

$$\frac{\partial f^{**}}{\partial t} = \frac{\partial f}{\partial t} + \frac{\partial f}{\partial x} \cdot v \quad (1.59)$$

$$\frac{\partial f^{**}}{\partial X} = \frac{\partial f}{\partial x} \frac{\partial x}{\partial X} \quad (1.60)$$

2.6.3 Mesh Update and Smoothing

When the surrounding boundary deforms as a results of etching, it becomes necessary to move the mesh as well. However just moving the mesh nodes on the boundary, with the same velocity as that of the boundary surface, would results in negative volumes of the mesh and hence render the mesh unusable. It is for this reason that we use mesh smoothing. Using this method, the position of the mesh points are modified, but the mesh topology remains unchanged. Shifting points can have a drastic effect on the quality of the mesh, and it is more efficient that refinement and collapsing points especially when the translation amplitudes are small. A global optimum is reached by sequentially updating the mesh points in a Gauss Seidal type iteration. As long as the mesh smoothing is done, after each time

step, only a few sweeps through the mesh is sufficient to have a good quality mesh. A simple and straight forward method to smooth a mesh, known as Laplace smoothing is used here. A mesh point is moved to the centroid of the surrounding mesh points which are topologically connected. Since only the region underneath the membrane deformed, the implementation of the moving mesh was carried out only in that region. This reduced the number of variables solved for and hence the computational time.

CHAPTER 3 SIMULATION AND RESULTS

3.1. Experimental results

The purpose of this thesis is present a model for the key phenomena governing the process of FEFIIT. Hence we first present key experimental results obtained earlier by Khiam et al. In his work Khiam et al, carried out experiment on FEFIIT using three different operating modes of FEFIIT and observed the material removal rate and the surface structures under various operating parameters.

3.1.1 Method 1: Direct Contact Mask-Modulated Electric Field Printing

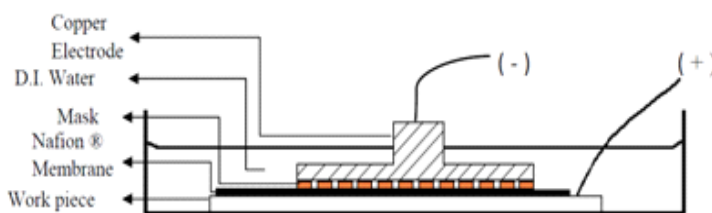


Figure 3.1: Experimental Configuration for direct contact printing method

This method is characterized by the fact that the Nafion membrane is in direct-contact with the copper substrate/workpiece and the mask. The cathode or the negatively charged electrode is placed on top of the perforated mask. A copper stud is attached directly on top of the mask, and acts as an electrode. A second purpose of the copper stud is to apply a uniform pressure on the mask to prevent it from floating freely in the D.I. water. The entire assembly is immersed in DI water or electrolyte to close the conduction current path. It is assumed that the applied potential is adequately large that the kinetics of the electrode are not rate limiting. The current obtained when the conductive mask makes contact with the Nafion® membrane will depend on the rate of mass transport of metal ions transfer to the bottom of the mask. The result is a reduction process at the mask and membrane interface (deposition) and an oxidation process at the work piece (etching).

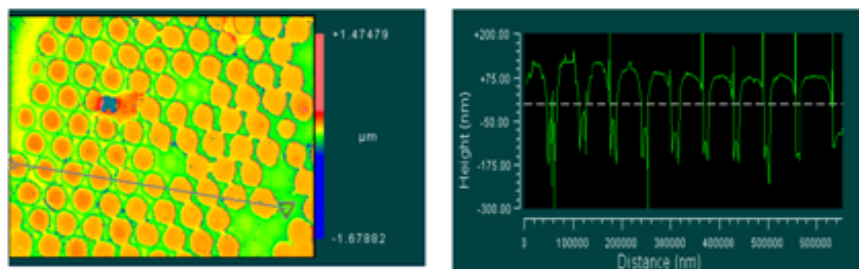


Figure 3.2 Direct contact printing under CDC voltage (5V, pulse duration = 0.02/200 μ sec., exposure = 10sec.

Experiments were conducted under voltage control, such that the total current was within the power supply sensitivity. The applied voltage was varied between 2-5 volts and the effect of this variation on the height, width and the slope of the wall were obtained. During the course of the experiments, it was found that material was removed only after the voltage difference between the cathode and the anode reached a certain threshold. This was attributed to the fact that there exists a certain thickness of electric double layer, which has to be broken down before material can be removed from the surface of the workpiece. In general it was observed that the material removal rate in terms of the height, width and slope of the surface increased with increasing applied voltage.

3.1.2 Method 2: Non-contact Mask-Modulated Electric Field Printing

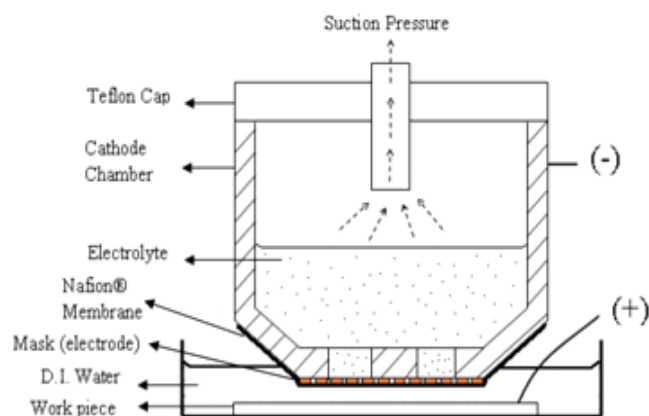


Figure 3.3: Schematic diagram for non-contact mask-modulated electric field printing.

The present method, used two separate chambers to provide greater control in obtaining structures on the surface of the copper disc. The upper chamber consists of a copper tubular structure containing the electrolyte. The electrolyte used here, is a mixture of various proportions of copper sulphate, hydrogen sulphate, and water. The chamber is connected to a vacuum pump, to induce a negative pressure within itself. The perforated mask is directly attached on to its surface along with the membrane using a tape. The lower chamber consists of the copper disc (workpiece) immersed in DI water. To operate the system, the upper chamber is brought in contact with the DI water present in the lower chamber, so that a continuous current flow path is established.

By varying the pressure applied inside the cathode chamber relative to ambient pressure, local curvature on the membrane can be achieved. The local curvature of the membrane will modulate the equipotential electric field to focus the electric current on the work piece and a pattern with aspect ratio smaller than the original window mask size can be achieved. Besides pressure variation, the depth and aspect ratio on the pattern are controlled by process parameters such as separation distance between two terminal, amount of potential energy that applied (voltage),

total exposure time as well as concentration of the electrolyte used. A well defined mask (electrode) with precise window opening is mandatory to achieved pattern in micron range.

Three different mask types were used in these experiments: a) a 50 PPI wire mesh, b) a perforated stainless steel mask consisting of triangular holes of diameter 570 μm and pitch of 1170 μm , and c) a polymer mask with a 2.2 mm diameter hole. Experiments were carried out under current control in chopped DC and DC modes. Chopped DC yielded very interesting patterns on the surface of the work-piece, yielding a torus-shaped structure instead of a hemispherical structure.

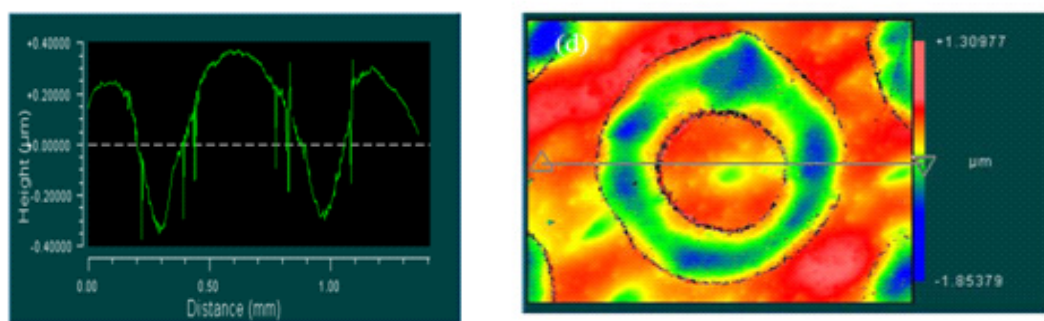


Figure 3.4 $I = 0.2\text{A}$. (CDC voltage, standoff distance = $75\mu\text{m}$, pressure = 15inHg, pulse duration = 6.25/400msec., exposure = 60sec., electrolyte = 1.80M H_2SO_4 + 0.25M CuSO_4)

An increase in the applied pressure also yielded an improvement in the feature size and shape. While at lower pressure differences under chopped DC, a flat shaped bowl was obtained, at higher negative pressures, a torus shaped structure was obtained.

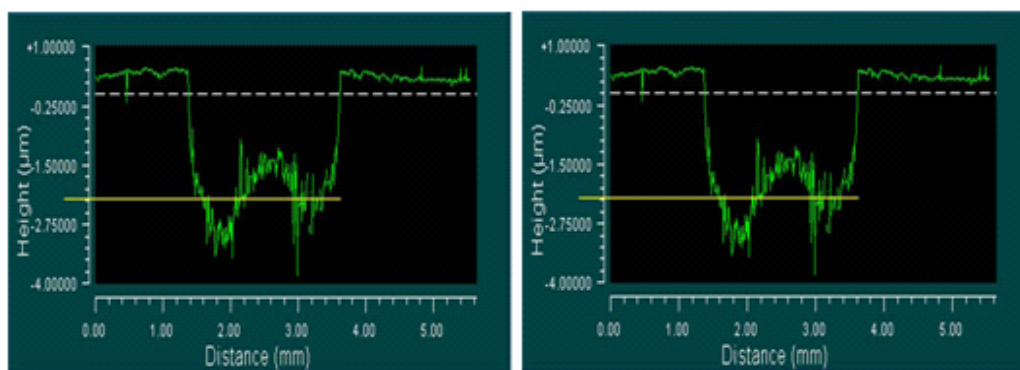


Figure 3.5: Polymer sheet with single drilled 2mm hole, comparison of pressure variation at 1.25X. (a) $P = 0$ inHg (b) $P = 4$ inHg (CDC voltage, standoff distance = $10\mu\text{m}$, current = 0.05A , pulse duration = $0.5/50\text{msec.}$, exposure = 15sec. , electrolyte = $1.80\text{M H}_2\text{SO}_4 + 0.25\text{M CuSO}_4$)

The role of standoff distance between the upper chamber and the lower chamber was also studied. Experiments showed that an increase in the stand-off distance resulted in a decrease in MRR.

3.1.3 Method 3: Non-contact Uniform Electric Field Mask Printing

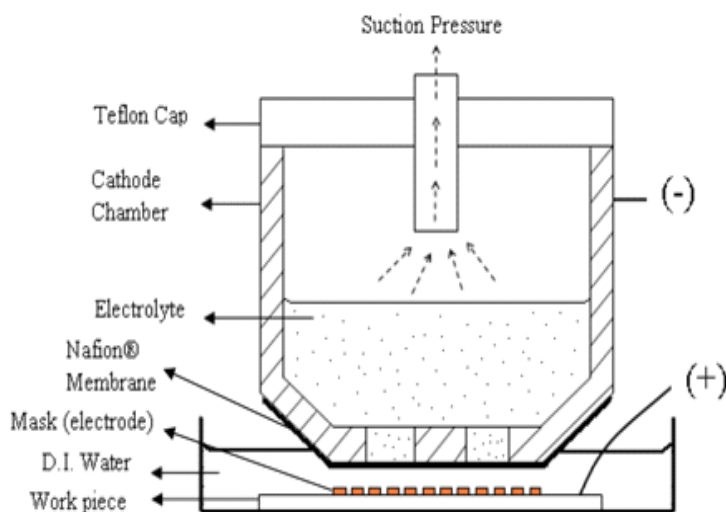


Figure 3.6 Schematic diagram depicting Uniform Electric Field Mask Printing

This experimental setup is similar to the one used earlier. However, this method is distinguished by the fact, that the mask lies directly on top of the copper workpiece. The Nafion membrane is attached directly on the surface of the top chamber. Experiments were conducted using a 35 μm TEM mesh using this setup.

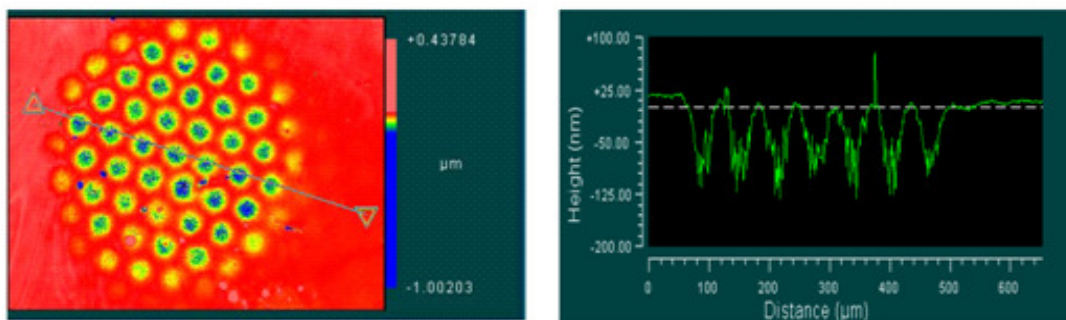


Figure 3.7: Mask printing under uniform DC voltage (0.1V, standoff distance = 20 μm , P=1.0inHg, exposure = 30sec., electrolyte = 0.01M H_2SO_4 + 0.5M CuSO_4).

3.2. Simulation details

Parameter	Value
D_{Cu}	$6.1e-10 m^2 / s$
D_{SO_4}	$1.065e-9 m^2 / s$
D_H	$9.3e-9 m^2 / s$
$D_{Cu,membrane}$	$8.86e-11 m^2 / s$
$D_{SO_4,membrane}$	$3.37e-11 m^2 / s$
$D_{H,membrane}$	$4e-10 m^2 / s$
$V_{cathode}$	-1V
V_{anode}	+1V
i_0	$9.7 A / m^2$
α_a	0.5
α_c	0.21
γ	0.75
MW_{Cu}	$63.5e-3 kg / mole$
ρ_{Cu}	$8920 kg / m^3$
C_{CuSO_4}	$500 M / m^3$
$C_{H_2SO_4}$	$100 M / m^3$
ϵ	$8.854e-12 F / m$
$\epsilon_{electrolyte}$	80
ϵ_{Nafion}	6
Simulation duration(t_{total})	0.1 seconds
cell half – width(L)	$2.5e-3 m$
cell height(H)	$1e-3 m$
membrane thickness(T_{mem})	$12.5e-6 m$
mask thickness(T_{mask})	$25e-6 m$
gap height(T_{gap})	$10e-6 m$
opening radius(W)	$50e-6 m$

To simulate the model, an initialization simulation was carried out with a time scale of $1e-3$ seconds. This was necessary, since an accurate initial value of the potential distribution couldn't be provided. In the experimental situation, the initial potential will be uniformly zero, however it will rapidly rise to a stable potential distribution. Hence a small time step is necessary to capture this sudden rise. If a large time step is used here, the simulation doesn't converge, since this sudden rise cannot be captured properly. However after this sudden rise, the time scale of simulation becomes higher, and it is no longer necessary to use a small time step to capture the phenomena, unless a varying potential is applied at the anode or cathode. Hence we use a larger time step of $1e-2$ seconds after this sudden jump.

3.3. Variation with height from electrode surface

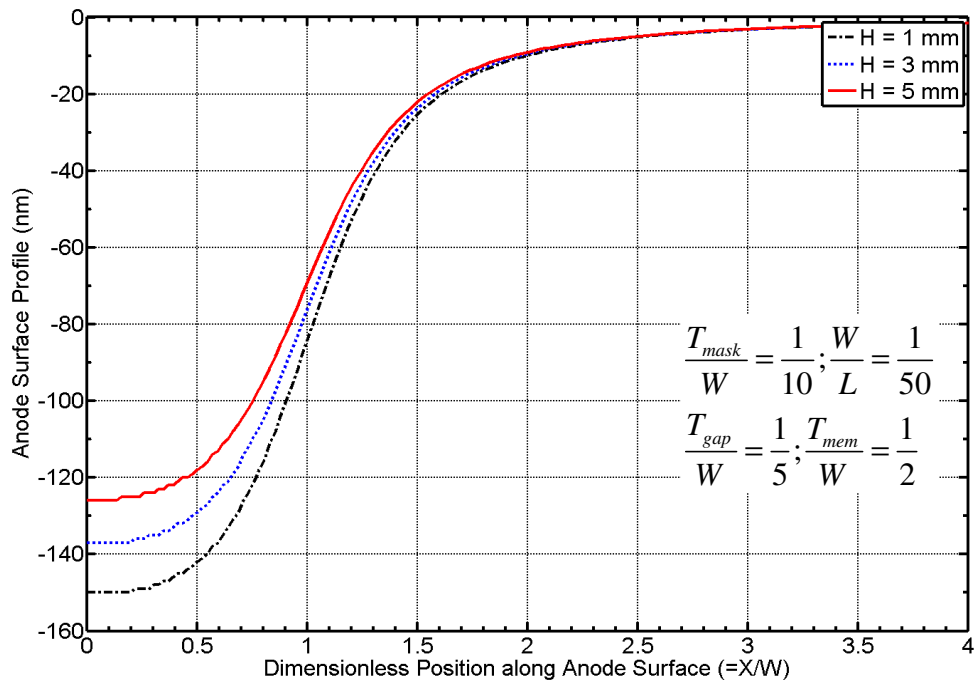


Figure 3.8 Variation of imprinted profile with various values of standoff distance between anode and cathode

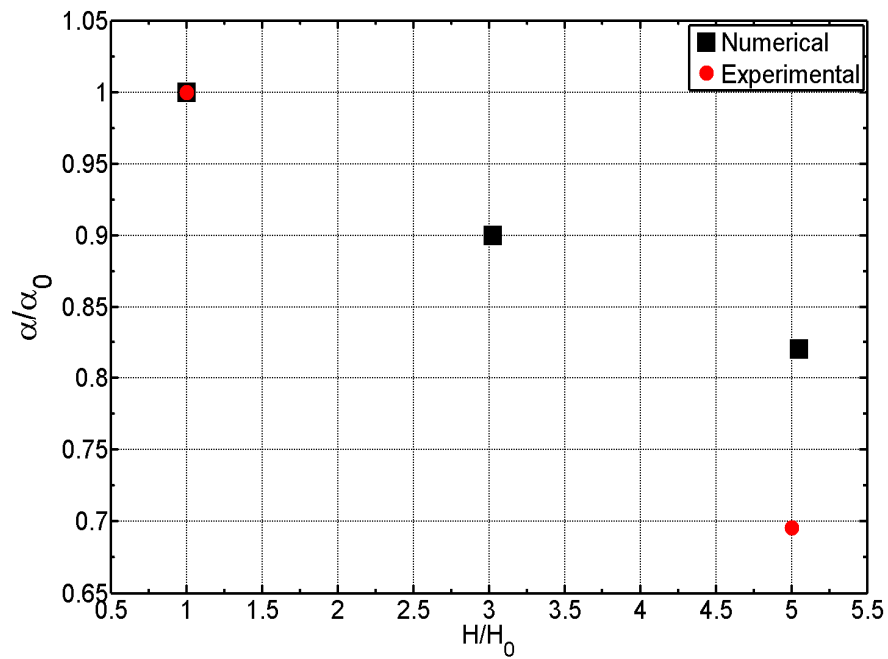


Figure 3.9 Variation of α (surface angle) with standoff distance between anode and cathode (H), comparison of experimental and numerical values

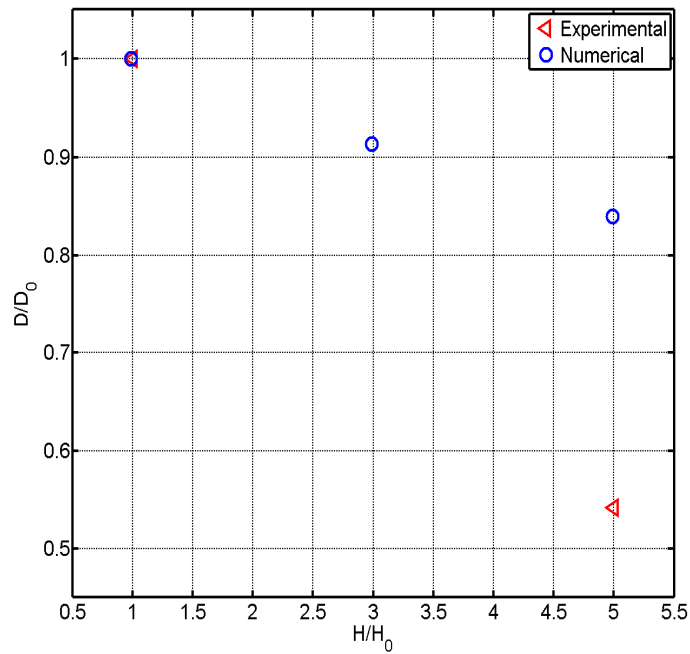


Figure 3.10 Variation of depth of surface profile (D) with standoff distance between anode and cathode (H), comparison of experimental and numerical values

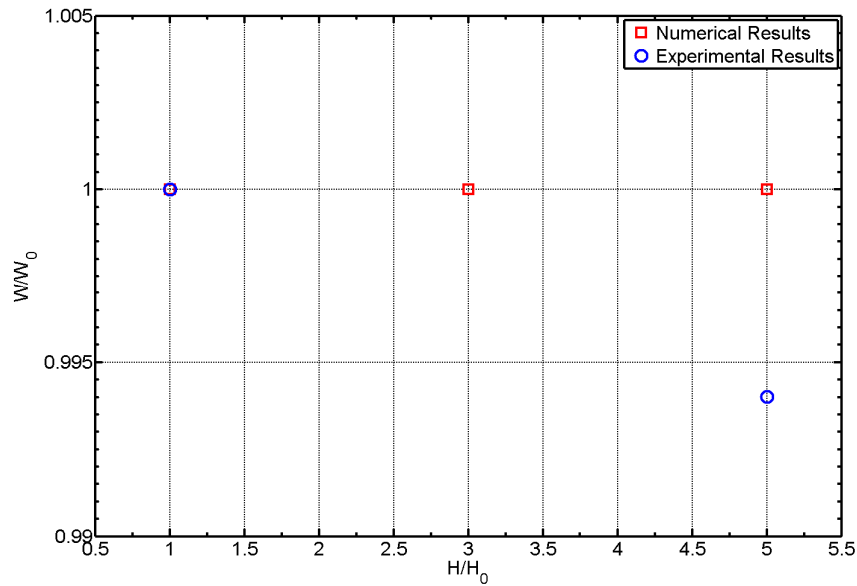


Figure 3.11 Variation of width of surface profile(W) with standoff distance between anode and cathode(H), comparison of experimental and numerical values

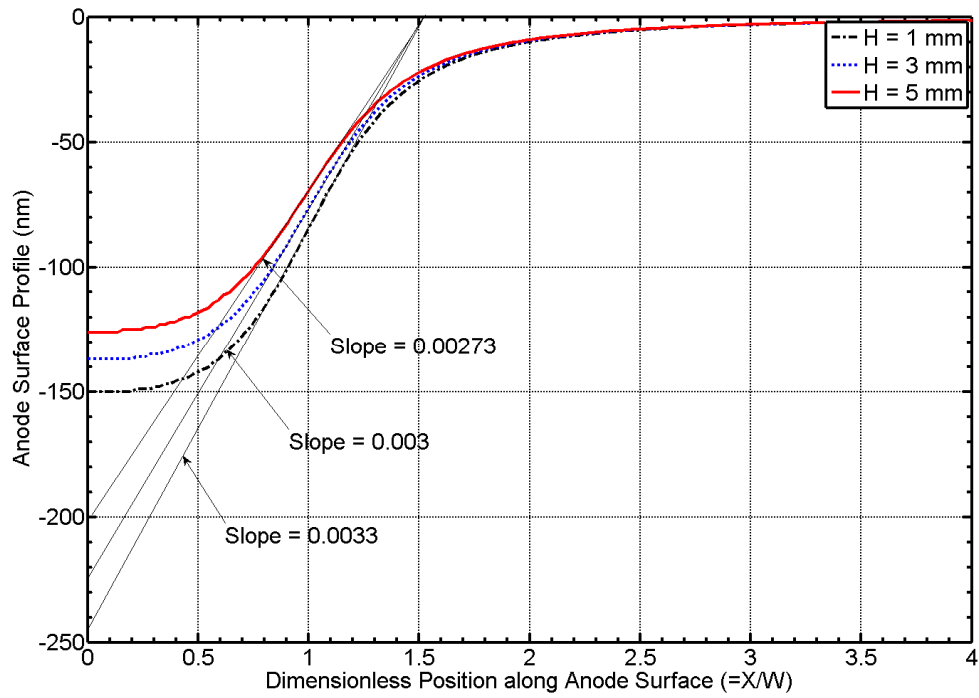


Figure 3.12 Schematic depicting the imprinted profile along with the fitting line used to calculate surface angle(α)

In Figure 3.8 we plot the variation of the anode surface profile with the dimensionless position along the original anode surface. For greater separation between the anode and the cathode, at constant potential difference between the two electrodes, the electric field at the electrodes and within the chamber decreases. A decrease in the electric field in the sub-domain leads to a decrease in the flow of ions from the anode to the cathode. This results in a decrease in the net current that can be sustained. Hence, the surface overpotential, responsible for the dissolution of the copper ions decreases, thus giving rise to a decrease in the net dissolution at points along the surface of the anode. Since the dissolution rate is directly proportional to the electric field, we find a decrease in the net dissolution rate. Thus the Anode surface has a higher depth of cut with decreasing electrode height.

Figure 3.9 to Figure 3.11 plots a comparison of the experimental and theoretical results obtained using mask modulated electric field printing. In the course of the simulations, we couldn't reach the experimental time scales. Further, a number of characterizing parameters such as the anodic and cathodic current coefficients of the electrodes are extrapolated from literature results and might deviate from the experimental conditions in Khiam's results. This is because the studies in the literature measured/obtained the parameters during electro-deposition rather than electro-dissolution. Hence direct quantitative comparisons between experimental and numerical results are difficult to make. However, we can compare the dimensionless values and compare the trends observed. As seen from the above figures, the trends obtained by comparing the numerical and experimental results seem to be correct, and are very close. Particularly the width of the imprinted profile has a very good match with the experimental results. Finally Figure 3.12 shows a schematic depicting how the height, width and angle of the imprinted surface was obtained from the simulation results.

3.4. Variation with chamber width/periodicity of mask opening

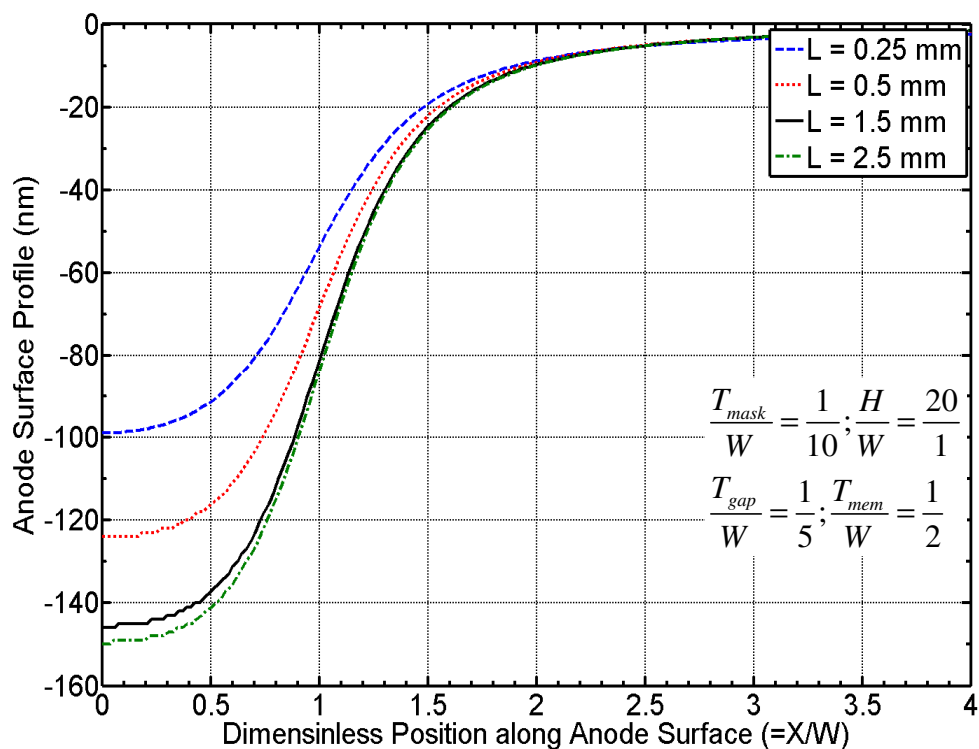


Figure 3.13 Variation of imprinted profile with various values of half-pitch of cell

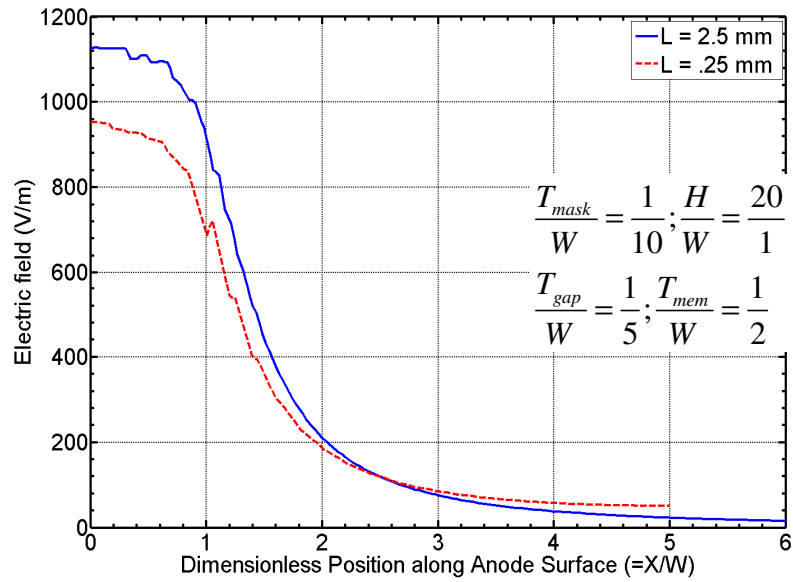


Figure 3.14 Variation of Electric field on anode surface with half cell width

Figure 3.13 depicts the variation of the anode surface profile with width of the chamber. At larger widths we obtain a greater depth of cut and greater dissolution, compared to that at smaller chamber widths. In these simulations, all other parameters except from the width of the channel have been kept fixed. The greater dissolution of the anode surface at higher chamber widths comes across due to higher electric fields present just below the opening when a larger chamber width is used. The increase in electric field arises due to a larger area of exposed cathode surface at higher chamber widths. Since the mask has a lower dielectric constant, it presents a higher resistance path, hence the electric lines of force originating out of the cathode tend to bend away from the mask and towards the opening of the mask. The opening in the mask presents a path of least resistance; hence most electric lines of force originating out the cathode tend to pass through the opening. Obviously for a larger exposed electrode, larger number of electric lines of force will originate from the cathode, and will get focused near the mask. Since, the electric field is directly proportional to the density of electric lines of force passing through a cross-sectional area, the region underneath the mask opening, for the case with higher chamber width, experiences a higher electric field. This leads to a higher surface over potential and hence a higher dissolution rate.

However, as the chamber width increases, the electric line of force originating from the edge has to traverse a longer distance to move to the mask opening. Hence the net resistance of the path traversed by the electric line of force originating from the chamber edge and moving through the mask opening becomes increasingly large. Hence at large cell widths, the path going directly through the mask, becomes a path of less resistance compared to a path originating from the ends of the chamber and through the mask opening. Since the lines of force tend to take the path of least resistance, we find more lines of force moving directly through the mask and towards the anode. Hence, the increase in electric field and the net removal rate becomes saturated at high values of mask width.

A second interesting to notice from Figure 3.13 and Figure 3.14 is the fact that the surface profile for shorter width undergoes a constant shift along the vertical direction. However beyond a certain critical value of the widths, there is no shift in the surface profile. This shift originates from cross-leaks between two adjoining cells. Since the widths of masks relative to the mask opening is small, sufficient number of electric lines of force can penetrate to the edge of the cells, thus eroding material at the edges as well. When the mask width compared to the mask opening is relatively large, it is much more difficult for the electric lines of force to reach the edges, thus causing minimal erosion at the edges of the mask. Increase in the width of the chamber beyond a certain critical value of approximately 2.5 mm doesn't result in an increase in the etching of the anode. This arises primarily because the electric field strength becomes saturated at a critical chamber width.

3.5. Variation with opening radius

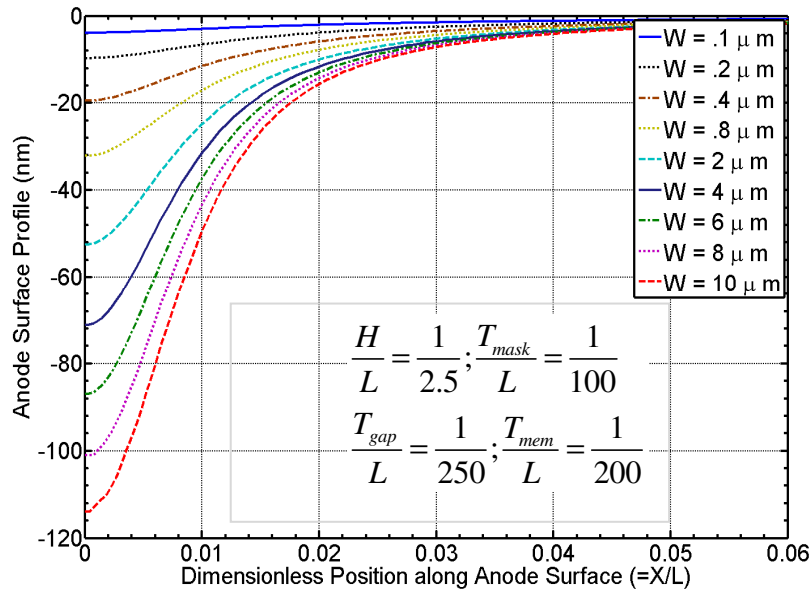


Figure 3.15 Variation of imprinted profile with opening radius. Variation shown for small opening radius 100 nm-1 μ m

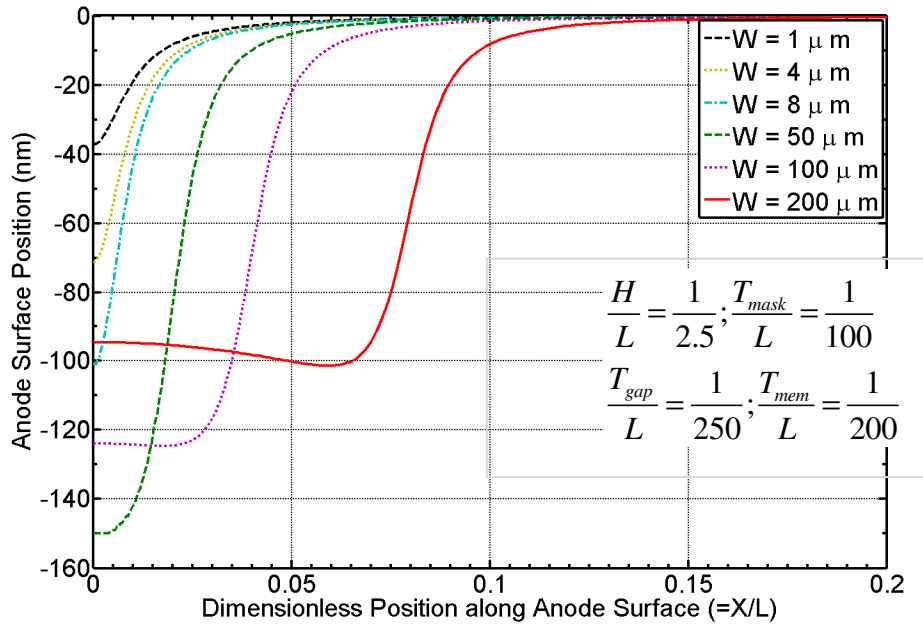


Figure 3.16 Variation of imprinted profile with opening radius, at intermediate values ($1\mu m - 200\mu m$), showing the increase and subsequent decrease in depth of cut.

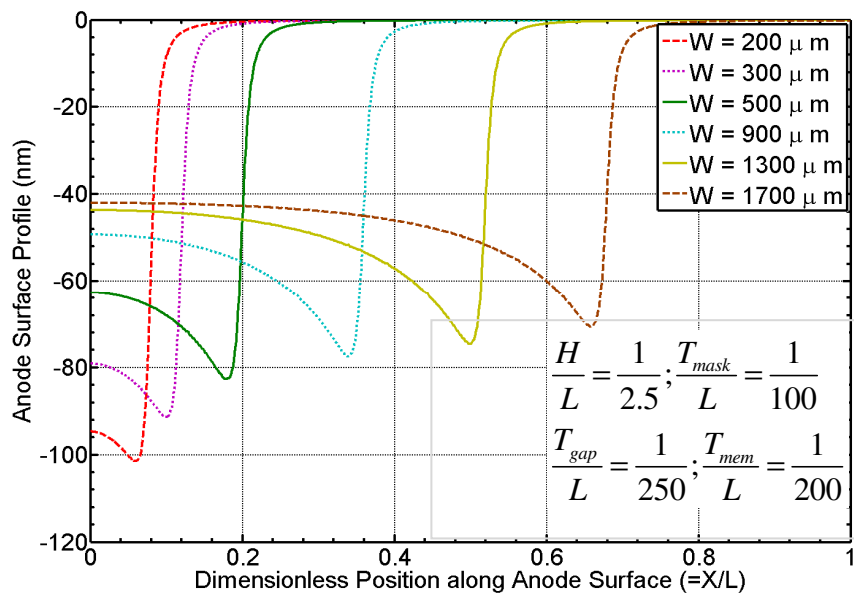


Figure 3.17 Variation of imprinted profile with opening radius at large value of the radius ($200\mu m - 1700\mu m$)

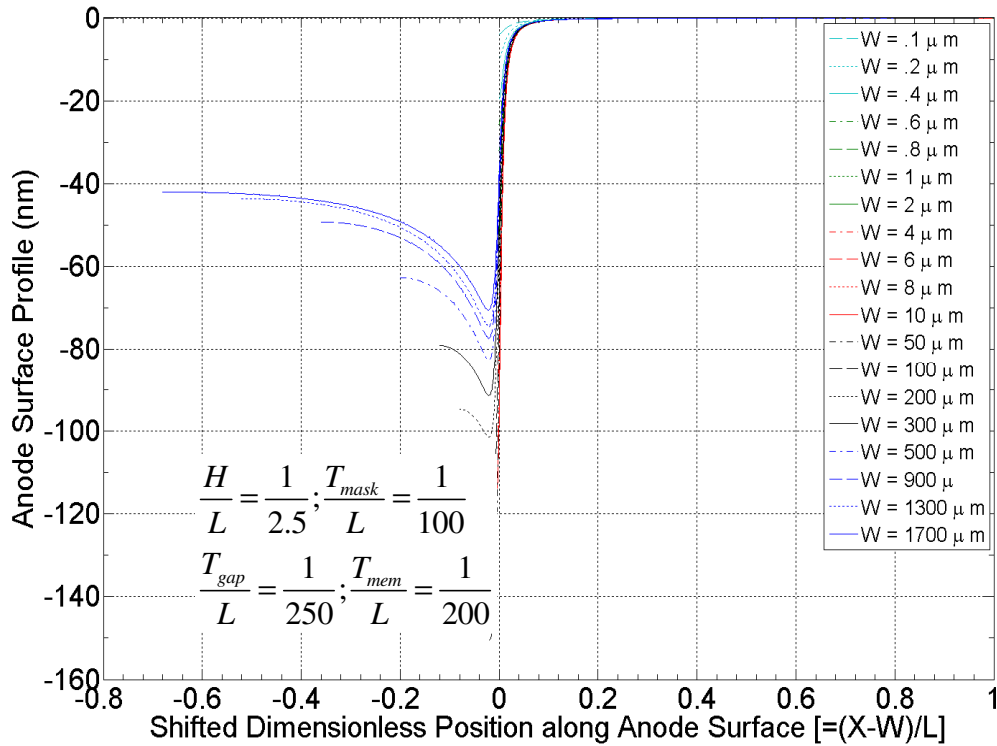


Figure 3.18 Variation of imprinted profile shifted by the opening radius W

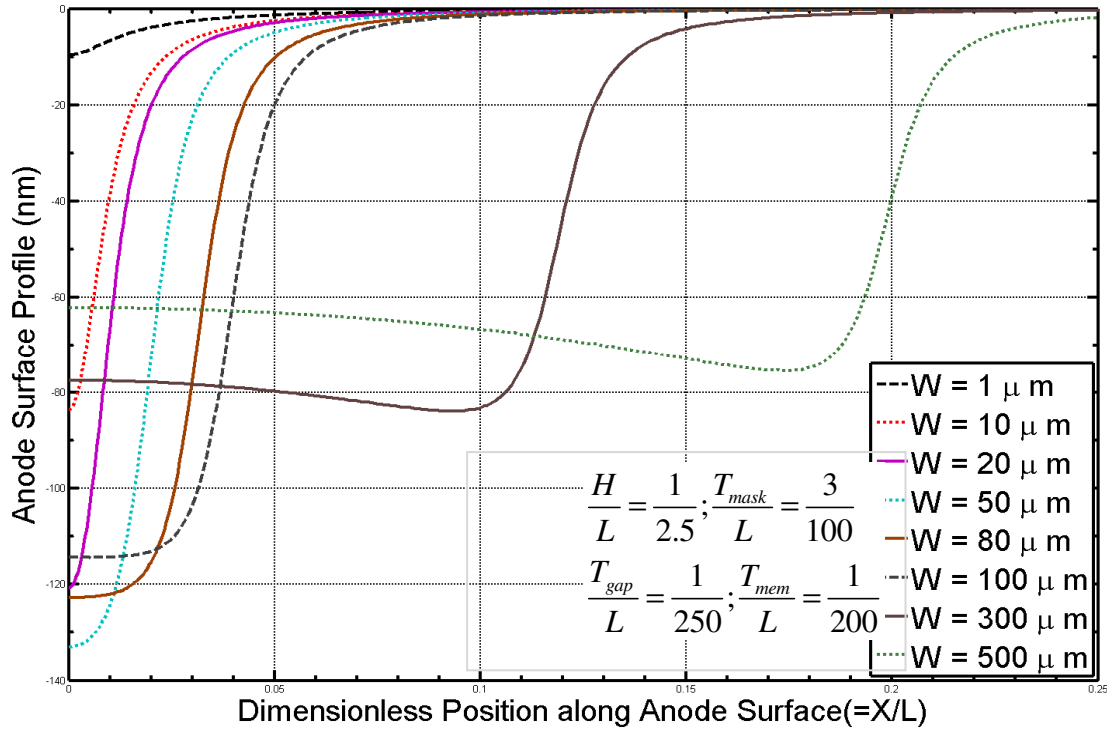


Figure 3.19 Variation of imprinted profile with various opening radius, mask thickness (T_{mask}) = 75e-6 m

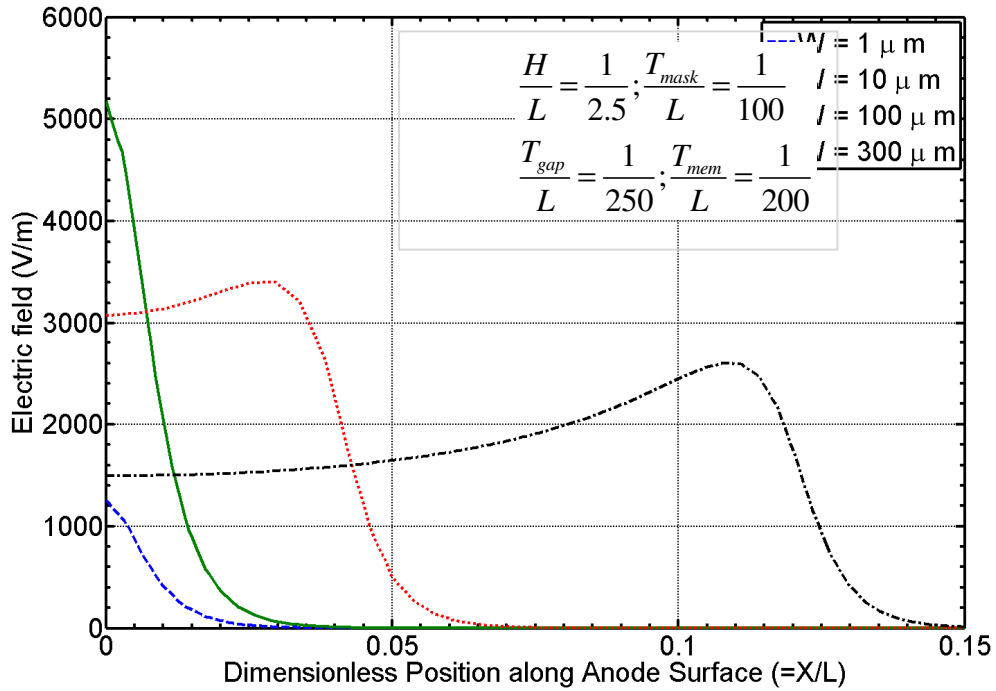


Figure 3.20 Variation of Electric field with Opening radius, using conductive media model

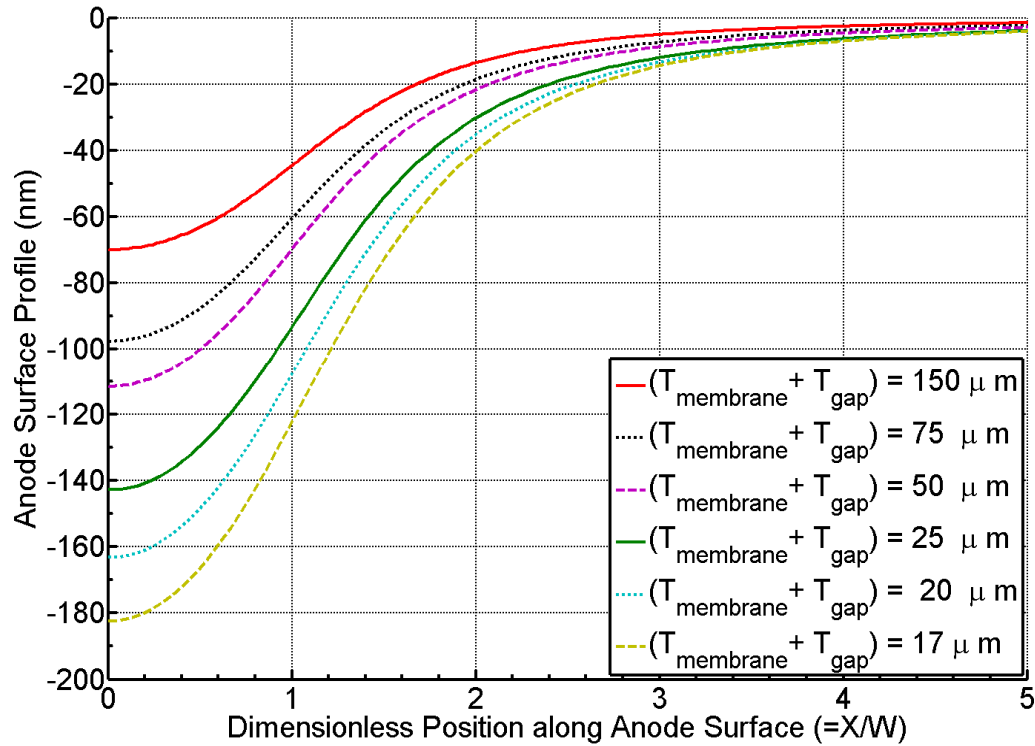


Figure 3.21 Variation of the imprinted profile with standoff distance between mask and anode ($=T_{\text{gap}} + T_{\text{membrane}}$), for $W / (T_{\text{gap}} + T_{\text{mask}}) = 1$

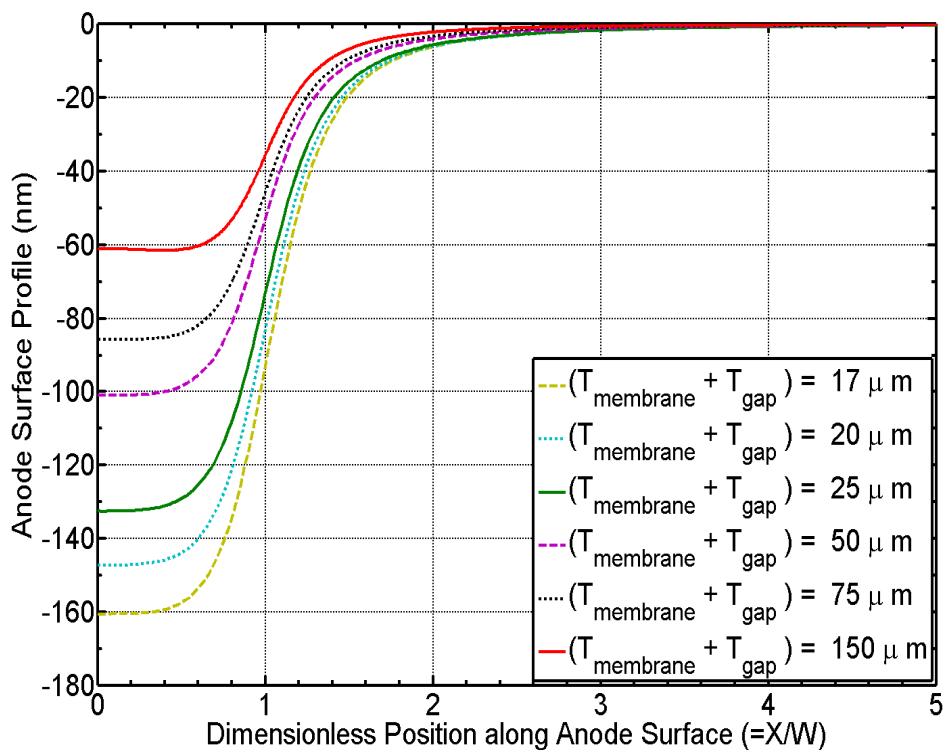


Figure 3.22 Variation of the imprinted profile with standoff distance between mask and anode ($=T_{\text{gap}} + T_{\text{membrane}}$), for $W / (T_{\text{gap}} + T_{\text{mask}}) = 3$

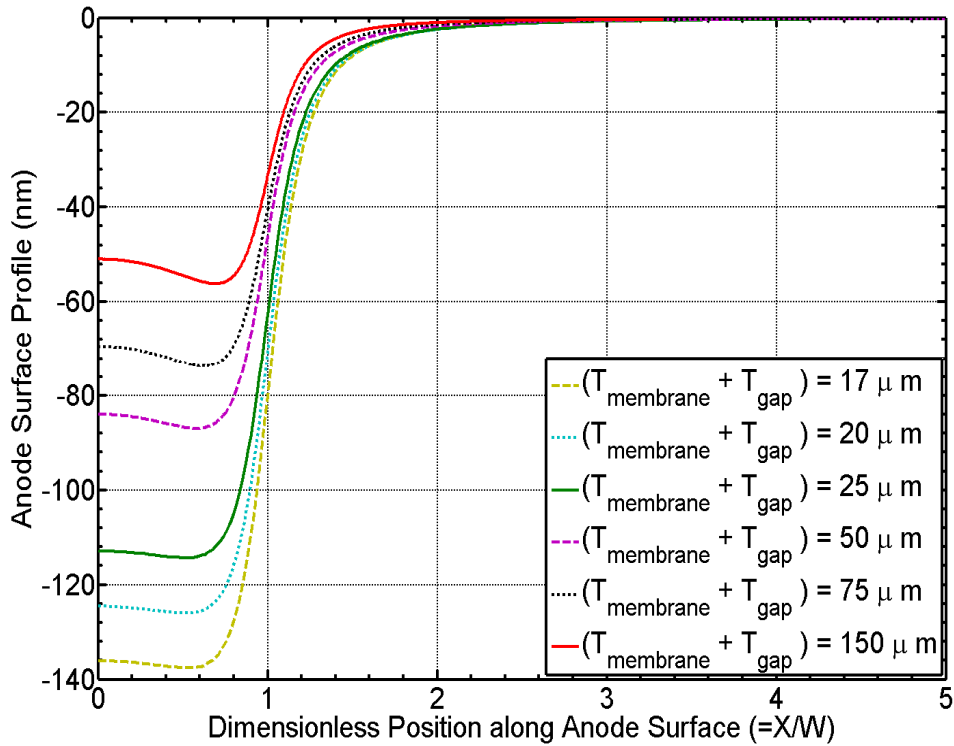


Figure 3.23 Variation of the imprinted profile with standoff distance between mask and anode ($=T_{gap} + T_{membrane}$), for $W / (T_{gap} + T_{mask}) = 5$

Figure 3.15, Figure 3.16, and Figure 3.17 illustrate the variation of the imprinted surface with change in the opening radius W , while keeping all other parameters fixed. These figures illustrate the variation in the imprinted profile for various ranges of the opening radius, to illustrate the trends clearly. It can be seen that at small values of W , the imprinted profile tends to grow linearly monotonically with increase in the opening. However, with increase in W , a critical value is reached beyond which no increase in the absolute value of the imprinted profile at the center is obtainable. At that point, the central portion of the opening tends to flatten out. With further increase in W , a sharp asperity shaped structure is produced, which is located just beneath the edge of the mask, but slightly away from it. Further as opening is made wider, the entire imprinted surface tends to get decreased in height and broader is width.

It was found upon further inspection, that the imprinted surface is directly proportional to the electric field produced at the surface of the anode. This leads to the conclusion that while other phenomena might be occurring, it is the electric field the drives and significantly affects the imprinting of the surface. As a result, if we are able to understand the physics occurring in a simple ionic conduction driven model, we should be able to directly correlate the results obtained by the results obtained using the more sophisticated model.

To understand and characterize the above results, we plot Figure 3.21, Figure 3.22 and Figure 3.23. Here we keep the ratio $W / (T_{gap} + T_{membrane})$ fixed, while varying the value of $T_{gap} + T_{membrane}$. It can be seen that the imprinted profile plotted with respect to the non-dimensionalized position along the anode surface appears to be self similar. However, it should be remembered that since there are multiple length scales, no one particular non-dimensionalized number can completely determine the profile shape and size. Rather, some of these numerous dimensionless numbers significantly affect the profile shape. This can be clearly observed at higher values of $W / (T_{gap} + T_{membrane})$. As shown later, in Figure 3.26 and Figure 3.27, the ratio W / T_{mask}

plays a role in determining the sharpness of the feature obtained. Since, the mask thickness T_{mask} remains constant, at higher values of $W/(T_{gap} + T_{membrane})$, the value of W/T_{mask} , becomes very large. This results in a decrease in the sharpness of the indentation obtained on the surface. From these figures it can be observed that, the plateau shaped profile can be obtained only beyond a critical value of $W/(T_{gap} + T_{membrane})$ of approximately 2.

While other parameters, such as the periodicity, the height of the channel can and do influence the imprinted profile, at the values of the opening, radius, the standoff distance between the membrane and the mask, it appears that they don't significantly affect the imprinted surface. A demonstration about the importance of the above two parameters can be observed in Figure 3.13. Intuitively we would have expected to see a plateau shaped structure if we had the same value of W/L , however we don't find the indentation or the plateau shaped profile. This is because, the value of $W/(T_{gap} + T_{membrane})$ in these simulations, is just around 2. If the simulations were done at higher values of $W/(T_{gap} + T_{membrane})$, we would have observed the indentation as well as the plateau shaped structure.

3.6. Variation with standoff distance between mask and anode surface

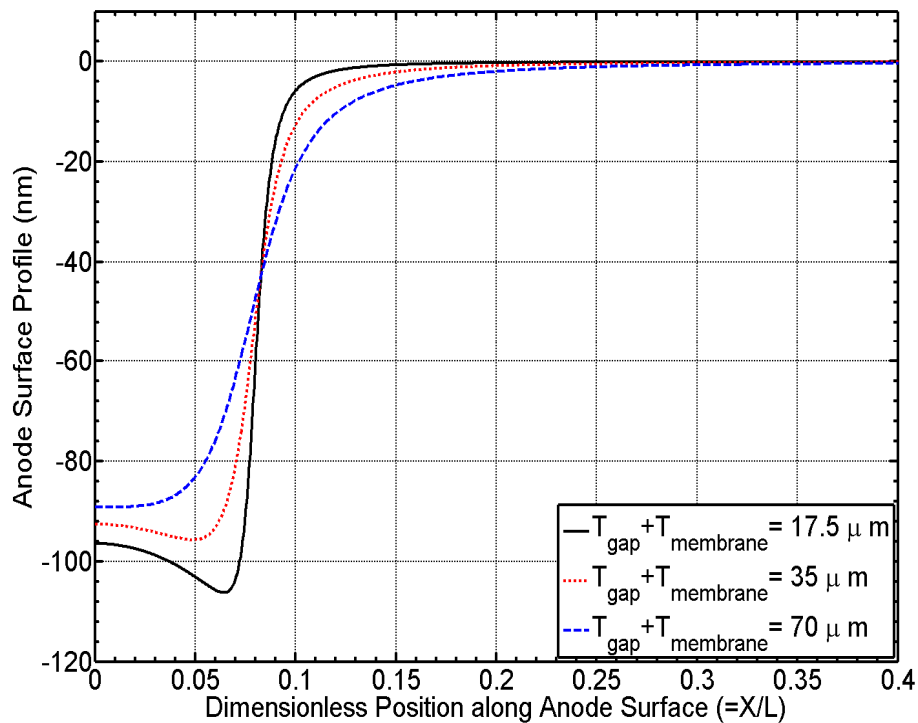


Figure 3.24 Variation of imprinted profile with change in the standoff distance between mask and anode.

The above figure plots the imprinted profile with variation in the standoff distance between the mask and the anode, while all other parameters remain fixed. It can be clearly seen that the effect of the mask edge becomes increasingly important, and the edge shaped feature becomes increasingly sharp. As we reduce the standoff distance, $W / (T_{membrane} + T_{gap})$ and $T_{mask} / (T_{membrane} + T_{gap})$ become increasingly large. As a result we get imprinted profiles, with increasingly sharper indentations.

3.7. Variation with membrane and mask thickness

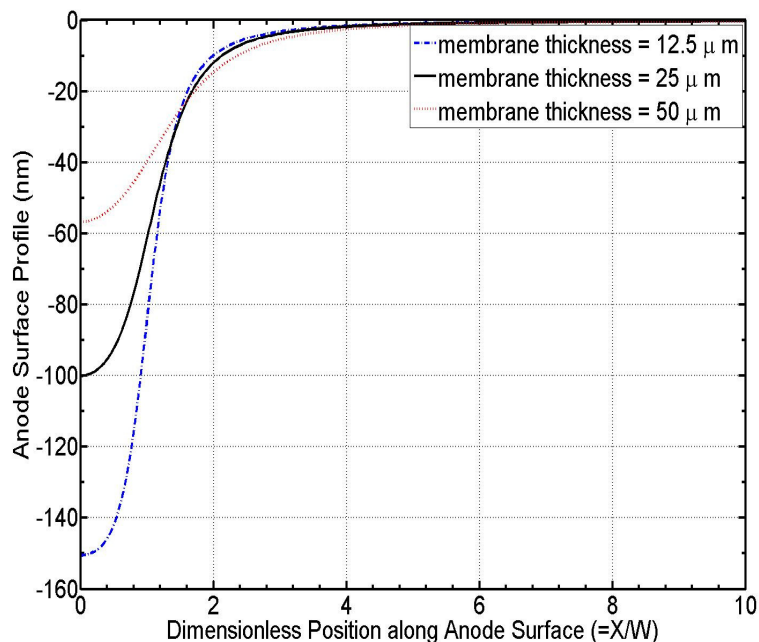


Figure 3.25 Variation of imprinted profile with various values of membrane thickness

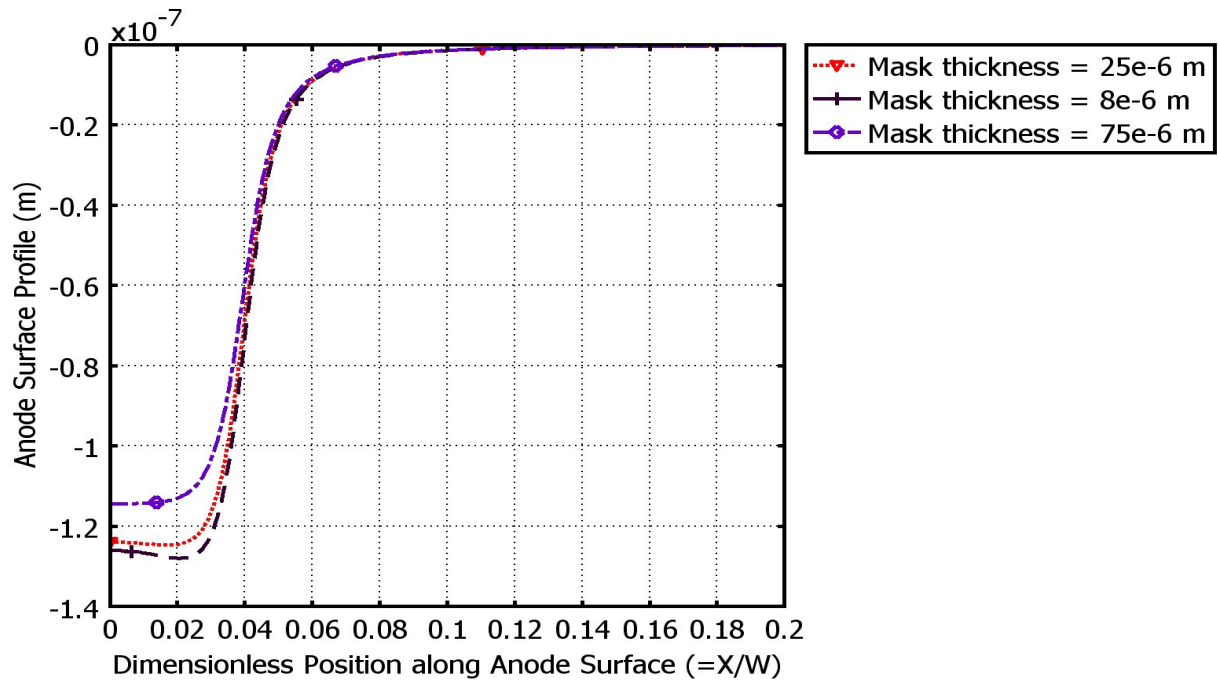


Figure 3.26 Variation of imprinted profile with various values of mask thickness, for mask opening = $1e-4$ m

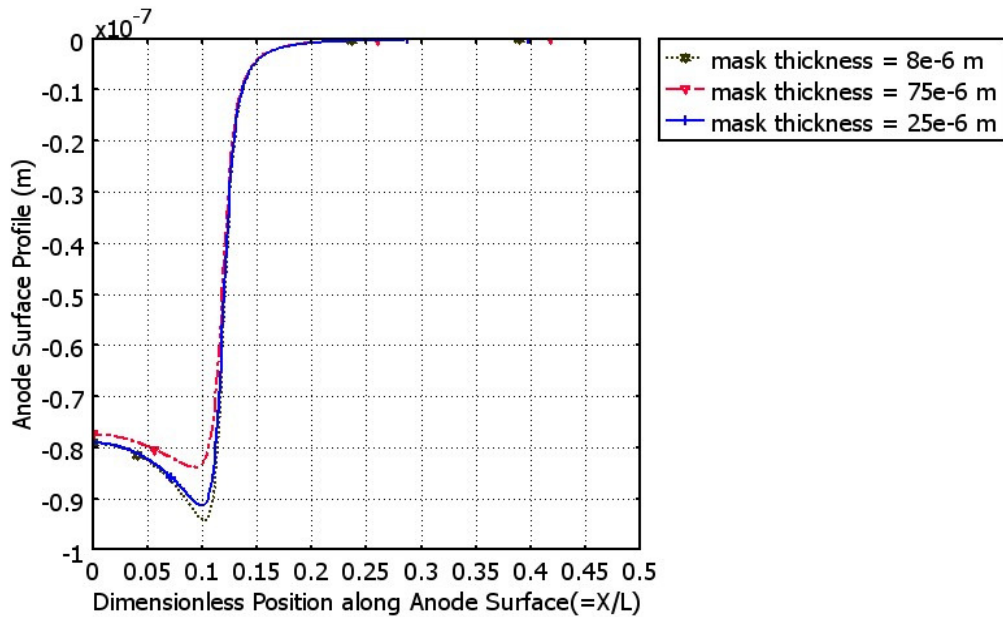
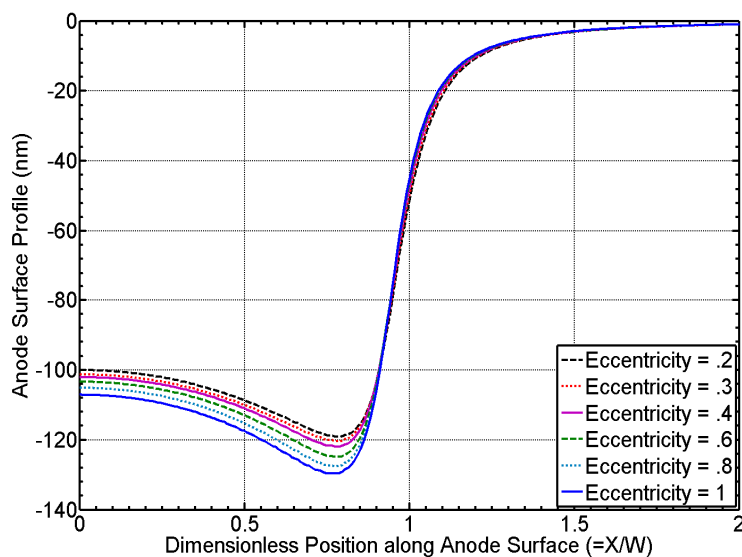


Figure 3.27 Variation of imprinted profile with various values of mask thickness, for mask opening = $3\text{e-}4$ m

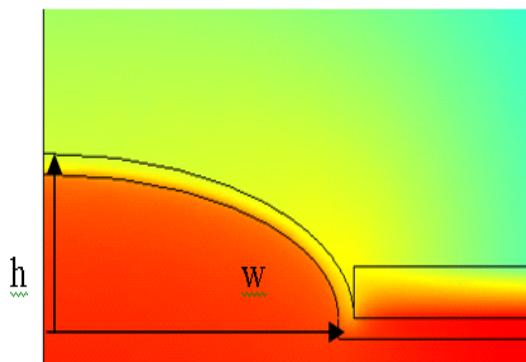
Figure 3.25 plots the variation of the anode surface profile with increase in the thickness of the membrane. We plot the anode surface profile at three values of the membrane thickness: $12.5\ \mu\text{m}$, $25\ \mu\text{m}$ and $50\ \mu\text{m}$. The membrane thickness has a remarkable effect on the depth of cut on the anode surface. We find that increasing the membrane thickness decreases the depth of cut by a significant amount. This arises due to the fact that the membrane diffusivity and conductivity are much less than that of the electrolyte, for all ions. Specifically, the membrane diffusivity (proportional to the conductivity) for Copper, sulphate and hydrogen ion is 7.5, 31 and 23 times lower than that of the electrolyte. Hence a thicker membrane provides much higher resistance to the transport of the ions from the anode to the cathode, which results in a monotonic decrease in the effective ionic current for the same potential drop. This results in a decrease in the depth of cut of the anode.

Figure 3.26 and Figure 3.27 plots the variation of the anode surface with change in the mask thickness at two distinct opening radius. As shown earlier, at small relative mask opening, the electric field produced by the mask edge also contributes to the etching of the anode at the center. When the mask thickness increase, the mask appears to have a low effective curvature (lower value of $T_{mask} / (T_{membrane} + T_{gap})$), hence leading to a decrease in the electric field contribution on the anode surface. Since the etching of the anode depends on the electric field produced by the mask, an increase in the thickness leads to a decrease in the material removal rate and hence the depth of cut on the anode surface.

3.8. Variation with curvature of membrane



(a)



(b)

Figure 3.28 (a) Variation of the imprinted profile with eccentricity/curvature of membrane, eccentricity = h/w . While eccentricity is not equal to the curvature it is proportional to the curvature of the membrane. (b) Schematic depicting the eccentricity of the membrane.

Figure 3.28 shows the variation of the imprinted profile with curvature of the membrane. The curved nature of the membrane tends to curve and focus the electric lines of force originating from the cathode. Due to this focusing nature of the curved membrane, the electric field produced at the surface of the anode increases, which in turn leads to larger number of ions being removed from the anode. Hence we find an increase in the net dissolution rate at the anode. The increase in the etching is almost uniform over the entire region under the opening. However since a larger number of electric lines of force are focused within the opening, fewer fringe lines of force reach the ends of the cell thus. Thus we find a slightly reduction of the etching rate away from the mask edge as the curvature is increased. This slight reduction in the mask etching away from the edge and a higher etching within the opening, also gives rise to a sharper slope of the torroidal structure.

3.9. Variation of surface profile with time

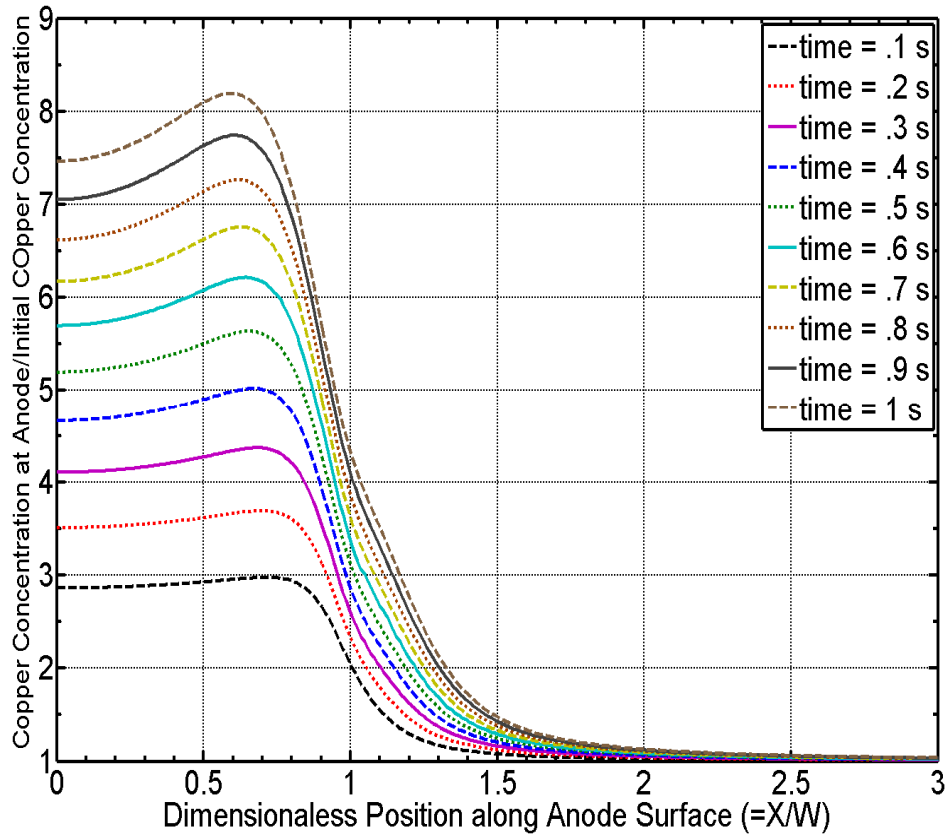


Figure 3.29 Variation of Dimensionless Copper concentration over anode surface, with time, mask opening= 200×10^{-6} m

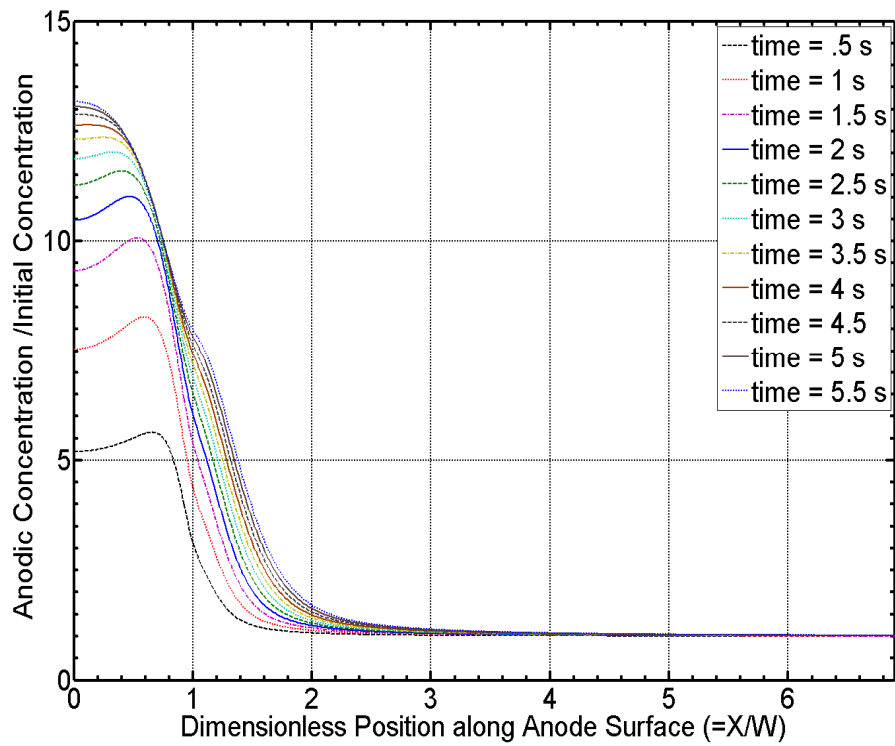


Figure 3.30 Variation of the concentration profile on anode surface with time, at long time scales

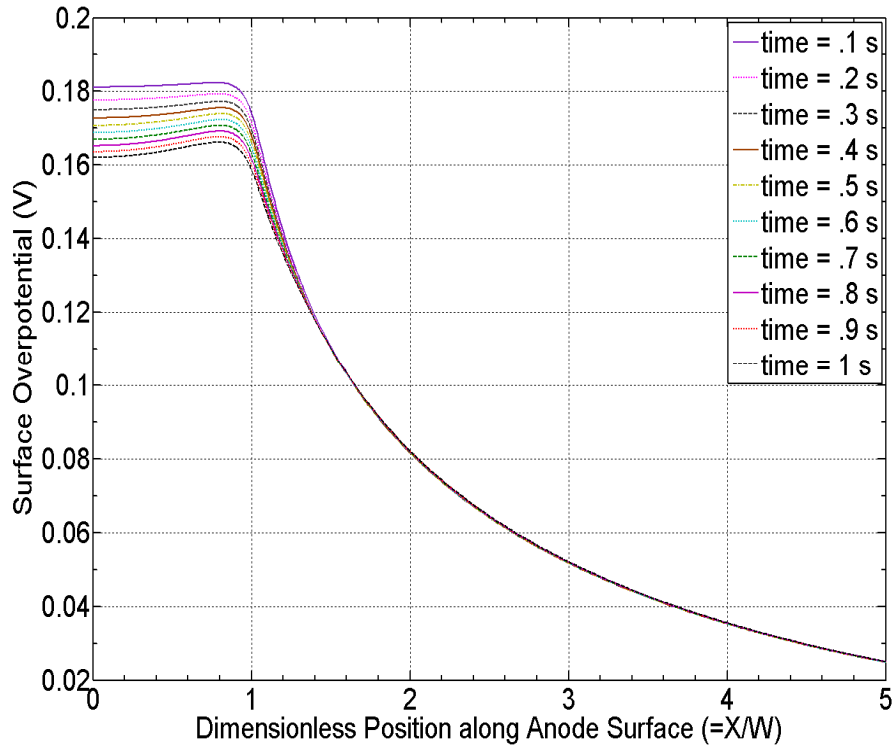


Figure 3.31 Variation of Effective surface overpotential($(V - V_{cu}) - U_{anode}$) along anode surface, mask opening= $200e-6$ m

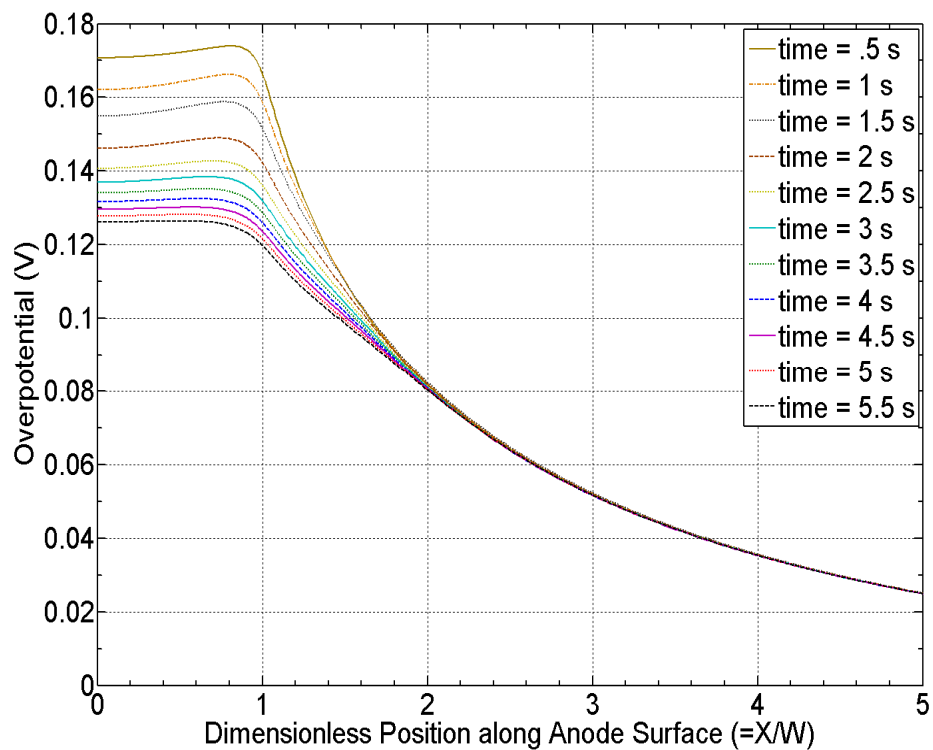


Figure 3.32 variation of the Surface Overpotential at the anode surface, at long time scales

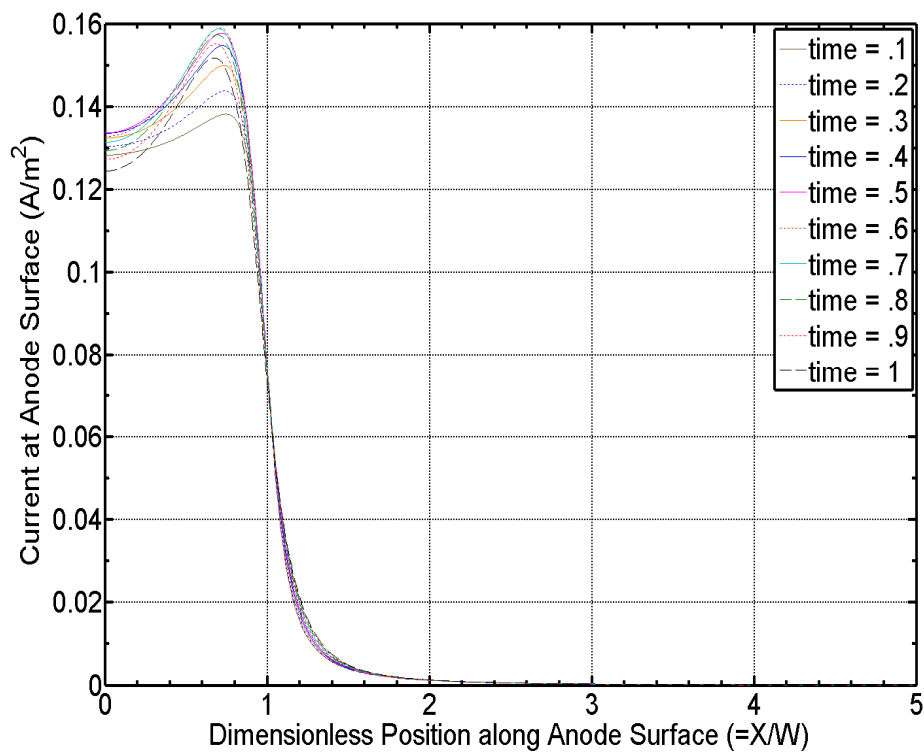


Figure 3.33 Variation of anodic current density with time, mask opening= 200e-6 m

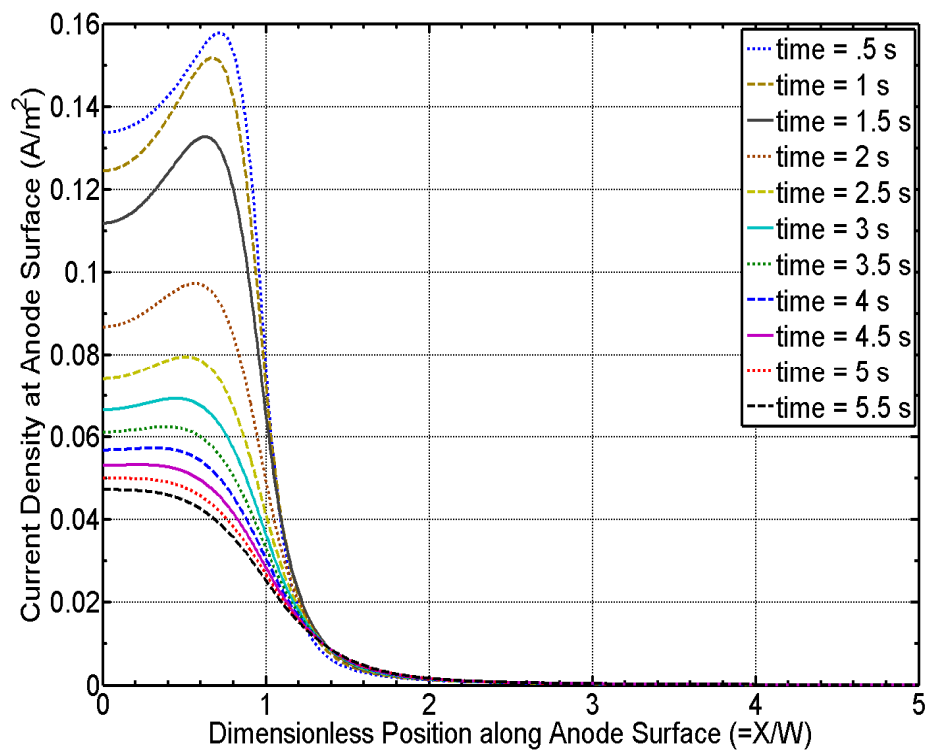


Figure 3.34 Variation of the current density at anode surface, at long time scales

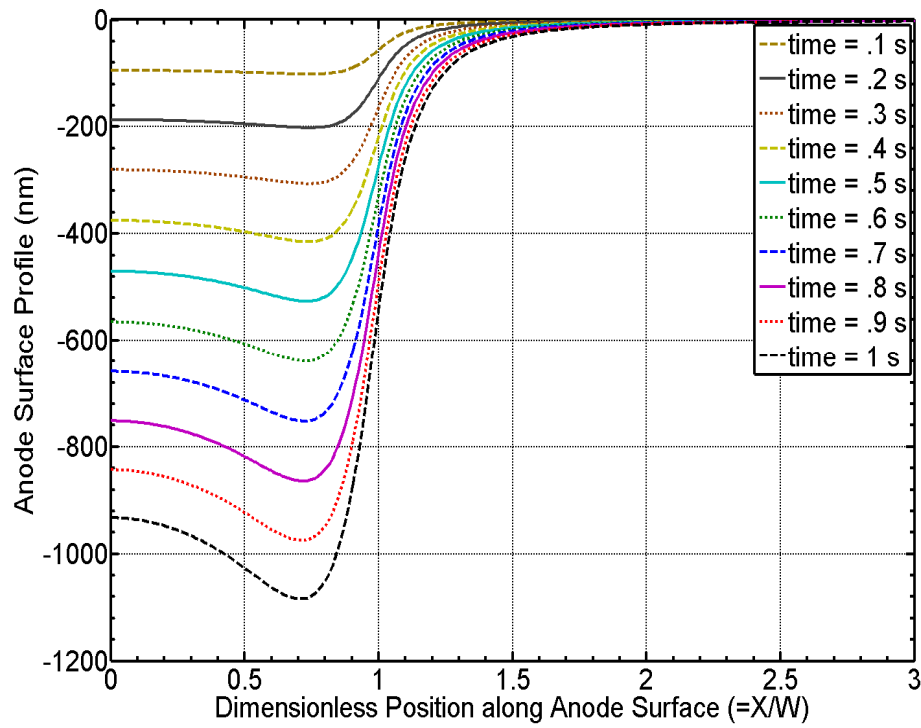


Figure 3.35 Variation of imprinted surface profile, mask opening= 200×10^{-6} m

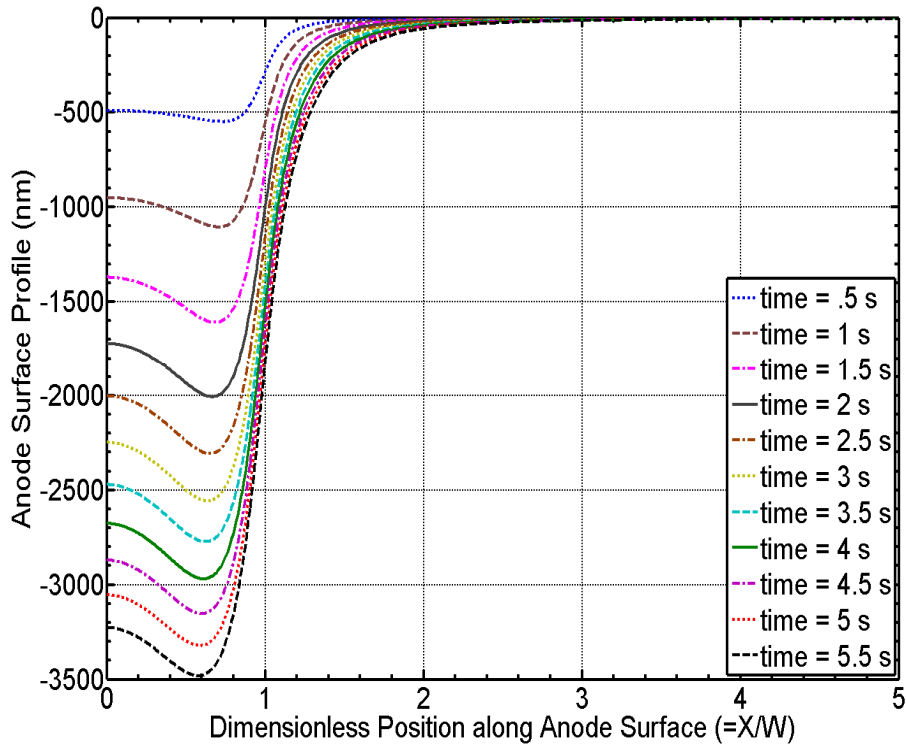


Figure 3.36 Variation of the imprinted surface profile, at long time scales.

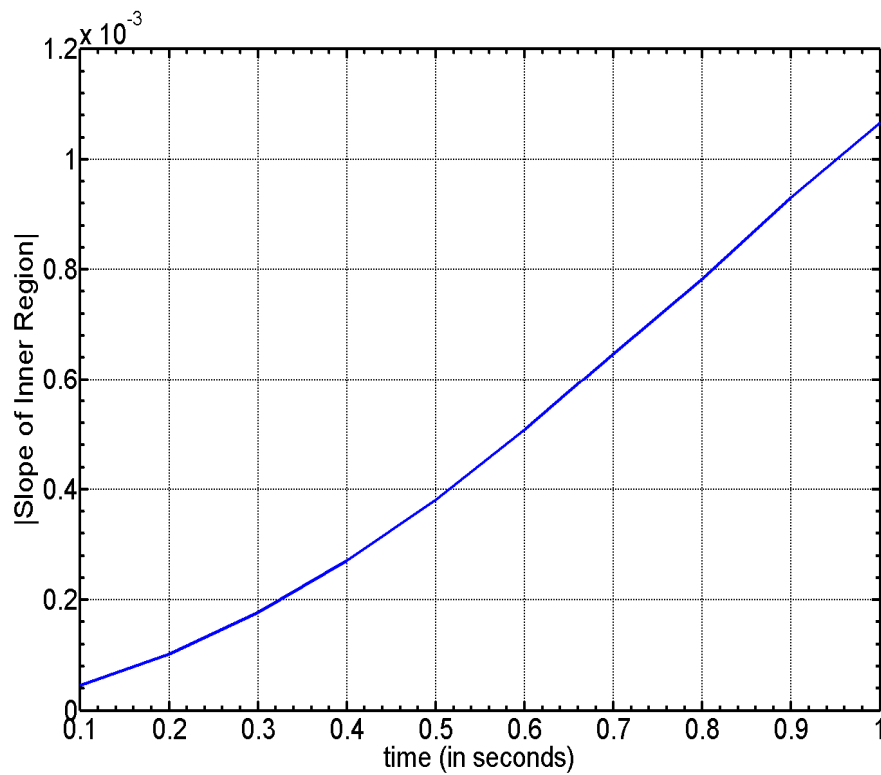


Figure 3.37 Variation of the average slope of the anode surface within the mask opening with time. Note that the shown slope slightly understates the actual slope due to the nature of the calculation.

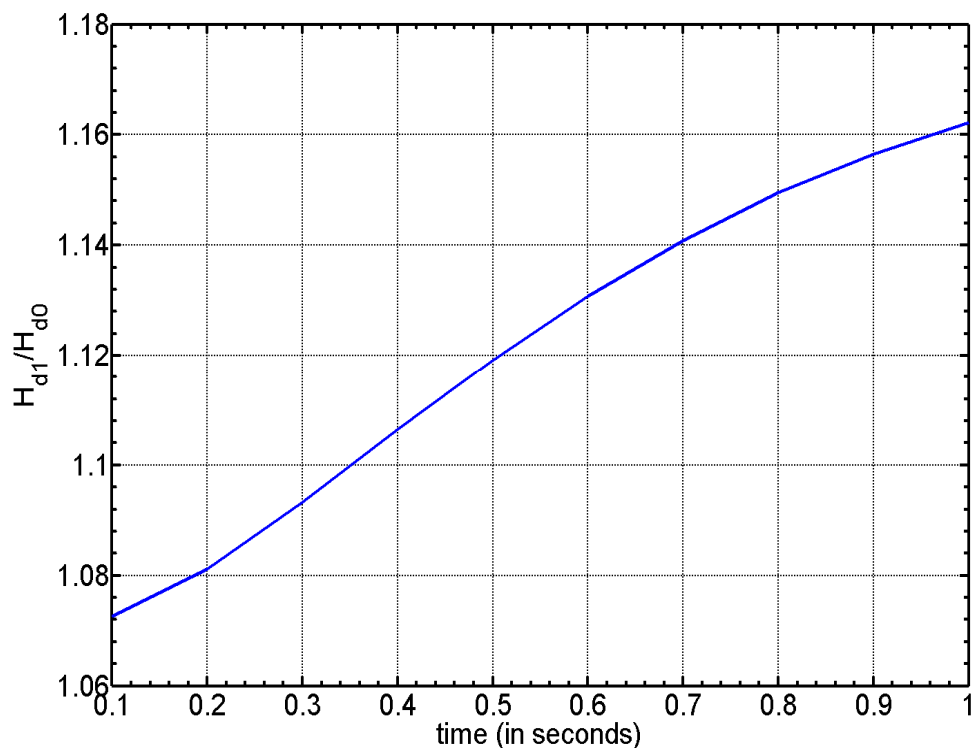


Figure 3.38 Variation of Ratio H_{d1}/H_{d0} with time. H_{d1} =displacement of bottom most point on the profile from the original anode surface, H_{d0} =displacement at the center of the mask opening

To understand the variation of the surface profile with passage of time we plot Figure 3.29 - Figure 3.35. Figure 3.35 shows the variation of the imprinted profile with time. With the onset of a potential difference between the cathode and the anode, the imprinted profile tends to shift by a constant magnitude in the opening of the mask, with a slightly increased value at the edge. As time progresses and the anode is incrementally etched, it appears that the anode surface just beneath the edge of the mask, tends to be etched at a higher rate compared to that of the region at the center of the cell. The reason for this is illustrated by plotting Figure

3.29 to Figure 3.33. It must be remembered that in these simulations the potential at the anode-electrolyte interface or the cathode-electrolyte interface is not held constant but is determined by the Butler-Volmer equation. The simulation starts with a zero potential everywhere in the cell. Hence there is a very high current density at the start of the simulation. This high current density results in generation of a high copper ion density just near the surface of the anode. However copper ions far away from the opening, face far more resistance to move. As a result only limited number of copper ions can be removed away from the anode, the farther we move away from the opening. Since only a small amount of copper can be moved away, and thus generated, the surface overpotential obtained is lower as we move away from the opening. (On the contrary, if a high surface overpotential were present far away from the opening, a very high electric field would have to be present away from the opening, to remove the high amount of copper ions generated, so as to overcome the high resistance for the copper ions to move towards the opening, which is not possible under these circumstances). The effective surface overpotential is almost uniform underneath the opening, with a slight bump at the edges. This increase arises because of the increased electric field underneath the mask edge. Because of this increased electric field, generated by the discontinuity in the dielectric constant, the flux of copper ions that can be sustained is comparatively higher than at the center of the opening, where the electric field is lower. Hence a higher overpotential and a higher anodic current is obtained.

Figure 3.37 and Figure 3.38 plot two distinct measures of the sharpness of the torroidal feature formed just beneath the edge of the mask. It can be seen that the slope of the surface within the opening, increases almost exponentially. It is interesting to note that the anodic current also becomes increasingly sharp at the position corresponding to the mask edge. Because of the higher flux at the position corresponding to the mask edge, a higher number of copper ions reside at the anode surface. (This is similar to having a high heat flux at the surface of an object. Higher the heat flux, higher will be the temperature of the surface on which the heat flux is

imposed). Since the anodic current is proportional to the copper concentration, the anodic current density too tends to become sharper as time progresses. Hence we observe a higher aspect ratio of the torus shaped structure generated on the mask. While the position corresponding to the mask edge becomes increasingly sharp, it should also be noticed that the overall etching rate (MRR) tends to decrease with time. This can be clearly observed from Figure 3.36. Here we plot the surface profile upto time = 5.5 s. Further proof of this can be seen from the current density variation at time = 5.5 seconds from Figure 3.34, which shows that the current density initially increases and becomes sharper. However beyond a certain critical time scale, the current density tends to flatten out and start decreasing with time. It is expected that the current density will eventually attain a fixed distribution over the entire anode surface, perturbed only by the changing surface shape of the anode. Since the anode current density at the mask opening center is higher than that beneath the anode, the sharp feature obtained should eventually be completely erased. It is also interesting to note that while the current density initially increases and then decreases, the copper ion density doesn't go through this bifurcation, rather it increases monotonically and then equilibrates to an asymptotic value, determined only by the surface shape of the anode.

3.10. Variation with Electrode potential

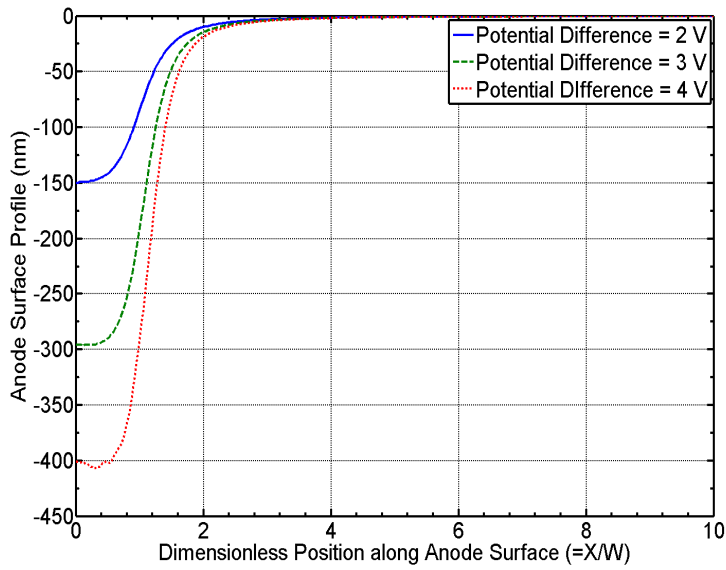


Figure 3.39 Variation of the imprinted profile with potential difference between anode and cathode

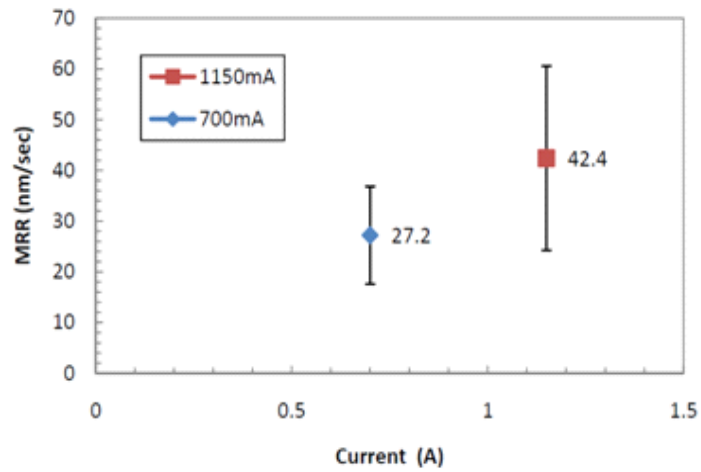


Figure 3.40 Variation of Material removal rate with current from experimental setup for Non-contact mask modulated electric field printing

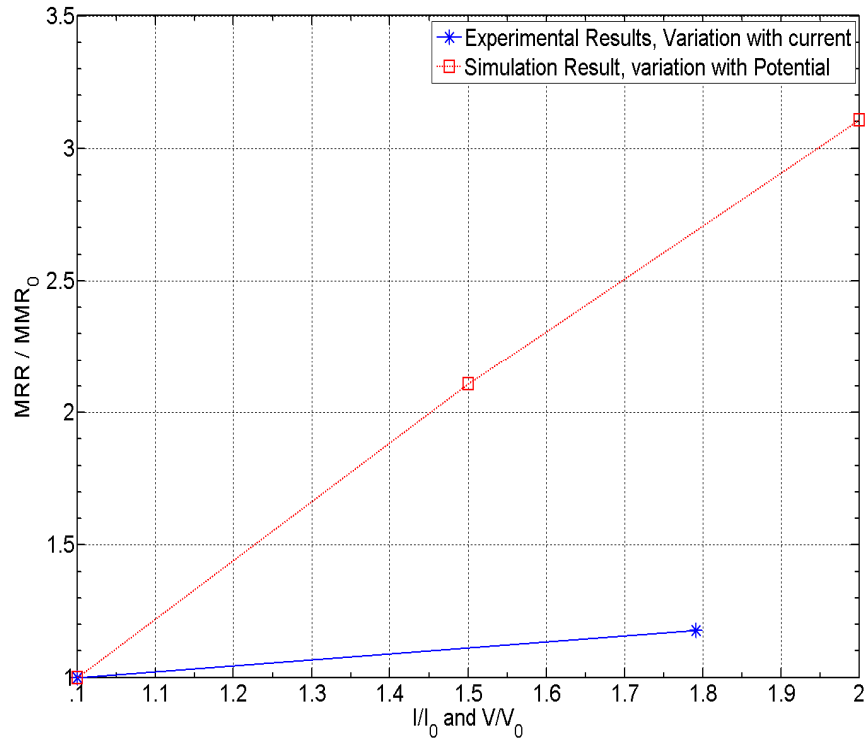


Figure 3.41 Variation of Material removal rate (nm/s) with current (experiment) and voltage(simulation) respectively.

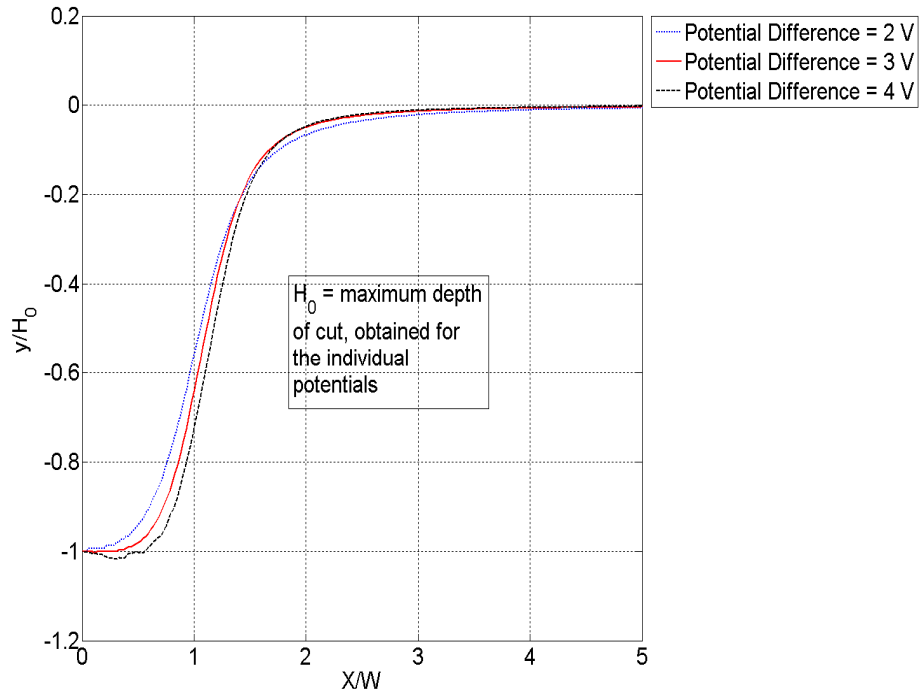


Figure 3.42 Variation of dimensionless imprinted profile depicting the flattening of the bottom surface with increasing potential difference between anode and cathode.

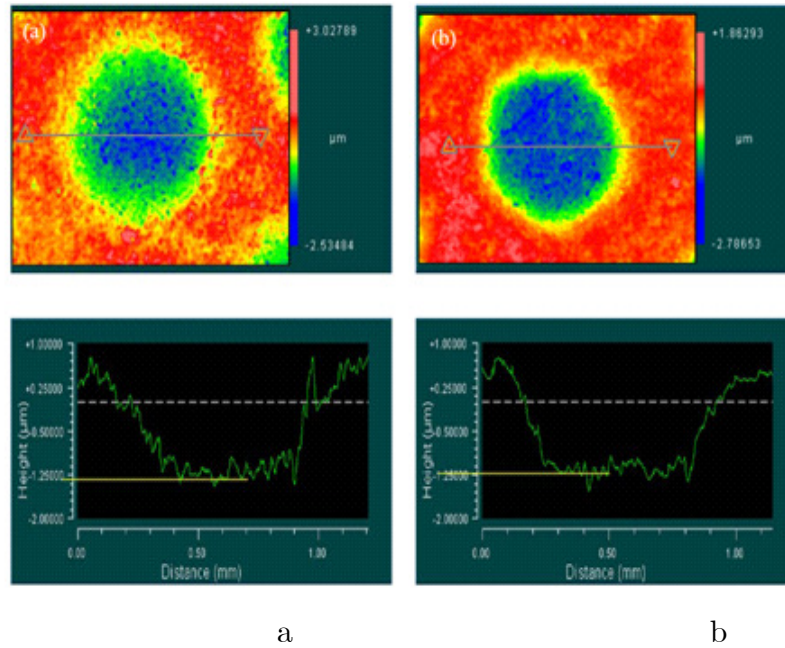


Figure 3.43 Experimentally obtained profile using stainless steel 570 μm mask, (a) $I = 1.052 \text{ A}$ (b) $I = 1.885 \text{ A}$ (DC voltage, standoff distance = 150 μm . Exposure = 300 sec, electrolyte = 1.80 M H_2SO_4 + 0.25 M CuSO_4)

As expected, with a larger applied electric potential difference between the anode and the cathode, a larger erosion of the copper substrate takes place. This occurs due to the generation of higher electric fields in the domain and at the boundaries, thus removing the generated copper ions at the anode to the cathode. This results in a decrease in the surface overpotential, thus giving rise to a higher rate of material removal. A similar trend can be observed from the experimental results as well. As seen from Figure 3.40 the material removal rate tends to increase with the current density. However it should also be observed from the figure, that the net change in the surface profile per Volt increase in the potential difference decreases with increasing potential difference. While the experimental and numerical results cannot be directly compared we can compare the dimensionless values. Figure 3.41 plots the non-dimensionalized values and compares the experimental and theoretical results. In these cases the non-dimensionalization is carried out using the least potential difference and depth of cut for experimental and numerical results obtained. While the trends predicted are correct, the simulation and experimental trends tend to differ by a magnitude of around 3. This suggests that some sort of passivation might be taking place at the anode surface, and hence relatively lower increase in the MRR. The Butler-Volmer equation used here, doesn't consider passivation of the anode, and hence results in the overprediction of the MRR.

3.11. Variation with H_2SO_4 concentration

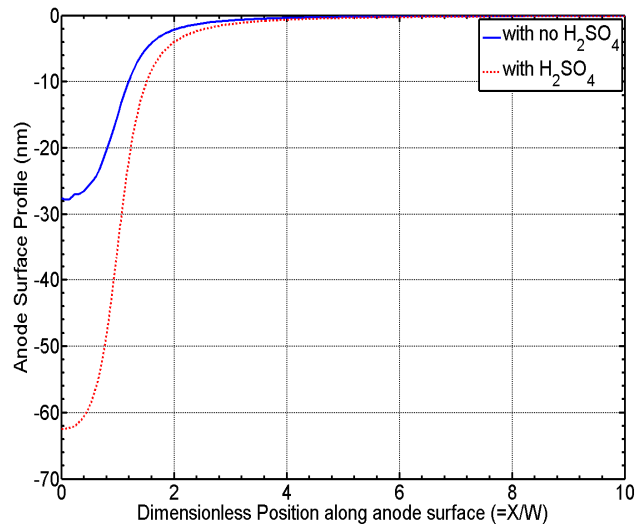


Figure 3.44 Variation of imprinted profile with/without H_2SO_4 at time $t=.04$ seconds

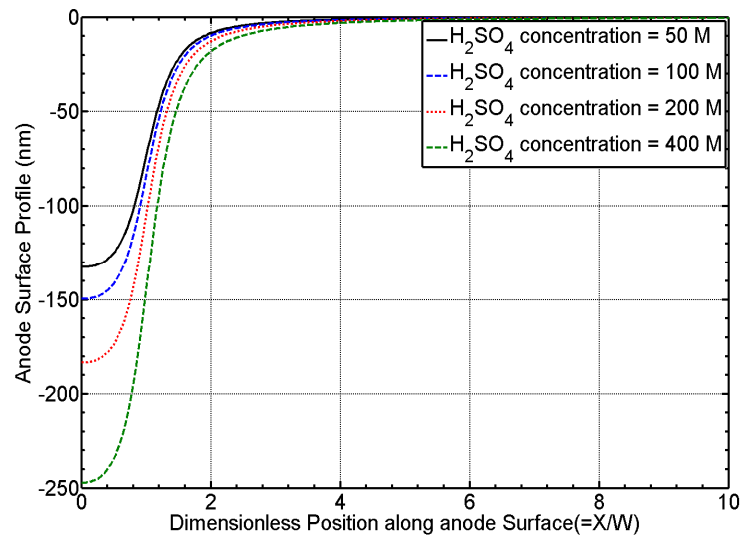


Figure 3.45 Variation of imprinted profile with various concentrations of H_2SO_4

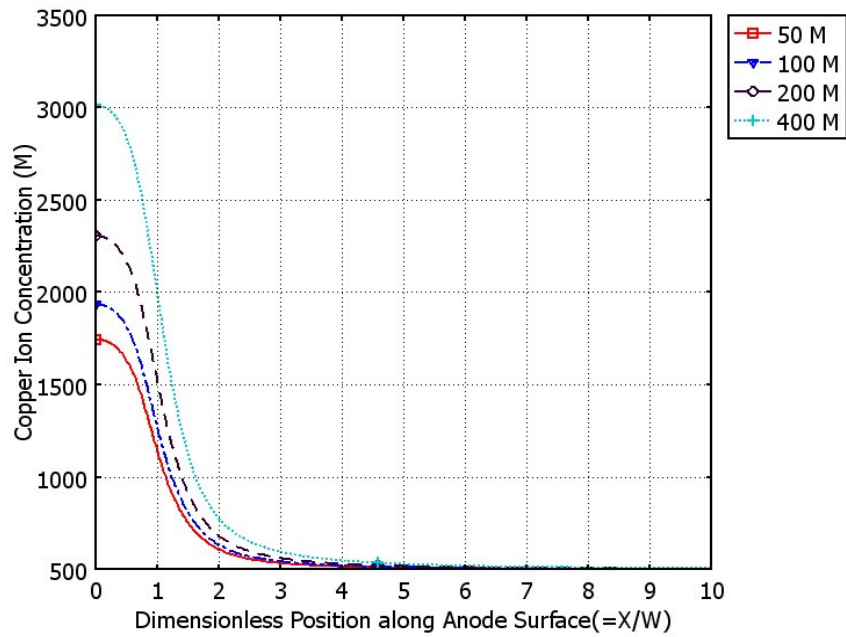


Figure 3.46 Variation of Copper Ion Concentration with concentration of sulphuric acid

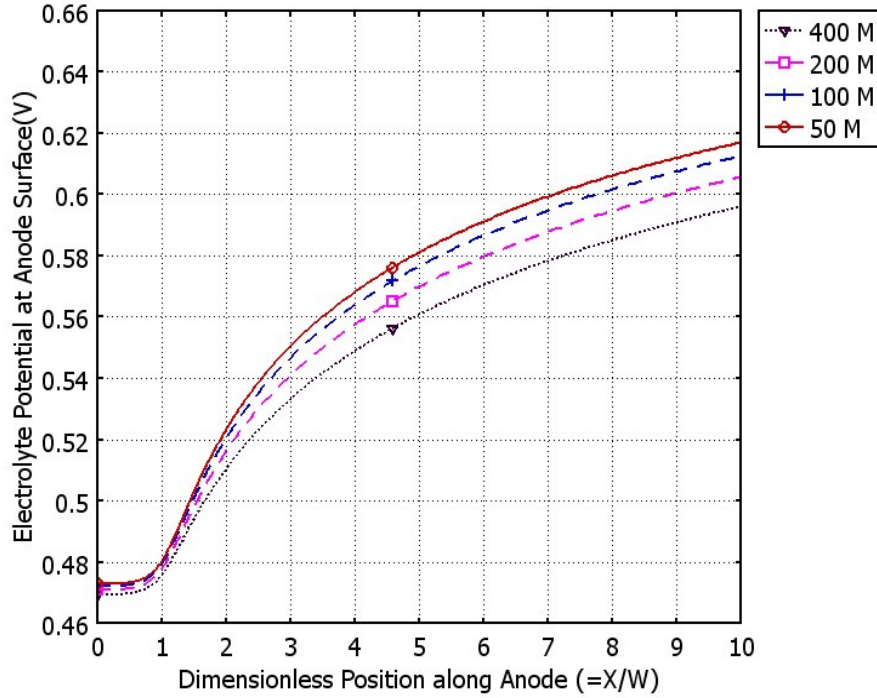


Figure 3.47 Variation of Potential at Electrolyte-Anode Interface with sulphuric acid concentration

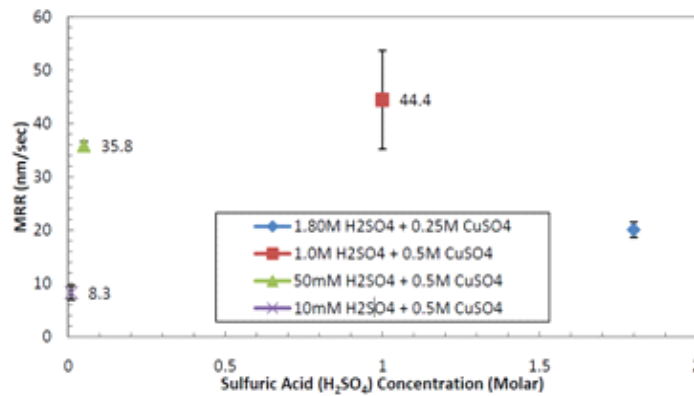


Figure 3.48 Perforated stainless steel 570 μ m, comparison of MRR at different electrolyte concentrations. (DC voltage, Insulated perforated stainless steel hole, insulated cathode chamber with added round electrode, P = 1inHg, standoff distance = 20 μ m, exposure = 60sec.)

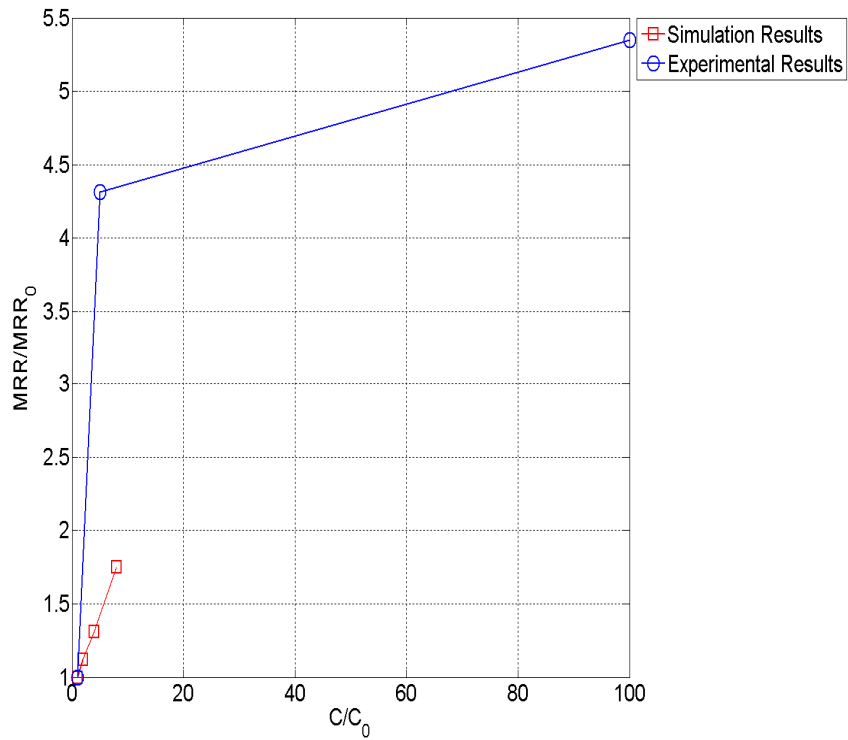


Figure 3.49 Variation of Dimensionless MRR (nm/s) with concentration of sulphuric acid

To understand the increase in the depth of cut with increasing concentration of sulphuric acid, we plot the copper ion concentration and the electrolyte potential at the anode in Figure 3.46 and Figure 3.47 respectively. From Section 2.1.3, we know that the copper ion anodic current density depends both on the copper ion concentration as well as the surface overpotential at the anode surface. As the copper ion concentration goes up for constant surface overpotential, we should expect an increase in the anodic current and hence an increase in the material removal. Similarly for constant copper concentration we can expect an increase in the anodic current and hence the material removal with increase in surface overpotential.

Figure 3.46 shows us that for increasing concentration of sulphuric acid, the copper ion concentration at the anodic surface also tends to increase dramatically. The above phenomena can be explained by observing how the copper ions is generated and dissolved. For higher concentration of sulphuric acid, there are higher number of hydrogen ions and sulphate ions at the anode surface. When copper ions are generated at the anode, the charge neutrality is temporarily violated, and in an effort to neutralize the volume containing higher number of copper ions, sulphate ions can either move into the region containing a higher number of copper ions or hydrogen ions can move out of the region, and into the bulk of the electrolyte. In actual practice, both phenomenon occur simultaneously. However since hydrogen has a much higher diffusivity and mobility, it is expected that the movement of hydrogen ion away from the electrolyte will occur faster and will thus determine the copper dissolution rate. A higher number of hydrogen ions present in the vicinity would mean that it can sustain and facilitate a higher rate of copper dissolution. Hence as the sulphuric acid concentration increases we find an increase in the copper ion concentration and an increase in the dissolution rate at the anode surface. While there is a small change in the surface overpotential at the anode, with change in the sulphuric acid concentration, the change is very small and is not expected to have any important effect on the copper dissolution rate.

Experimental data of the material removal rate as shown in Figure 3.48, show that the MRR increases with increasing concentration of sulphuric acid and copper sulphate. Hence the experimental results clearly support the above hypothesis.

3.12. Variation with mask and membrane dielectric constant

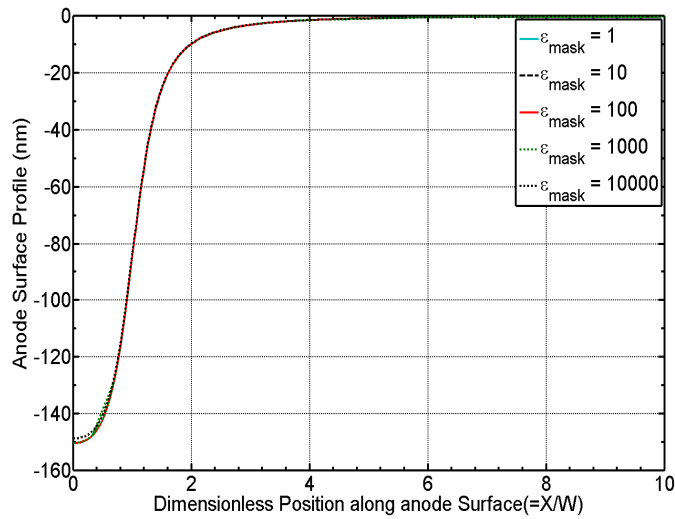


Figure 3.50 Variation of imprinted profile with various values of mask dielectric constant.

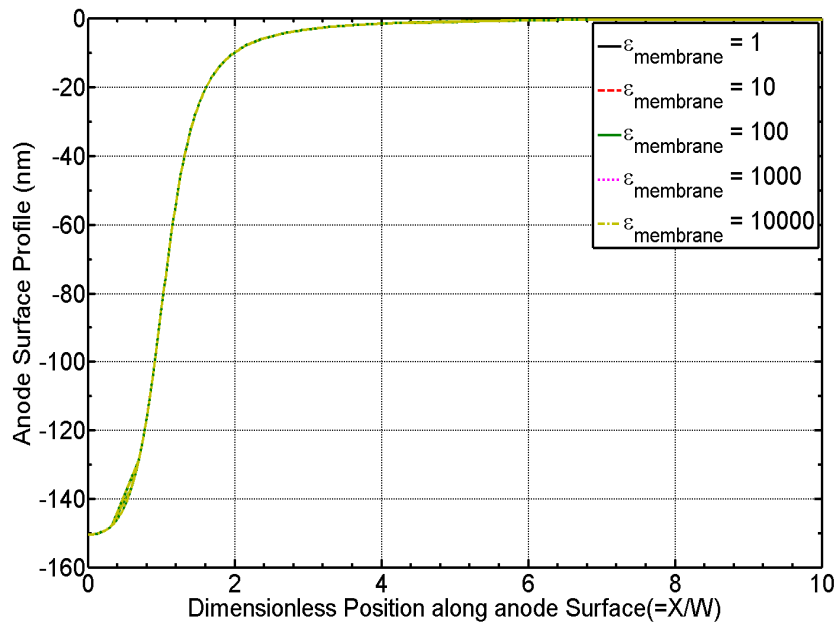


Figure 3.51 Variation of imprinted profile with various values of mask dielectric constant.

To understand the effect of the dielectric constant of the mask and the membrane on the dissolution, we plot Figure 3.50 and Figure 3.51. The above figures show that there is no effect of the variation of the dielectric constant of mask or the membrane on the anode surface profile. This lack of variation of the anode surface on the dielectric constants arise due to the small value of $\frac{\epsilon}{F}$. A more formal proof of this is derived below using perturbation theory.

We express c_{Cu} , c_{SO_4} , c_H and Φ as expansions in terms of the perturbation parameter $\frac{\epsilon}{F}$. Since c_{Cu} , c_{SO_4} , and c_H have similar governing equations, we expand the boundary and governing equations only for c_{Cu} and Φ .

Hence we obtain

$$c_{Cu} = c_{Cu}^0 + \left(\frac{\epsilon}{F}\right)c_{Cu}^1 + \left(\frac{\epsilon}{F}\right)^2 c_{Cu}^2 + \dots \quad (1.61)$$

$$\Phi = \Phi_{Cu}^0 + \left(\frac{\epsilon}{F}\right)\Phi_{Cu}^1 + \left(\frac{\epsilon}{F}\right)^2 \Phi_{Cu}^2 + \dots \quad (1.62)$$

Expanding Equation (1.38) we have

$$\frac{\partial c_{Cu}^0}{\partial t} + \left(\frac{\epsilon}{F}\right)\frac{\partial c_{Cu}^1}{\partial t} = z_{Cu} F u_{Cu} \left[\begin{array}{l} \nabla \cdot (c_{Cu}^0 \nabla \Phi^0) + \\ \left(\frac{\epsilon}{F}\right) \left\{ \begin{array}{l} \nabla \cdot (c_{Cu}^0 \nabla \Phi^1) \\ + \nabla \cdot (c_{Cu}^1 \nabla \Phi^0) \end{array} \right\} \end{array} \right] + \quad (1.63)$$

$$\begin{aligned} & D_{Cu} \left[(\nabla^2 c_{Cu}^0) + \left(\frac{\epsilon}{F}\right) (\nabla^2 c_{Cu}^1) + \dots \right] \\ & (z_{Cu} c_{Cu}^0 + z_{SO_4} c_{SO_4}^0 + z_H c_H^0) + \left(\frac{\epsilon}{F}\right) (z_{Cu} c_{Cu}^1 + z_{SO_4} c_{SO_4}^1 + z_H c_H^1) \\ & = -\frac{\epsilon}{F} \nabla^2 \Phi = -\left(\frac{\epsilon}{F}\right) \left(\nabla^2 \Phi^0 + \left(\frac{\epsilon}{F}\right) \nabla^2 \Phi^1 \right) \end{aligned} \quad (1.64)$$

$$\nabla^2 \Phi = \nabla^2 \Phi^0 + \left(\frac{\epsilon}{F}\right) \nabla^2 \Phi^1 = 0 \quad (1.65)$$

Hence we can separate the zeroth order and first order terms on both sides of Equation (1.63) and Equation (1.64) to obtain the following equations

$$\frac{\partial c_{cu}^0}{\partial t} = z_{cu} F u_{cu} \nabla \cdot (c_{cu}^0 \nabla \Phi^0) + D_{cu} (\nabla^2 c_{cu}^0) \quad (1.66)$$

$$\frac{\partial c_{cu}^1}{\partial t} = z_{cu} F u_{cu} \left\{ \begin{array}{l} \nabla \cdot (c_{cu}^0 \nabla \Phi^1) \\ + \nabla \cdot (c_{cu}^1 \nabla \Phi^0) \end{array} \right\} + D_{cu} (\nabla^2 c_{cu}^1) \quad (1.67)$$

For Φ we have

$$(z_{cu} c_{cu}^0 + z_{SO_4} c_{SO_4}^0 + z_H c_H^0) = 0 \quad (1.68)$$

$$(z_{cu} c_{cu}^1 + z_{SO_4} c_{SO_4}^1 + z_H c_H^1) = -\nabla^2 \Phi^0 \quad (1.69)$$

As we can see from the above Equations (3.6) – (3.9), the value of ϵ , doesn't affect the value of Φ^0, Φ^1, c_{cu}^0 or c_{cu}^1 . The term $\frac{\epsilon}{F}$ enters and affects the total solution only through the first order expansion term as shown in Equation (1.61) and Equation (1.62). Assuming that the zeroth order first order terms of the concentration and potential fields are of approximately the same magnitude, since $\frac{\epsilon}{F}$, has a value of 1×10^{-16} , we can conclude that any reasonable change in the dielectric constant of the mask, membrane or electrolyte won't cause any observable change in the amount of material removal, the shape of the anode or the concentration distribution. This was also tested numerically, by substituting a value of ~ 1 , for $\frac{\epsilon}{F}$, and observing the change when $\frac{\epsilon}{F}$ was varied. We did obtain significant changes in the material removal, the shape of the anode or the concentration distribution. The above derivation only shows the governing equation so as to show the basis of the argument, however a complete derivation considering the three dielectric constants of the membrane, electrolyte and mask, and the effect of the boundary conditions is expected to lead to the same conclusions.

No comparison of the above simulations could be made to experiments since, there was no experimental data using different mask and membrane materials, and using similar sizes and periodicity of the mask.

CHAPTER 4 CONCLUSION

The present thesis provides a basic model to understand various experimental results which were obtained by Khiam et al. Electrochemical phenomenon are complex and require solving multiple coupled equations simultaneously. Further at micro/nanoscales the phenomena become stochastic. Hence to get accurate simulation results it is necessary to carry out stochastic simulations at the microscale coupled with continuum simulations at the macroscale. The model presented here can be vastly improved if a more rigorous method of implementation using finite element codes which can be modified with appropriate numerical methods to capture the proper phenomena. Since the process was simulated with a commercial generalized finite element code made primarily for linear system of equations, and the system being studied had non-linear boundary conditions, I believe the software had some difficulty capturing the phenomena properly. While there are algorithms to capture these non-linear phenomena properly, they cannot be directly incorporated into the software, since the source code for COMSOL cannot be altered or modified. Secondly, the software becomes very unstable as the model becomes complicated. Only basic models for the Nafion, the electrolyte, the interfaces and the electrode kinetics could be incorporated. While attempts were made to incorporate improved models for Nafion and the electrode kinetics, simulations couldn't be run properly.

In spite of these inherent problems, the present model does support the basic phenomena observed in the experiments qualitatively, especially for direct current simulations. Comparisons of the simulation results with the experimental results show that the model captures the trends quite well. Chopped DC simulations however are not very well correlated to the simulation results obtained here. It is presumed that some other phenomena occur in this case, which is not captured properly in these simulations. However a physical reasoning can be drawn by observing the variation of the surface profile, current density with time. It is seen that while the profile as well as the current density becomes sharper with increase in

time, beyond a critical value of time, the current density tends to become parabolic in shape with the highest value being obtained at the center of the mask opening. Hence at some point in time history, it is expected that the indentation obtained at lower time scales will be erased and the final surface left will have a parabolic profile as well, for all values of the mask radius. It seems Chopped DC simulations, somehow stop this evolution of the parabolic current density profile, and initiate the generation of sharpened current density profile at repeated intervals of time. Further, studies at smaller values of the opening radius show that this critical value of time depends on the opening radius, and with increase in the opening radius, this critical value of time tends to increase. Hence to obtain an optimally sharp indentation, we need to know this critical value of time, so that the frequency of the oscillation of the potential can be modified.

These simulations also indicate the importance of various length scales in determining appropriate surface features. While it was initially predicted that the curvature of the membrane would play a significant role in determining the shape of the profile, simulations seem to indicate the role is actually small. There is definitely an increase in the feature depth with increase in curvature; however, the increase is small compared to similar changes in the length scale of other features. Particularly, the opening radius, the standoff distance between the anode and the cathode, and the thickness of the mask/membrane, seem to play significant roles determining the shape of the features. It is observed that two non-dimensional parameters $W/(T_{\text{membrane}} + T_{\text{gap}})$ and $[T_{\text{mask}} / (T_{\text{membrane}} + T_{\text{gap}})]$ play significant roles in determining the shape of the features. The overall shape of the profile is determined primarily by $W/(T_{\text{membrane}} + T_{\text{gap}})$. $T_{\text{mask}} / (T_{\text{membrane}} + T_{\text{gap}})$ on the other hand determines the sharpness of the indentation depth.

ACKNOWLEDGEMENTS

I would like to take this opportunity to express my thanks to those who helped me with various aspects of conducting research and the writing of this thesis. First and foremost, I would like to thank Prof. Abhijit Chandra and Prof. Ashraf Bastawros for their guidance, patience and support throughout this research and the writing of this thesis. Their insights and words of encouragement have often inspired me and throughout my journey towards the completion of my masters degree. I would also like to thank Prof. Liang Dong for serving on my committee. I would additionally like to thank my friends and family for their support and encouragement throughout my master degree program.

BIBLIOGRAPHY

1. Georgiadou, M. and R. Alkire, *Anisotropic Chemical Pattern Etching of Copper Foil*. Journal of the Electrochemical Society, 1994. **141**(3): p. 679-689.
2. Georgiadou, M. and R. Alkire, *Modelling of copper etching in aerated chloride solutions*. Journal of Applied Electrochemistry, 1997. **28**(2): p. 127-134.
3. Georgiadou, M., R. Mohr, and R.C. Alkire, *Local Mass Transport in Two-Dimensional Cavities in Laminar Shear Flow*. Journal of the Electrochemical Society, 2000. **147**(8): p. 3021-3028.
4. Georgiadou, M., et al., *Simulation of Shape Evolution during Electrodeposition of Copper in the Presence of Additive*. Journal of the Electrochemical Society, 2001. **148**(1): p. C54-C58.
5. Pricer, T.J., M.J. Kushner, and R.C. Alkire. *Monte Carlo simulations of the electrodeposition of copper*. in *International Symposium on Fundamental Aspects of Electrochemical Deposition and Dissolution*. 1999. Honolulu, Hi: Electrochemical Society Inc.
6. Pricer, T.J., M.J. Kushner, and R.C. Alkire, *Monte Carlo simulation of the electrodeposition of copper - I. Additive-free acidic sulfate solution*. Journal of the Electrochemical Society, 2002. **149**(8): p. C396-C405.
7. Drews, T.O., et al., *Multiscale simulations of copper electrodeposition onto a resistive substrate*. Ibm Journal of Research and Development, 2005. **49**(1): p. 49-63.
8. Drews, T.O., et al., *Stochastic simulation of the early stages of kinetically limited electrodeposition*. Journal of the Electrochemical Society, 2006. **153**(6): p. C434-C441.
9. Li, X.H., et al., *Effect of additives on shape evolution during electrodeposition: I. Multiscale simulation with dynamically coupled kinetic Monte Carlo and moving-boundary finite-volume codes (vol 154, pg D230, 2007)*. Journal of the Electrochemical Society, 2007. **154**(7): p. S15-S15.

10. Stephens, R.M. and R.C. Alkire, *Simulation of kinetically limited nucleation and growth at monatomic step edges*. Journal of the Electrochemical Society, 2007. **154**(8): p. D418-D426.
11. Drews, T.O., R.D. Braatz, and R.C. Alkire, *Monte Carlo simulation of kinetically limited electrodeposition on a surface with metal seed clusters*. Zeitschrift Fur Physikalische Chemie-International Journal of Research in Physical Chemistry & Chemical Physics, 2007. **221**(9-10): p. 1287-1305.
12. Rusli, E., et al., *Effect of additives on shape evolution during electrodeposition - II. Parameter estimation from roughness evolution experiments*. Journal of the Electrochemical Society, 2007. **154**(11): p. D584-D597.
13. Zheng, Z.M., et al., *A hybrid multiscale kinetic Monte Carlo method for simulation of copper electrodeposition*. Journal of Computational Physics, 2008. **227**(10): p. 5184-5199.
14. Stephens, R.M. and R.C. Alkire, *Island Dynamics Algorithm for Kinetically Limited Electrochemical Nucleation of Copper with Additives onto a Foreign Substrate*. Journal of the Electrochemical Society, 2009. **156**(1): p. D28-D35.
15. Mattsson, E. and J.O. Bockris, *GALVANOSTATIC STUDIES OF THE KINETICS OF DEPOSITION AND DISSOLUTION IN THE COPPER + COPPER SULPHATE SYSTEM*. Transactions of the Faraday Society, 1959. **55**(9): p. 1586-1601.
16. Mehl, W. and J.O.M. Bockris, *MECHANISM OF ELECTROLYTIC SILVER DEPOSITION AND DISSOLUTION*. Journal of Chemical Physics, 1957. **27**(3): p. 818-819.
17. Bockris, J.O. and M. Enyo, *MECHANISM OF ELECTRODEPOSITION AND DISSOLUTION PROCESSES OF COPPER IN AQUEOUS SOLUTIONS*. Transactions of the Faraday Society, 1962. **58**(474): p. 1187-&.
18. Pirogov, B.Y. and A.G. Zelinsky, *Numerical simulation of electrode process in Cu/CuSO₄ + H₂SO₄ system*. Electrochimica Acta, 2004. **49**(20): p. 3283-3292.
19. Zelinsky, A.G. and B.Y. Pirogov, *Numerical simulation of corrosion process with two-step charge transfer mechanism in the Cu/CuSO₄ + H₂SO₄ system*. Corrosion Science, 2006. **48**(10): p. 2867-2881.

20. Pirogov, B. and A. Zelinskii, *Mass transport and effective diffusion coefficient in the reduction of hydrogen ions from aqueous sulfuric acid solutions: Numerical modeling*. Russian Journal of Electrochemistry, 2009. **45**(3): p. 336-344.
21. Gurau, V., F. Barbir, and H. Liu, *An Analytical Solution of a Half-Cell Model for PEM Fuel Cells*. Journal of the Electrochemical Society, 2000. **147**(7): p. 2468-2477.
22. Marr, C. and X. Li, *Composition and performance modelling of catalyst layer in a proton exchange membrane fuel cell*. Journal of Power Sources, 1999. **77**(1): p. 17-27.
23. Newmann, J. and K.E. Thomas-Alyea, *Electrochemical Systems*. 2004, New York: John Wiley & Sons.
24. Einstein, A., *Über die von der molekularkinetischen Theorie der Wärme geforderte Bewegung von in ruhenden Flüssigkeiten suspendierten Teilchen*. Annalen der Physik, 1905. **322**(8): p. 549-560.
25. Springer, T.E., T.A. Zawodzinski, and S. Gottesfeld, *Polymer Electrolyte Fuel Cell Model*. Journal of the Electrochemical Society, 1991. **138**(8): p. 2334-2342.
26. Pintauro, P.N. and D.N. Bennion, *Mass transport of electrolytes in membranes. 1. Development of mathematical transport model*. Industrial & Engineering Chemistry Fundamentals, 1984. **23**(2): p. 230-234.
27. Fimrite, J., et al., *Transport Phenomena in Polymer Electrolyte Membranes*. Journal of the Electrochemical Society, 2005. **152**(9): p. A1815-A1823.
28. Thampan, T., et al., *Modeling of Conductive Transport in Proton-Exchange Membranes for Fuel Cells*. Journal of the Electrochemical Society, 2000. **147**(9): p. 3242-3250.
29. Weber, A.Z. and J. Newman, *Transport in Polymer-Electrolyte Membranes*. Journal of the Electrochemical Society, 2004. **151**(2): p. A311-A325.
30. Bernardi, D.M. and M.W. Verbrugge, *Mathematical model of a gas diffusion electrode bonded to a polymer electrolyte*. Aiche Journal, 1991. **37**(8): p. 1151-1163.

31. Bernardi, D.M. and M.W. Verbrugge, *A Mathematical Model of the Solid-Polymer-Electrolyte Fuel Cell*. Journal of the Electrochemical Society, 1992. **139**(9): p. 2477-2491.
32. Verbrugge, M.W. and R.F. Hill, *Ion and Solvent Transport in Ion-Exchange Membranes*. Journal of the Electrochemical Society, 1990. **137**(3): p. 886-893.
33. Verbrugge, M.W. and R.F. Hill, *Transport Phenomena in Perfluorosulfonic Acid Membranes during the Passage of Current*. Journal of the Electrochemical Society, 1990. **137**(4): p. 1131-1138.
34. Schlögl, R., *Über Kondensationen von Aldehyden mit einseitig n-substituierten Paradiaminen*. Journal für Praktische Chemie, 1913. **88**(1): p. 251-256.
35. Gurau, V., H. Liu, and S. Kakaç, *Two-dimensional model for proton exchange membrane fuel cells*. Aiche Journal, 1998. **44**(11): p. 2410-2422.
36. Janssen, G.J.M. and M.L.J. Overvelde, *Water transport in the proton-exchange-membrane fuel cell: measurements of the effective drag coefficient*. Journal of Power Sources, 2001. **101**(1): p. 117-125.
37. Kreuer, K.D., *On the development of proton conducting materials for technological applications*. Solid State Ionics, 1997. **97**(1-4): p. 1-15.
38. He, W., J.S. Yi, and T.V. Nguyen, *Two-phase flow model of the cathode of PEM fuel cells using interdigitated flow fields*. Aiche Journal, 2000. **46**(10): p. 2053-2064.
39. Meyers, J.P. 1998, University of California, Berkeley: Berkeley.
40. Li, J.Y. and S. Nemat-Nasser, *Micromechanical analysis of ionic clustering in Nafion perfluorinated membrane*. Mechanics of Materials, 2000. **32**(5): p. 303-314.
41. Nemat-Nasser, S. and J.Y. Li, *Electromechanical response of ionic polymer-metal composites*. Journal of Applied Physics, 2000. **87**(7): p. 3321-3331.
42. Nemat-Nasser, S. and S. Zamani, *Modeling of electrochemomechanical response of ionic polymer-metal composites with various solvents*. Journal of Applied Physics, 2006. **100**(6).

43. Tadokoro, S., et al. *Modeling of Nafion-Pt composite actuators (ICPF) by ionic motion.* in *Smart Structures and Materials 2000 Conference*. 2000. Newport Beach, Ca: Spie-Int Soc Optical Engineering.
44. Tamagawa, H., et al. *Bending curvature and generated force by Nafion actuator.* in *IEEE International Conference on Industrial Technology*. 2002. Bangkok, Thailand: Ieee.
45. Tamagawa, H., K. Yagasaki, and F. Nogata, *Mechanical characteristics of ionic polymer-metal composite in the process of self-bending.* Journal of Applied Physics, 2002. **92**(12): p. 7614-7618.
46. Tamagawa, H., et al., *Influence of metal plating treatment on the electric response of Nafion.* Journal of Materials Science, 2003. **38**(5): p. 1039-1044.
47. Yamaue, T., et al., *Electrostress Diffusion Coupling Model for Polyelectrolyte Gels.* Macromolecules, 2005. **38**(4): p. 1349-1356.
48. Porfiri, M., *Charge dynamics in ionic polymer metal composites.* Journal of Applied Physics, 2008. **104**(10): p. 104915-10.
49. Porfiri, M., *An electromechanical model for sensing and actuation of ionic polymer metal composites.* Smart Materials & Structures, 2009. **18**(1).
50. Rubinstein, I., J. Rishpon, and S. Gottesfeld, *An AC-Impedance Study of Electrochemical Processes at Nafion-Coated Electrodes.* Journal of the Electrochemical Society, 1986. **133**(4): p. 729-734.
51. Cahan, B.D. and J.S. Wainright, *AC Impedance Investigations of Proton Conduction in Nafion[trademark sign].* Journal of the Electrochemical Society, 1993. **140**(12): p. L185-L186.
52. Fontanella, J.J., et al., *ELECTRICAL-IMPEDANCE STUDIES OF ACID FORM NAFION(R) MEMBRANES.* Solid State Ionics, 1993. **66**(1-2): p. 1-4.
53. Cappadonia, M., J.W. Erning, and U. Stimming, *PROTON CONDUCTION OF NAFION((R))-117 MEMBRANE BETWEEN 140 K AND ROOM-TEMPERATURE.* Journal of Electroanalytical Chemistry, 1994. **376**(1-2): p. 189-193.
54. Gardner, C.L. and A.V. Anantaraman, *Measurement of membrane conductivities using an open-ended coaxial probe.* Journal of Electroanalytical Chemistry, 1995. **395**(1-2): p. 67-73.

55. Sone, Y., P. Ekdunge, and D. Simonsson, *Proton Conductivity of Nafion 117 as Measured by a Four-Electrode AC Impedance Method*. Journal of the Electrochemical Society, 1996. **143**(4): p. 1254-1259.
56. Paddison, S.J., D.W. Reagor, and T.A. Zawodzinski Jr, *High frequency dielectric studies of hydrated Nafion®*. Journal of Electroanalytical Chemistry, 1998. **459**(1): p. 91-97.
57. Paganin, V.A., et al., *Modelistic interpretation of the impedance response of a polymer electrolyte fuel cell*. Electrochimica Acta, 1998. **43**(24): p. 3761-3766.
58. Silva, R.F., A. De Francesco, and A. Pozio, *Tangential and normal conductivities of Nafion((R)) membranes used in polymer electrolyte fuel cells*. Journal of Power Sources, 2004. **134**(1): p. 18-26.
59. Casciola, M., et al., *On the decay of Nafion proton conductivity at high temperature and relative humidity*. Journal of Power Sources, 2006. **162**(1): p. 141-145.
60. Ma, S., Z. Siroma, and H. Tanaka, *Anisotropic Conductivity Over In-Plane and Thickness Directions in Nafion-117*. Journal of the Electrochemical Society, 2006. **153**(12): p. A2274-A2281.
61. Tsou, Y.M., M.C. Kimble, and R.E. White, *HYDROGEN DIFFUSION, SOLUBILITY, AND WATER-UPTAKE IN DOWS SHORT-SIDE-CHAIN PERFLUOROCARBON MEMBRANES*. Journal of the Electrochemical Society, 1992. **139**(7): p. 1913-1917.
62. Yeo, R.S. and J. McBreen, *Transport Properties of Nafion Membranes in Electrochemically Regenerative Hydrogen/Halogen Cells*. Journal of the Electrochemical Society, 1979. **126**(10): p. 1682-1687.
63. Unnikrishnan, E.K., *Permeation of inorganic anions through Nafion ionomer membrane*. Journal of Membrane Science, 1997. **137**(1-2): p. 133.
64. Nemat-Nasser, S., *Micromechanics: overall properties of heterogeneous materials*. 1993.
65. Mori, T. and K. Tanaka, *Average stress in matrix and average elastic energy of materials with misfitting inclusions*. Acta Metallurgica, 1973. **21**(5): p. 571-574.

66. Eshelby, J.D., *The determination of the elastic field of an ellipsoidal inclusion, and related problems*. Proceedings of the Royal Society of London. Series B, Biological sciences, 1957. **241**(1226): p. 376.
67. Taya, M., *Metal matrix composites: thermomechanical behavior*. 1989.
68. Brown, P.N., A.C. Hindmarsh, and L.R. Petzold, *Using Krylov Methods in the Solution of Large-Scale Differential-Algebraic Systems*. SIAM Journal on Scientific Computing, 1994. **15**(6): p. 1467-1488.
69. Hindmarsh, A.C., et al., *SUNDIALS: Suite of nonlinear and differential/algebraic equation solvers*. ACM Trans. Math. Softw., 2005. **31**(3): p. 363-396.